Faculdade de Engenharia da Universidade do Porto

Modelling the Gear Coefficient of Friction: Effects of Surface Finishing and Running-In

Miguel Ângelo de Sousa Dias



Master in Mechanical Engineering
Machine Design

Supervisor: Professor Carlos M. C. G. Fernandes

June, 2025

Modelling the Gear Coefficient of Friction: Effects of Surface Finishing and Running-In

Miguel Ângelo de Sousa Dias

Master in Mechanical Engineering
Machine Design

June, 2025

Abstract

The increasing concern of the climatic and financial cost of machine elements inspires the need to extend their lifespan. Therefore, it is essential to understand both wear and friction processes, motivating the development of efficient models for tribological contacts such as gears.

The proposed model applies the load-sharing concept that considers statistical surface roughness distribution. Initially, a Gaussian distribution is assumed, following the works of Faraon and Gelinck, and is then extended to other distributions, emphasizing that, after running-in, technical surfaces often deviate from a Gaussian profile.

The model was compared to traction and Stribeck curves obtained from a ball-on-disk test rig and results from an FZG gear test rig. With the validated model, a comparison of the coefficient of friction on gear surfaces before and after the running-in phase was conducted, and a wear model was developed to track surface evolution during running-in, where a new method to define a summit is proposed.

The results confirm the strong dependence of the coefficient of friction on surface roughness parameters and demonstrate the model's capability to predict and optimize the running-in process, resulting in reduced friction and possible extended gear lifespan.

Keywords: Friction, Gaussian Sufaces, Gears, Non-Gaussian Sufaces, Roughness, Running-in, Wear

Resumo

A crescente preocupação das implicações financeiras e climáticas dos componentes cria a necessidade de aumentar a sua vida útil. Por isso, é essencial entender o processo de desgaste e atrito, desenvolvendo modelos eficientes para o contacto entre engrenagens.

O modelo proposto aplica o conceito de partiha de carga, considerando a superficie como uma distribuição estatística. Inicialmente, foi assumida uma distribuição gaussiana, seguindo o trabalho de Faraon e de Gelinck e Schipper, sendo depois expandido para outras distribuições, realçando que, depois da rodagem, as superficies técnicas podem divergir de um perfil gaussiano.

O modelo proposto foi comparado com testes bola-disco e com resultados de engrenagens antes e depois da rodagem, onde foi proposto um novo metodo para selecionar as asperidades. Com o modelo validado, o coeficiente de atrito de engrenagens antes e depois da rodagem comparado.

Os resultados obtidos mostram a grande dependência entre o coefficiente de atrito e os parametros de rugosidade e demonstram a capacidade de prever e otimizar o processo de rodagem, resultando numa redução do atrito e aumentando a sua vida útil.

Keywords: Atrito, Desgaste, Engrenagens Rodagem, Rugosidade, Superficies Gaussianas, Superficies não Gaussianas,

Acknowledgements

First of all, I would like to thank my supervisor, Professor Carlos Fernandes by the guidance and opportunity of making part of this project, and all the members of CETRIB for the their help during this dissertation.

Next, I would to thanks to all the members of BSS Engineering's members in special to Cristiana Bonifácio and Jorge Henriques who believed in my potential.

To my friends Pedro, Maria, Beatriz, Francisco and Vasco that always stand by my side and always help me during this journey, to all of you I say thank you.

To my family I express my gratitude, in special to my parents and sister, for the countless times that stand by my side and without them this was not possible.

Lastly, to all the professors and colleagues that I encounter from my first school day to the my last master's class I thank you all for making me grow not only as a student but also as a person.

Miguel Dias

"Out there is the perfect lap. No mistakes.
Every gear change, every corner, perfect.
You see it?"

Ken Miles, Ford v Ferrari (2019)

Contents

1 Introduction **1**
- 1.1 Context . . . 1
- 1.2 Goal . . . 1
- 1.3 Methodology . . . 2
- 1.4 Structure . . . 2
- 1.5 Sustainable development goals . . . 2

2 Surface roughness **5**
- 2.1 Roughness parameters . . . 6
  - 2.1.1 Statistical parameters . . . 6
  - 2.1.2 Roughness measurement methods . . . 8
- 2.2 Surface filtering process . . . 12
  - 2.2.1 Conventional Method . . . 12
  - 2.2.2 Orthogonal distance fitting (ODF) . . . 14
  - 2.2.3 Numerical procedure . . . 16
- 2.3 Roughness parameters of the summits . . . 19
  - 2.3.1 Summit Parameters . . . 20
- 2.4 Surface Pattern . . . 22
- 2.5 Statistical distributions of the roughness profiles . . . 22
  - 2.5.1 Most likelihood method . . . 24
  - 2.5.2 Weibull distribution . . . 24
  - 2.5.3 Laplace distribution . . . 25
  - 2.5.4 Asymmetrical Laplace distribution (ALD) . . . 26
  - 2.5.5 Ex-Gaussian distribution . . . 27
  - 2.5.6 Skew-Normal distribution . . . 27
  - 2.5.7 Combination of two rough surfaces . . . 29

3 Running-in, Wear and Friction **31**
- 3.1 Running-in . . . 31
- 3.2 Wear mechanisms . . . 34
  - 3.2.1 Wear calculation . . . 37
  - 3.2.2 Gear wear . . . 39
- 3.3 Coeficient of friction . . . 40
  - 3.3.1 Load Sharing Concept . . . 41
  - 3.3.2 Empirical Methods . . . 42
  - 3.3.3 Coefficient of friction in gears . . . 44

4 Mixed lubrication model **49**
4.1 Hertzian contact . . . 49
4.2 Elastohydrodynamic Lubrication (EHL) . . . 50
4.2.1 Lubricant properties . . . 50
4.2.2 Line contact . . . 52
4.3 Boundary Lubrication . . . 55
4.4 Mixed Lubrication-Statistical model . . . 56
4.4.1 Greenwood and Williamson's asperity contact model . . . 57
4.4.2 Convergence Algorithm . . . 61
4.4.3 Model verification . . . 62
4.4.4 Faraon's asperity contact model . . . 65
4.4.5 Thermal model . . . 66
4.4.6 Application of the model to gears . . . 68

5 Comparison with experimental results **73**
5.1 Ball-on-disk - Gaussian Distribution . . . 73
5.1.1 Traction curves - Faraon's summits definition . . . 75
5.1.2 Stribeck curves - Faraon's summit definition . . . 80
5.1.3 Stribeck curves - Proposed summit definition . . . 80
5.1.4 Traction curves - Proposed summit definition . . . 86
5.2 Gears - Gaussian Distribution . . . 87
5.3 Ball-on-disk - Non Gaussian distributions . . . 93
5.4 Linear contact - Non Gaussian distributions . . . 96

6 Conclusions and Future works **101**
6.1 Conclusions . . . 101
6.2 Future works . . . 102

References **109**

A Elliptical Contact **111**
A.1 Hertzian Contact . . . 111
A.2 Elastohydrodynamic lubrication . . . 112
A.3 Mixed lubrication model . . . 113
A.4 Thermal model . . . 113

List of Figures

2.1 Average roughness. . . . 7
2.2 Peak-to-Valley parameters. . . . 7
2.3 Schematics of a stylus profilometer. . . . 8
2.4 Influence of the probe tip in the measurement. . . . 9
2.5 Schematics of an interferometer. . . . 9
2.6 Schematic of a confocal microscopy. . . . 10
2.7 Focal plane of a sample. . . . 10
2.8 Measurement of the roughness using the confocal chromatic technique. . . . 11
2.9 Topography measurement using light triangulation. . . . 11
2.10 Optical profiler. . . . 12
2.11 Tooth surface. . . . 13
2.12 Tooth roughness. . . . 13
2.13 Parametric generation of the involute profile. . . . 15
2.14 Root and tip circle. . . . 16
2.15 Scheme for the ODF algorithm. . . . 16
2.16 Fitted curves. . . . 17
2.17 Profile with the form removed. . . . 17
2.18 Roughness profile. . . . 18
2.19 Contact path coordinate. . . . 18
2.20 Example of a matrix for the summit selection. . . . 20
2.21 Diferent surface patterns. . . . 22
2.22 Height distribution of the surface fitted to a Gaussian distribution before and after running-in. . . . 23
2.23 Height distribution of the summits fitted to a Gaussian distribution before and after running-in. . . . 24
2.24 Height distribution of the summits fitted to a Weibull distribution. . . . 25
2.25 Height distribution of the summits fitted to a Laplace distribution. . . . 26
2.26 Height distribution of the summits fitted to an Asymmetrical Laplace distribution. . . . 26
2.27 Height distribution of the summits fitted to an Ex-Gaussian distribution. . . . 27
2.28 Height distribution of the summits fitted to a Skewed normal distribution. . . . 28
2.29 Height distribution of the summits fitted to several distributions. . . . 28
2.30 Example of the process to obtain the equivalent surface. . . . 29

3.1 Example of the influence of the running-in process in the roughness and friction. . . . 31
3.2 Evolution of the temperature during the runnng-in. . . . 32
3.3 Schematics of an asperity 33

3.4 Influence of the rolling speed in the running-in process. . . . 34
3.5 Influence of the contact load in the running-in process. . . . 34
3.6 Relative motion. . . . 35
3.7 Surface disturbance. . . . 35
3.8 Schematic of the wear of an asperity. . . . 39
3.9 Lubrication regimes. . . . 40
3.10 Stribeck curve. . . . 41
3.11 EHD2 Ultra Thin Film Measurement System. . . . 44
3.12 Contact between two gears. . . . 45
3.13 FZG gear test rig. . . . 45
3.14 Scheme of a two disk machine. . . . 45
3.15 Schmatic of the measuring system. . . . 46

4.1 Contact between two cylinders. . . . 50
4.2 Temperature effects on the lubricant properties. . . . 51
4.3 Moes' Diagram. . . . 54
4.4 Example of traction curves of lubricants. . . . 55
4.5 Example of the influence of SRR in the μ_c. . . . 56
4.6 Example of the contact of one smooth surface and a rough surface that follows a Gaussian distribution. . . . 58
4.7 Comparision between h_c and h'. . . . 59
4.8 Flowchart of the numerical method with pressure convergence. . . . 60
4.9 Flowchart of the numerical method with force convergence. . . . 61
4.10 Influence of the normal force. . . . 63
4.11 Influence of β and n (F_n= 2000 N and $\sigma_s = 0.05\,\mu m$). . . . 64
4.12 Influence of σ_s and n (F_n= 2000 N and $\beta = 10\,\mu m$). . . . 64
4.13 Influence of η_0 (F_n= 500 N). . . . 65
4.14 Influence of the sliding rate in the Sribeck's curve. . . . 65
4.15 Faraon's new model comparison. . . . 66
4.16 Flowchart of the thermal model iterative process. . . . 68
4.17 Start of gear tooth meshing. . . . 69
4.18 End of gear tooth meshing. . . . 69
4.19 Example of the normal force along the path of contact. . . . 70
4.20 Example of the speeds along the path of contact. . . . 71
4.21 Example of the contact radius along the path of contact. . . . 71

5.1 Selection criteria of the curves for the estimation of τ_L. . . . 76
5.2 Traction curves used for estimating τ_L. . . . 76
5.3 Comparison between the experimental and adjusted values of τ_L. . . . 77
5.4 Summit heights distribution. . . . 78
5.5 Traction curves used to estimate τ_L. . . . 78
5.6 Traction curves with disk 1. . . . 79
5.7 Stribeck Curves of disk 2 using Faraon's summit definition (F_n=50 N). . . . 80
5.8 Profile showing the summit selection with a (3x3) matrix along Hertz contact width ($2a$). . . . 81
5.9 Stribeck curves with different matrix sizes for T_0=40 °C and F_n=50 N. . . . 82
5.10 Profile showing the summit selection with matrix size of (5x5). . . . 82
5.11 Profile showing the summit selection with matrix size of (7x7). . . . 82
5.12 Profile showing the summit selection with matrix size of (9x9). . . . 83

5.13 Stribeck Curves of the disk 2. 83
5.14 Stribeck Curves of the disk 3. 84
5.15 Stribeck Curves of the disk 1. 84
5.16 Influence of the summits standard deviation on the Stribeck curves. 85
5.17 Influence of the summit density on the Stribeck curves. 85
5.18 Influence of the asperities radius on the Stribeck curves. 85
5.19 Stribeck Curves of the disk 2. 86
5.20 Stribeck Curves of the disk 3. 87
5.21 Traction curves at T_0=40 °C and F_n=50 N of each disk. 87
5.22 Experimental procedure to the gears' test. 88
5.23 Flowchart of the torque loss test 89
5.24 Coefficient of friction along the path of contact before and after the running-in process. 92
5.25 Influence of the wheel's speed on the mean coefficient of friction. 92
5.26 Influence of the wheel speed on the coefficient of friction along the path of contact. 93
5.27 Summit height distribution of ball and disk 2. 94
5.28 Example of the combined surface with a Ex-Gaussian distribution. 95
5.29 Stribeck curves of the medium roughness disk at T_0 =70 °C, F_n=50 N, and SRR=20%. 95
5.30 Summit heights of the G3's pinion before and after running-in 96
5.31 Summit heights of the pinions before and after running-in. 97
5.32 Gear set G1's coefficient of friction before and after running-in. 98
5.33 Gear set G2's coefficient of friction before and after running-in. 98
5.34 Gear set G3's coefficient of friction before and after running-in. 99

List of Tables

2.1 Shape deviation from DIN 4760. . . . 5
2.2 Cut-off length values from DIN 4768. . . . 6

3.1 Categorization of the normal wear types. . . . 36
3.2 Categorization of the generation of defects of the pathological wear types. . . 36
3.3 Categorization of the generation of heat of the pathological wear types. . . 36
3.4 Specific Film thickness. . . . 44

4.1 Kinematic viscosity of the ISO VG 150. . . . 51
4.2 Vogel's Law parameters. . . . 51
4.3 Reference values for the model verification. . . . 63
4.4 Roughness parameters for cases a and b. . . . 66
4.5 Steel properties. . . . 67

5.1 Relevant properties for the EHD2 test machine. . . . 73
5.2 Lubricant parameters 74
5.3 Properties of the traction curves 74
5.4 Roughness parameters of the disk used in the ball-on-disk tests 74
5.5 Properties of the Stribeck curves 75
5.6 Values for the estimation of τ_L. . . . 76
5.7 Adjusted parameters for PAO ISO VG 150. . . . 77
5.8 Comparison between the experimental and adjusted values of τ_L. . . . 77
5.9 Roughness parameters obtained with Faraon's summit selection method. . . 77
5.10 Roughness parameters to different matrix sizes. . . . 81
5.11 Roughness parameters using a (7x7) matrix. . . . 83
5.12 Parameters to select the matrix size. . . . 85
5.13 Roughness parameters for the disk 2's test. . . . 86
5.14 Roughness parameters for the disk 3's test. . . . 86
5.15 Properties of the gears. . . . 88
5.16 Running-in conditions. . . . 88
5.17 Values for the matrix size selection to each gear's sample 90
5.18 Difference between the roughness properties of the pinion and wheel before and after the running-in 90
5.19 Roughness parameters of the gears before and after running-in. . . . 91
5.20 Comparison between the coefficient of friction obtained in the model and experimentally. . . . 91
5.21 Distributions parameters for Ball and Disks. . . . 94
5.22 Distribution parameters of the pinion surface in the gear sets. . . . 97
5.23 Distribution parameters of the wheel surface in the gear sets. . . . 98

Abbreviations

ALD Asymetrical Laplace Distribution

EHL Elastohydrodynamic lubrication

FEM Finite elements model

MLE Most Likelihood Estimation

PDF Probability Density Function

Nomenclature

A	Real contact area	m^2
A_H	Hydrodynamic contact area	m^2
A_c	Nominal contact area	m^2
A_r	Wear model parameter	
$A_{surface}$	Area of the measured surface	m^2
B_i	Transient thermal resistance of body i	$K\,W^{-1}$
C_α	Dimensionless coefficient for a	
C_β	Dimensionless coefficient for a	
D	Deborah's number	
D_{ODF}	Sum of the square distance of all points in the ODF algorithm	m^2
E	Constant for the elliptical contact	
E	Elasticity modulus	Pa
E'	Reduced elasticity modulus	Pa
E_a	Heat absorption of the lubricant in the surface	$kJ\,mol^{-1}$
F_H	Load carried by the lubricant	N
F_c	Load carried by the asperities	N
F_n	Normal load	N
F_{bt}	Gear tangential force on the base plane	N
$F_{f,H}$	Friction force associated with Elastohydrdynamic regime	N
$F_{f,c}$	Friction force	N
$F_{f,c}$	Friction force associated with the asperities	N
G	Dimensionless lubricant number	
G	Shear modulus	Pa
H	Hardness	

H	Moes' dimensionless film thickness	
H_c	Moes' dimensionless central film thickness	
H_{00}	Dimnesionaless parameter related with the ellipticity of the contact	
H_{VL}	Gear loss factor	
K	Achard's wear coefficient	
K	Parameter of Vogel's Law	
K_I	Wear coefficient in mixed lubrication regime	
K_m	Dimensionless constant for wear, independent of the lubricant	
L	Thermal loading parameter	$\mathrm{m\ s^2 kg^{-1} K^{-1}}$
L	Likelihood function	
L	Moes' dimensionless lubricant number	
L	Sliding distance	m
M	Moes' dimensionless load number	
M_i	Steady-state thermal resistance of body i	$\mathrm{K\,W^{-1}}$
N	Number of summits in contact	
N_m	Number of sites on the friction surface unoccupied by molecules	
N_r	Total number of sites on the friction surface	
N_s	Number of summits in the surface	
P_V^i	Total power loss	W
P_{VD}	Seals power losses	W
P_{VL}	Rolling bearings power losses	W
P_{VZ0}	Load-independent power loss	W
P_{VZP}	Load-dependent power loss	W
P_{in}	Inlet power	W
R_a	Average roughness	m
R_g	Gas constant	$\mathrm{Jmol^{-1} K^{-1}}$
R_q	Root-mean-square profile height	m
R_x	Reduced radius	m
R_x	Reduced radius in x direction	m
R_y	Reduced radius in y direction	m

R_{ai}	Initiall average roughness	m
R_{cf}	Thermal resistant of the oil	$\mathrm{K\,W^{-1}}$
R_{fi}	Thermal resistant of the body i	$\mathrm{K\,W^{-1}}$
R_{max}	Maximum peak-to-valley height	m
$R_{z_{DIN}}$	Mean peak-to-valley height	m
SRR	Slide to roll ratio	
S_0	Roelands' exponent to temperature	
S_g	Gear geometric parameter	
S_p	Hersey parameter	
S_{ep}	Value of SRR where the transition from the elastic to plastic behaviour occurs	
T_s	Absolute temperature of the surface	K
U	Rolling speed	m/s
U_i	Speed of body i	m/s
U_Σ	Dimensionless speed number	
V	Wear volume	$\mathrm{m^3}$
V_e	Entrainment speed	m/s
V_s	Sliding rate	
W	Dimensionless load number	
X	Interpolation parameter	
X_L	Lubricant parameter	
Z	Roelands' exponent to pressure	
$\Delta\overline{T_{oil}}$	Average oil temperature rise	K
$\Delta\overline{T}_{Fl}$	Average flash temperature rise	K
Δ_x	Measurement step in the x direction	m
Δ_x	Step in the x direction	
Δ_y	Measurement step in the y direction	m
Δ_y	Step in the y direction	
Γ	Surface pattern parameter	
Λ	Specific film thickness	
Ψ	Ratio between the metal-on-metal contact area to the real area	

α	Lubricant wear dependent coefficient	
α	Piezoviscosity	Pa^{-1}
α_n	Normal pressure angle	$^\circ$
α_{SN}	Shape parameter of the Skew-Normal distribution	
α_{γ_1}	Step length in the optimization algorithm of γ_1	
α_{wt}	Working pressure angle	$^\circ$
α_{yt}	Incidence angle of point Y	$^\circ$
β	Helix angle	$^\circ$
β	Mean radius of the asperities	m
β	Thermoviscosity	K^{-1}
β_j	Equivalent radius of the asperity j	m
β_i	Asperity radius of the surface i	m
β_{xj}	Radius of an asperity j in the x direction	m
β_{yj}	Radius of an asperity j in the y direction	m
χ_i	Thermal diffusivity	m^2/s
δ	Diference in the otimization problem	
δ_{SN}	Scale parameter of the Skew-Normal distribution	
$\dot{Q}$	Heat	W
$\dot{\gamma_e}$	Elastic shear rate	Pa/s
$\dot{\gamma_v}$	Viscous shear rate	Pa/s
$\dot{\gamma}$	Shear rate	Pa/s
$\dot{q}$	Heat flux	$\mathrm{W/m}^2$
ϵ	Heat partition	
ϵ_α	Contact ratio	
η	Dynamic viscosity	Pa s
η_0	Inlet dynamic viscosity	Pa s
γ_1	Lubricant load carrying factor	
γ_2	Asperities load carrying factor	
κ	Constant for the elliptical contact	
κ_{AL}	Skewness parameter of the Asymmetrical Laplace distribution	

λ	Ratio between the radius	
λ_c	Cut off lenght	m
λ_{SN}	Location parameter of the Skew-Normal distribution	
λ_w	Scale parameter of the Weibull distribution	
μ	Coefficient of friction	
μ_E	Location parameter of the Ex-Gaussian distribution	
μ_c	Coefficient of friction of the asperities	
μ_{BL}	Coefficient of friction in the boundary lubrication regime	
μ_{EHL}	Coefficient of friction in the Elastohydrodynamic lubrication regime	
$\mu_{c,max}$	Maximum value of μ_c	
μ_{mZ}	Mean coefficient of friction	
μ_{max}	Maximum coefficient of friction	
ν	Kinematic viscosity	m^2/s
ν	Poisson's ratio	
ω	Angular speed	rad/s
Γ	Gamma distribution	
Φ	Cumulative distribution function of the Gaussian distribution	
ϕ	Probability density function of the Gaussian distribution	
$\overline{T}_f$	Average oil temperature	K
$\overline{\sigma_s}$	Normalized standard deviation of the summit heights	
$\overline{\zeta_1}$	Mean height of the summits	m
$\overline{h}$	Dimensionless film thickness	
$\overline{n}$	Normalized asperity density	
$\overline{p_c}$	Mean contact pressure in the asperities	Pa
ϕ	Angle of the rotation of the ODF algorithm	$^\circ$
ϕ_T	Correction factor for the temperature	
ρ	Density of the lubricant	kg/m^3
ρ_i	Density of the body i	kg/m^3
ρ_y	Radius of curvature	m
ρ_{yi}	Radius of the contact in the point Y	m

σ_E	Shape parameter of the Gaussian function in the Ex-Gaussian distribution	
σ_s	Standard deviation of the summit heights	m
σ_{AL}	Scale parameter of the Asymmetrical Laplace distribution	
σ_{si}	Standard deviation of the summits of the surface i	m
τ_0	Eyring shear stress	Pa
τ_E	Shape parameter of the Exponential function in the Ex-Gaussian distribution	
τ_H	Hydrodynamic shear stress	Pa
τ_L	Limit shear stress	Pa
θ	Temperature	°C
θ_L	Location parameter for the Laplace distribution	
θ_{AL}	Location parameter for the Asymmetrical Laplace distribution	
ϑ	Ratio between the radius in the rolling direction an perpendicular to the rolling direction	
ξ	Contact path coordinate	
ξ_y	Rolling angle of the involute as point Y	°
a	Centar distance	m
a	contact half-width	m
a_χ	Diameter of the area associated with an absorbed molecule	m
a_w	Working center distance	m
b	Facewidht	m
b	Parameter of Vogel's Law	$°C^{-1}$
c	Parameter of Vogel's Law	$°C^{-1}$
c_p	Specific heat capacity of the lubricant	$J\,kg^{-1}\,K^{-1}$
c_{p_i}	Specific heat capacity of the body i	$J\,kg^{-1}\,K^{-1}$
d	Reference diameter	m
d_a	Tip diameter	m
d_b	Base diameter	m
d_d	Difference between the mean surface height and mean asperity height	m
d_f	Root diameter	m
$f(s)$	Probability distribution function	

h	Film thickness	m
h'	Mean separation between the two rough surfaces	m
h_0	Central film thickness	m
h_c	Central film thickness	m
h_m	Minimal film thickness	m
k	Step number	
k	Thermal conductivity of the lubricant	$\mathrm{W\,m^{-1}\,K^{-1}}$
k_r	Wear model parameter	
$k_{s,i}$	Thermal conductivity of the body i	$\mathrm{W\,m^{-1}\,K^{-1}}$
k_w	Shape parameter of the Weibull distribution	
l_n	Length of the surface	m
m	Constant for the elliptical contact	
m_0	Zeroth moment of power density	$\mathrm{m^2}$
m_2	Second moment of power density	
m_4	Fourth moment of power density	$\mathrm{m^{-2}}$
m_n	Nominal modulus	m
m_{ie}	Equivalent moment of the power density of order i	
m_{imax}	Maximum moment of the power density of order i	
m_{imin}	Minimum moment of the power density of order i	
n	Density of asperities	$1/\mathrm{m^2}$
n_i	Asperity density of the surface i	m
p_H	Hydrodynamic contact pressure	Pa
p_h	Hertizian pressure	Pa
p_m	Mean hertzian pressure	Pa
p_{bt}	Transverse base pitch	m
r	Reference radius	m
r_a	Tip radius	m
r_b	Base radius	m
s	Gold's equation parameter	
s_L	Shape parameter of the Laplace distribution	

t	Gold's equation parameter	
t_0	Fundamental time of vibration of the molecule in the absorbed state	s
t_f	Root radius	m
t_r	Running-in duration	min
u	Gear ratio	
v_g	Sliding speed	m/s
$v_{\Sigma C}$	Sum of speeds at the pitch point	$\mathrm{m\,s^{-1}}$
v_{bt}	Gear tangential speed on the base plane	N
w	Displacement	m
x	Profile shift	
x_0	Coordinate x of the translation vector for the ODF algorithm	m
x_i	Coordinate x of the measured profile of a gear	m
x_k	Coordinate x of the theoretical profile of a gear	m
x_w	Shift parameter of the Weibull distribution	
x_y	Coordenate in the x axis of a point Y in the involute profile	m
y_0	Coordinate y of the translation vector for the ODF algorithm	m
y_i	Coordinate y of the measured profile of a gear	m
y_k	Coordinate y of the theoretical profile of a gear	m
y_y	Coordenate in the y axis of a point Y in the involute profile	m
z	Number of teeth	
z	Surface height	m
M_m	Translation matrix for the ODF algorithm	
M_r	Rotation matrix for the ODF algorithm	
d	Distance vector in ODF algorithm	m
r_i	Position vector of the measured profile	m
r_k	Position vector of the theoretical profile	m
$inv\ \alpha_{yt}$	Involute of angle α_{yt}	°

Exponents

$'$	Approximated value
exp	Values acquired experimentally

GW Values related with the Greenwood and Williamson's asperity contact model

Subscripts

$_1$ Properties of the pinion or surface 1

$_2$ Properties of the wheel or surface 2

i Measured profile for the ODF algorithm

j Properties of the summit j

k Theoretical profile for the ODF algorithm

Chapter 1

Introduction

1.1 Context

In recent years, besides the financial cost, the climatic cost of a component has gained great relevance, so it is essential to increase its life span. To achieve that, it is crucial not only to understand both wear and friction processes but also to be able to model them [1, 2]. With this in mind, this dissertation will implement a friction model.

Once the friction model is fully implemented, it will be possible to study how to decrease it, which leads to an increase in efficiency of the system and a decrease in wear.

In literature, friction in the boundary and elastohydrodynamic regimes have equations or reference values to predict them but there are some problems in how to estimate the friction in the mixed lubrication regime, where some work must be done, and, besides that, the gears normally work in this regime, so it is important to develop a computationally efficient model applicable to them.

1.2 Goal

The goal of this dissertation is to model the coefficient of friction in gears and study the influence of the surface finishing and the alterations in the surface caused by running-in process. To accomplish that, several objectives must be defined:

1. Develop a statistical model to calculate the coefficient of friction in a lubricated linear contact between rough surfaces;
2. Implement the model for gears;
3. Couple a thermal model and update 1. and 2.;
4. Validate the model with experimental results;
5. Since the model used statistical distributions of the roughness, study the influence of the selected distribution.

1.3 Methodology

The implementation of the refereed model was carried out in Python, where a statistical approach was used, that while is not the most accurate method, it is much more computational efficient than other alternatives like finite elements models (FEM) or to use a deterministic approach. The model's core is based on Johnson's load sharing concept [3] and Greenwood and Williamson's asperity contact model [4].

The process to obtain the roughness parameters is described, and the results from the model are compared with experimental results from ball-on-disk tests and gear tests before and after running-in.

During repetitive tasks in coding process it was used ChatGPT to help to structure the Python code.

1.4 Structure

In addition to the introduction, this dissertation will be organized in five more chapters, each with an important role in reaching the objectives of this dissertation.

Chapter 2 is dedicated to the surface roughness, a central point of this dissertation. It is explained two different procedures to obtain the surface roughness, how the summits can be selected, and calculate the roughness parameters required by the model.

Chapter 3 develops a literature review of relevant concepts about running-in, wear, and friction necessary to understand the other chapters.

Chapter 4 explains Greenwood and Williamson's asperity contact model implemented in this dissertation and verifies it with values from the literature. The model is further expanded to be applied to gears and to incorporate a thermal model.

Chapter 5 compares the numerical results of the model to experimental results from ball-on-disk and gears, highlighting the influence of the roughness parameters in the results. It also discusses some limitations of the model.

Chapter 6 takes some conclusions about the dissertation, and the next steps are discussed.

1.5 Sustainable development goals

As the global awareness for the climatic changes increases, it is important to contextualize this dissertation in the 2030 Agenda for Sustainable Development. From the 17 sustainable development goals, this dissertation can be framed in the following ones [5]:

- **Goal 9 – Industry, Innovation and Infrastructure** — Especially target **9.5**, as both the understanding and modeling of friction in gears contribute to enhancing scientific research and can support the upgrading of technological capabilities in the industrial sector.

- **Goal 12 – Responsible Consumption and Production** - In line with target **12.2**, once the modeling process of fiction will enable strategies to reduce it, leading to a lower wear, and extended component's life-span;
- **Goal 13 – Climate Action** — Aligned with target **13.2**, the study of friction will develop techniques to reduce it, increasing the mechanical efficiency of mechanical systems, that when integrated in the industry could lower the greenhouse gas emission.

Chapter 2

Surface roughness

A well-known fact in engineering is that creating a perfectly smooth surface, as depicted in manufacturing drawings, is impossible. Therefore, it is essential to acknowledge that all mechanical components exhibit shape deviation. This is significantly influenced by the manufacturing processes used to produce the component. Shape deviations are classified in the DIN 4760 (Table 2.1). The last two orders are generally neglected, so the profiles measured result from the superposition of the other four orders [6].

Table 2.1: Shape deviation from DIN 4760 - Adapted from [7].

Shape deviation	**Examples**	**Causes**
1st order: form deviation	Straightness, flatness, roundness, etc.	Error in the guideways of the equipment, incorrect clamping, hardening, or wear
2nd order: Waviness	Waves (DIN 4761)	Off-center clamping, form, or concentric deviation of a milling cutter, or vibrations
3rd order: Roughness	Grooves (DIN 4761)	Cutting edge shape, feed or depth of cut of the tool
4th order: Roughness	Grooves, scales, and lumps (DIN 4761)	Process chip formation, or material deformation during treatments
5th order: Roughness	Texture	Processes of crystillization, surface alteration by chemical reaction. or corrosion processes
6th order	Structure of the material	

Before calculating the roughness parameters, the profile must be levelled, removing the form deviation and the inclination of the profile if the measurement's reference plane is not parallel to the surface and must be filtered to remove the waviness from the profile [6].

To filter the profile, a cut-off length, denoted as λ_C, must be selected. It is recommended that (λ_C) be at least 2.5 times the peak-to-peak spacing of the profile roughness. If the peak-to-peak spacing is not easily identifiable, the values of DIN 4768 can be utilized (Table 2.2) [6].

Table 2.2: Cut-off length values from DIN 4768 - Adapted from [6].

λ_c / mm	Peak spacing / mm	Measured Roughness (R_a) / µm	(R_z) / µm
0.08	<0.032	-	-
0.25	0.032 - 0.1	<0.1	<0.5
0.8	0.1 - 0.32	0.1 - 2	0.5 - 10
2.5	0.32 - 1	2 - 10	10 - 30
8	>1	>10	>30

The removal of the form and waviness from the profile results in the roughness profile, which is the only one used for the calculation of the roughness parameters because the form deviation, and the larger wavelength of the waviness do not contribute to the micro-scale interactions in the contact.

2.1 Roughness parameters

With the filtered profile, the roughness parameters can be calculated. There are several relevant parameters, both with advantages and disadvantages. As will be discussed in more detail in Section 3.1, the running-in causes a smoothening of the surface, hence, one parameter must be chosen to analyze the impact of the running-in. Normally, this parameter is the average roughness (R_a).

2.1.1 Statistical parameters

The arithmetic roughness is mostly used to monitor production processes where changes in the surface finishing are expected, for example, in the grinding of gears and running-in. It describes the average deviation from the centerline of the surface (Figure 2.1) [7]. R_a is not greatly influenced by local defects on the surface so they have a greater measuring repeatability. Unlike other parameters, it does not differentiate between peaks and valleys [6].

$$R_a = \frac{1}{l_n} \int_0^{l_n} |z(x)| dx \tag{2.1}$$

Where $z(x)$ is the height of the profile at the position x and l_n is the length of the profile.

Root-mean-square profile height (equation (2.2)) is similar to R_a, being more sensitive to peaks and valleys and more relevant to statistical methods. It is not widely used due



Figure 2.1: Average roughness - Adapted from [6].

to the use of parameters that measure extreme values, but it is commonly employed in contacts mechanics and lubrication, and represents the standard deviation of the surface.

$$R_q = \sqrt{\frac{1}{l_n}\int_0^{l_n} z^2(x)dx} \tag{2.2}$$

The maximum peak-to-valley height measures the maximum difference in height between a peak and a valley (Figure 2.2). The profile is divided into five parts, each with the same length as the cut-off length, from where the maximum peak-to-valley (z_i) are averaged to calculate $R_{z_{DIN}}$ (equation (2.3)). Those parameters are relevant because they analyze the bigger defects of the surface, which is extremely important when defects are not allowed. Seals, are an example of that, where a simple scratch can affect the performance [6].

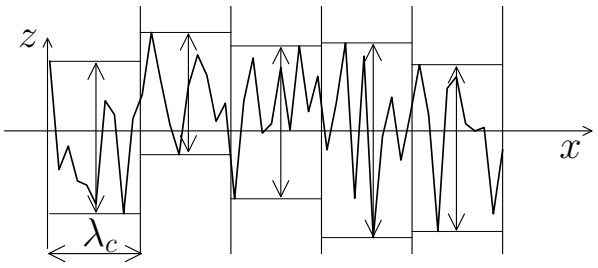


Figure 2.2: Peak-to-Valley parameters - Adapted from [6].

$$R_{z_{DIN}} = \frac{1}{5}\sum_{i=1}^{5} z_i \tag{2.3}$$

R_{max} and $R_{z_{DIN}}$ are used together to monitor the quality of the finishing process, if they are similar, a consistent surface finishing is achieve, while if they are very different, it indicates the presence defects in the surface [6]. Other parameters are relevant in more

specific scenarios, namely R_p and R_{pm}, maximum and mean peak height, respectively, and R_v and R_{vm}, maximum and mean valley height [6].

2.1.2 Roughness measurement methods

2.1.2.1 Stylus profilometry

The stylus profilometry, illustrated in Figure 2.3, uses a stylus to measure the surface. It normally consists of a probe, a tracing element, and a drive unit. The drive unit imposes a displacement in the probe, allowing measurements of all surfaces either in 2D or 3D [8].

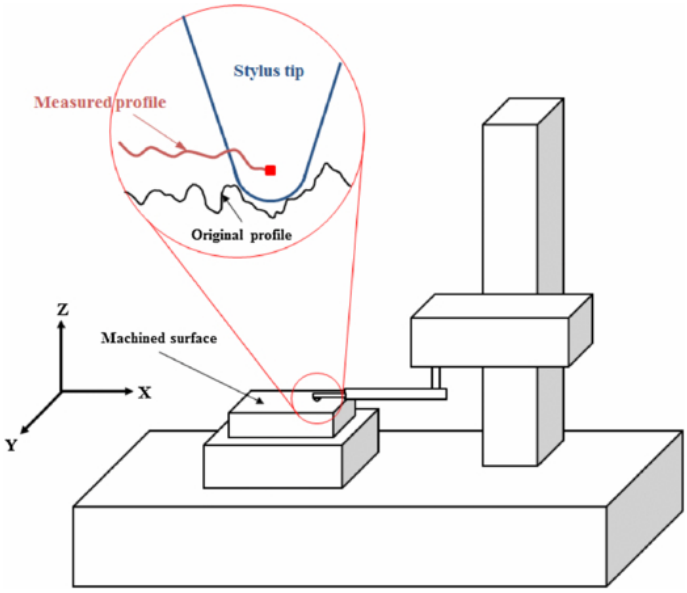
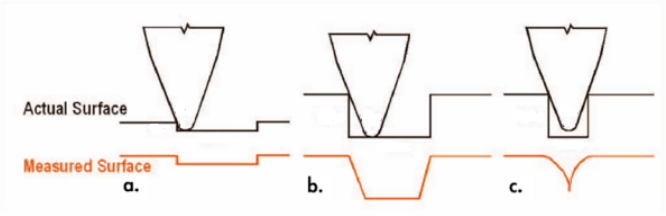
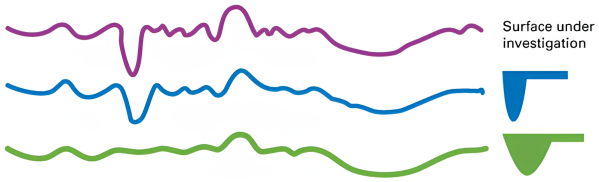


Figure 2.3: Schematics of a stylus profilometer [9].

In this technique, the shape and tip radius of the probe are important characteristics. A smaller probe is capable of better describe the surface which increases the precision of the obtained profile. The Figure 2.4a shows how the same tip measures different surfaces, where it is shown that the accuracy of a measurement is highly related with the surface itself, and the Figure 2.4b shows the measurement of a profile using different tips, where it is clear that a bigger tip reduces the accuracy of the measurement. The contact between the probe and the surface, applies a force in the probe, causing elastic deformation in softer materials and the wear of the tip influences the results. Because it is a contact technique, it is slower than non-contact techniques [8].



(a) Influence of the surface in the measurement.



(b) Influence of the tip size.

Figure 2.4: Influence of the probe tip in the measurement [10].

2.1.2.2 White light interferometry

White light interferometry uses a light source that, by a series of reflections and refractions, can get a black-and-white image that follows the topography of the surface [8], as shown in Figure 2.5. This technique has the advantage of measuring a large area, allowing to measure the surface of a sample in only one measurement [10].

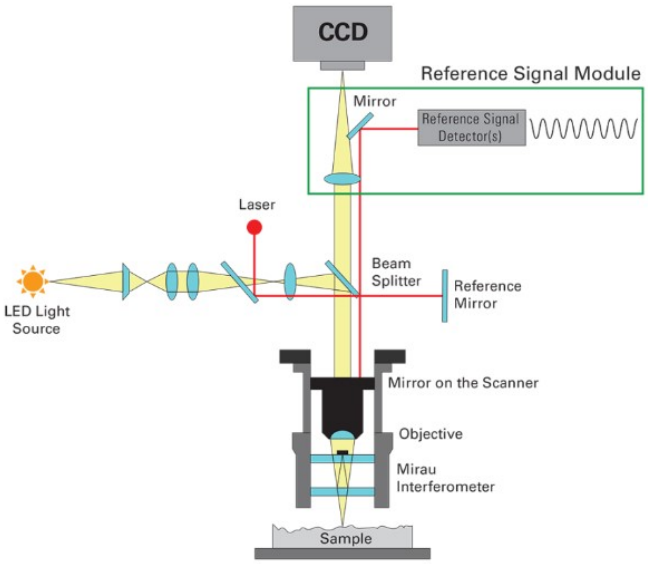


Figure 2.5: Schematics of an interferometer [10].

2.1.2.3 Confocal microscopy

Confocal microscopy was developed to decrease image blurring, sharpening the images even on thick plates. The surface is mapped by a light that passes through a pin hole and

is reflected to the sensor (Figure 2.6). The resulting image only gets the information of the focal plane, as shown in Figure 2.7, so it is required a vertical scan of the sample to get all the surface levels [8]. This technique has an important role in non-flat or translucent specimens [11].

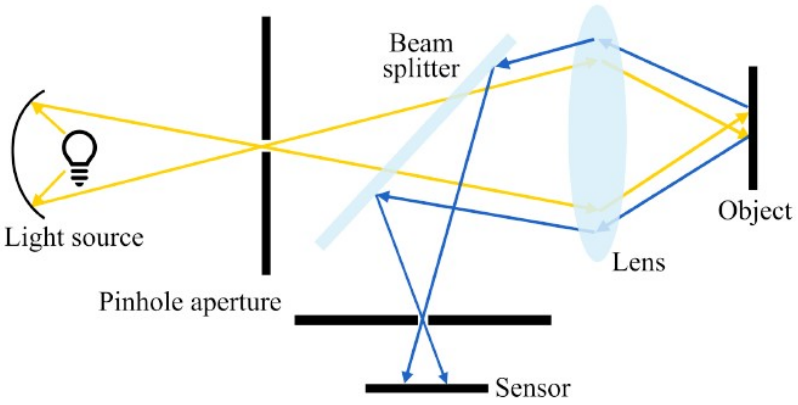


Figure 2.6: Schematic of a confocal microscopy [8].

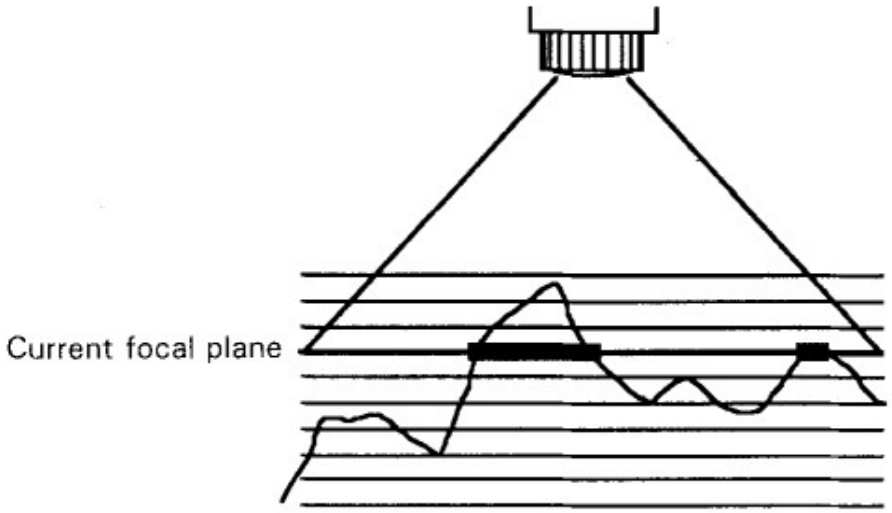


Figure 2.7: Focal plane of a sample [11].

2.1.2.4 Confocal Chromatic

Confocal Chromatic is a measurement method where a chromatic objective inside the probe decomposes the light into several wavelengths. The surface reflects the beam of light with a wavelength related to the distance of the surface to the probe, that is, the height of the profile is a function of the returned wavelength, represented in Figure 2.8. This procedure only measures the height of the focal point meaning that, to map all the

surface, it is necessary to move the probe along the object's surface [8]. This method is influenced by the roughness of the surface, due to the scattering of the light in the surface [12].

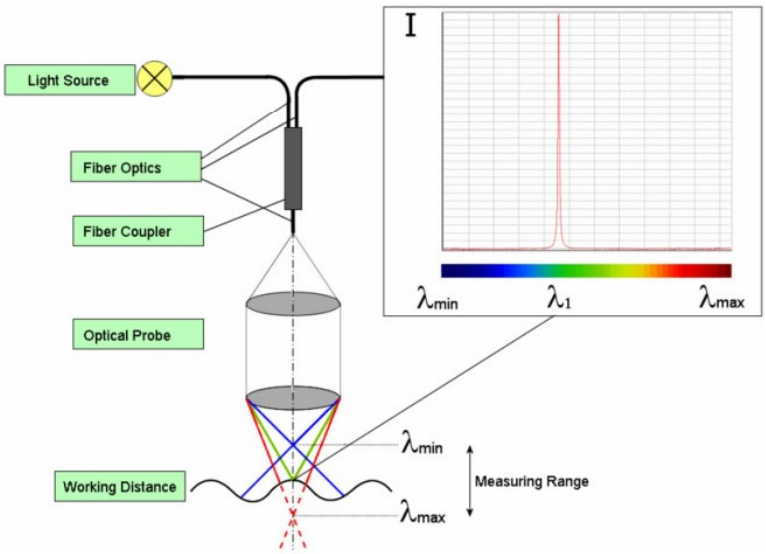


Figure 2.8: Measurement of the roughness using the confocal chromatic technique [13].

2.1.2.5 Structured Light Projection

Structured Light Projection measures the topography of the surface by triangulating the light beams of a light reflected by the surface, exemplified in Figure 2.9. With the lateral displacement of the light beams, it is calculated the height of the surface [8].

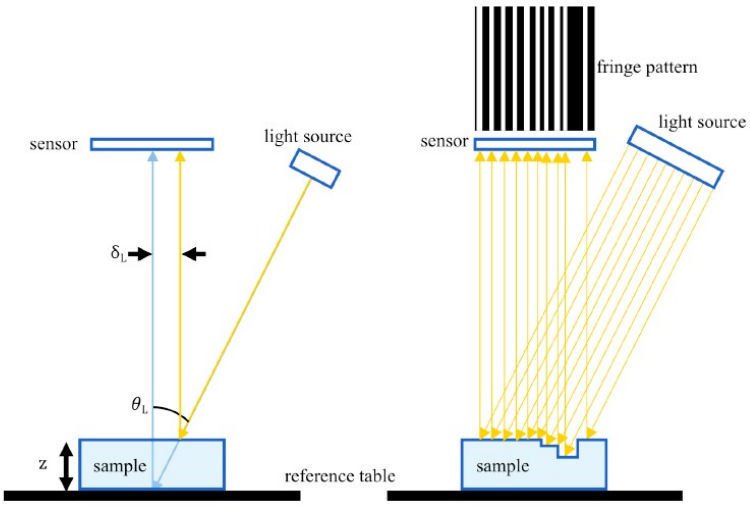


Figure 2.9: Topography measurement using light triangulation [8].

2.2 Surface filtering process

From the profiles or surfaces obtained with the equipment described in previous section, it is extremely important to be able to calculate the roughness parameters. A common procedure, on all the surfaces and stylus profiles, is to level and filter those profiles/surfaces. Later in this dissertation, two approaches to remove the curvature and waviness of the samples will be discussed. In the first approach, the Vision64 software is used to remove the curvature and tilt of the sample and filter the waviness by applying a Gaussian filter with a normalized cut-off length (λ_c), which will be discussed in Chapter 5.

Li et al. [14] proposed a new approach, only applicable for gear profiles, where the tooth's form is removed by fitting the theoretical tooth's profile to the measured one. Within this approach, the waviness is also removed with a Gaussian filter. Brandão et al. [15] also proposed a technique to remove the tooth's form, but due to the simplicity of Li et al.'s approach it will be used in this dissertation.

With this in mind, this section will be structured as follows: first, the two methods to obtain the roughness will be discussed, then how to obtain the roughness parameters needed for the model, and lastly, some statistical distributions are presented to model the summit heights. It is important to note that this chapter will be more focused on describing the process from a theoretical point of view, while the results obtained will be presented in Chapter 5.

2.2.1 Conventional Method

To measure the necessary parameters to characterise the surface, it was used the optical profiler from Bruker (Figure 2.10) that uses white light interferometry to measure the surface.



Figure 2.10: Optical profiler.

The measured surface (Figure 2.11) has its form removed in the Vision64 software with a 4th-order degree polynomial in the case of gears and disks, and a spherical fit in the case of the ball used during the ball-on-disk test. After that, a Gaussian filter is applied,

filtering the waviness and leaving only the roughness (Figure 2.12) that is exported, and the roughness parameters are calculated following the procedure in Section 2.3. Another method to filter the waviness out is to use a process called functional filtering, where it is assumed that anything with a wavelength higher than the length of the contact zone should be filtered out, resulting in λ_c similar to the Hertz contact width, where is typical to select the standard value (DIN 4768) closer to that value [16].

In the surfaces obtained using the conventional method, the roughness properties of the measured zone are assumed to be the same along the whole surface. This assumption is arises from the difficulty measuring the whole surface or accurately tracking the exact contact zone to consider the roughness properties near the contact zone.

Another problem with this approach is that only the tip of the tooth could be measured, as the preceding tooth obstructs access to the remaining surface. Therefore, the surface roughness of the tooth's tip are assumed to be the same as the whole tooth.

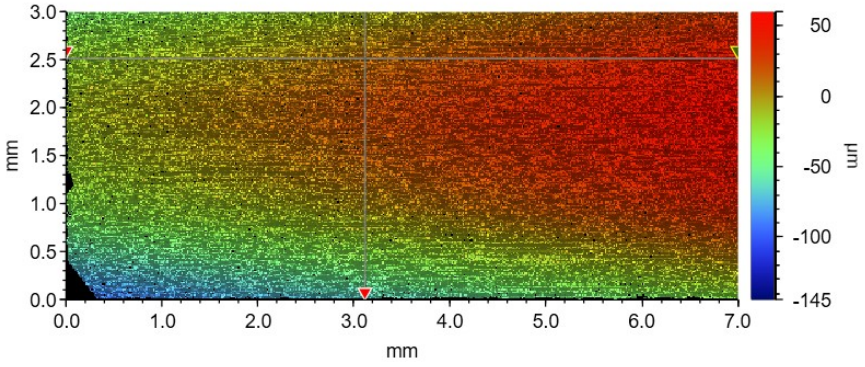


Figure 2.11: Tooth surface.

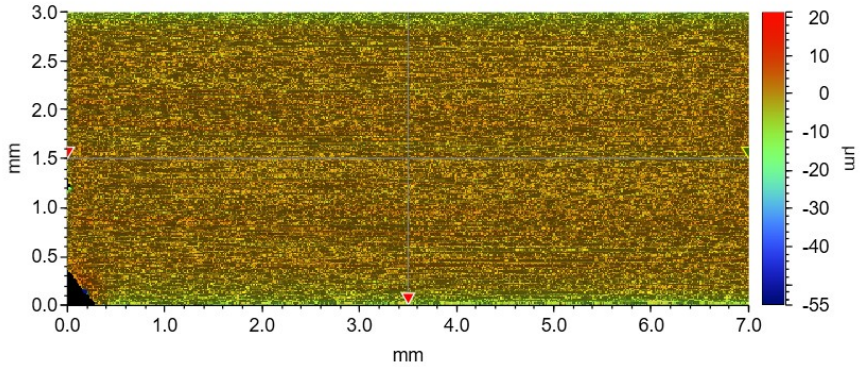


Figure 2.12: Tooth roughness.

With this in mind, it is interesting to develop a procedure that allows the model to consider the roughness parameters of the contact zone instead of the properties of the

whole surface. This can be done for tooth profiles following the procedure described in the next subsection.

2.2.2 Orthogonal distance fitting (ODF)

A new approach for accounting for the roughness is only to consider the roughness in the neighborhood of the contact zone, also known as local roughness, which has the advantage of not being affected by defects away from the contact area. This approach of considering the local roughness will allow a more accurate implementation of the statistical model because each point along the path of contact of gears will have a summit height distribution based on its neighborhood.

Li et al. [14] proposed an implementation of this concept using a 2D measurement (profile) in which they measure the entire tooth, presenting a technique to extract the involute part and remove the form deviation with the use of an ODF (Orthogonal distance fitting) algorithm by fitting a theoretical tooth profile to the measured profile. However, the extraction of the involute part of the profile in this dissertation is done manually. Since the theoretical tooth's profile is need to remove the form, it is important to first understand the involute gear geometry and how to create that theoretical profile.

2.2.2.1 Involute gear geometry

The gear geometry discussed and implemented follows the International Standard referent to cylindrical involute gears, BS ISO 21771:2007. Under that standard, the nominal dimensions of a gear are defined [17]:

- Number of teeth (z);
- Standard basic rack tooth profile;
- Nominal modulus (m_n) (normalized values in ISO 54) ;
- Helix angle (β) and flank direction (0° in the case of spur gears);
- Profile shift coefficient (x);
- Tip diameter (d_a);
- Face width (b).

In a involute gear it is important to define the reference circle, with radius (r) expressed in equation (2.4) and the base circle, with radius called base radius (r_b), is the circle from where the involute surface is generated and is calculated with equation (2.5).

$$r = \frac{d}{2} = \frac{|z|m_n}{2} \tag{2.4}$$

$$r_b = \frac{d_b}{2} = \frac{|z| m_n \cos \alpha_n}{2} \tag{2.5}$$

Where α_n is the normal pressure angle, that is normally $\alpha_n = 20^\circ$.

The involute profile is defined by the point Y with coordinates following the system of equations (2.6), as seen in Figure 2.13. In equations (2.7) and (2.8), α_{yt} is the incidence angle of the point Y [18].

$$\begin{cases} x_y = r_b \cdot (\cos \xi_y + \xi_y \cdot \sin \xi_y) \\ y_y = r_b \cdot (\sin \xi_y - \xi_y \cdot \cos \xi_y) \end{cases} \tag{2.6}$$

Where:

$$\xi_y = \tan(\alpha_{yt}) \tag{2.7}$$

$$\text{inv } \alpha_{yt} = \tan(\alpha_{yt}) - \alpha_{yt} \tag{2.8}$$

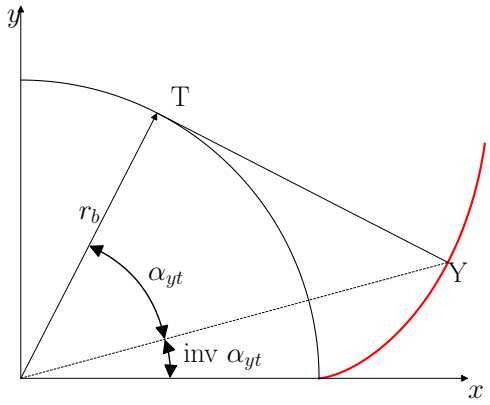


Figure 2.13: Parametric generation of the involute profile - Adapted from [18].

A tooth is limited by the root and tip circle (Figure 2.14), defined by the root radius (r_f) and tip radius (r_a), respectively. Following a type A profile, r_f and r_a is defined by equations 2.9 and 2.10, respectively, where x is the profile shift.

$$r_f = r - (1.25 \cdot m_n - x m_n) \tag{2.9}$$

$$r_a = r + (m_n + x m_n) \tag{2.10}$$

In equation (2.11), the equation for calculating the working center distance (a_w) is given. If the working center distance is made equal to the cutting center distance, the working pressure angle (α_{wt}) is equal to α_n and the center distance is given by equation (2.12).

$$a_w = \frac{1}{2}\left(d_{w2} + \frac{z_2}{|z_2|} d_{w_1}\right) = \left(\frac{r_{b_2}}{\cos \alpha_{wt}} + \frac{z_2}{|z_2|} \frac{r_{b_1}}{\cos \alpha_{wt}}\right) \tag{2.11}$$

$$a_w = \left(r_1 + \frac{z_2}{|z_2|} r_2 \right) \tag{2.12}$$

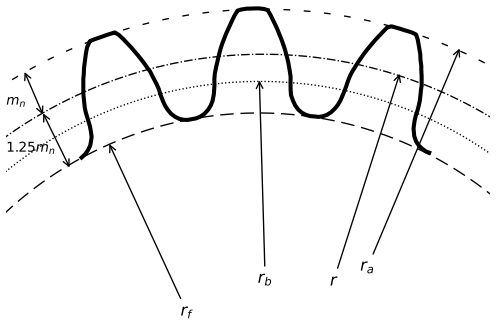


Figure 2.14: Root and tip circle - Adapted from [18].

2.2.3 Numerical procedure

With the involute profile extracted, the ODF is achieved by moving the measured profile and rotating the theoretical curve as shown in Figure 2.15, meaning that a corresponding point in both curves has the distance given by [14]:

$$\mathbf{d} = \mathbf{M}_m \mathbf{r}_i - \mathbf{M}_r \mathbf{r}_k = \begin{bmatrix} 1 & 0 & x_0 \\ 0 & 1 & y_0 \\ 0 & 0 & 1 \end{bmatrix} \begin{bmatrix} x_i \\ y_i \\ 1 \end{bmatrix} - \begin{bmatrix} \cos\phi & -\sin\phi & 0 \\ \sin\phi & \cos\phi & 0 \\ 0 & 0 & 1 \end{bmatrix} \begin{bmatrix} x_k \\ y_k \\ 1 \end{bmatrix} \tag{2.13}$$

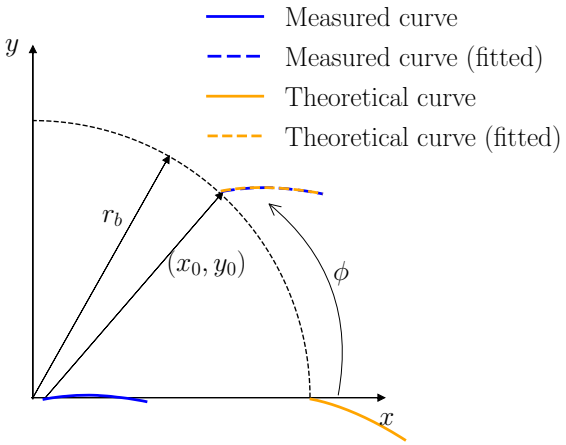


Figure 2.15: Scheme for the ODF algorithm.

Where $\mathbf{r}_i$ is the position vector of the measured curve, with coordinates (x_i, y_i), $\mathbf{r}_k$ is the position vector of the theoretical curve, with coordinates (x_k, y_k), $\mathbf{M}_m$ is the translation matrix with the translation coordinates (x_0, y_0), $\mathbf{M}_r$ is the rotation matrix that promotes a rotation of the theoretical curve around the origin with an angle ϕ and $\mathbf{d}$ is the difference between the measured and theoretical curves after the translation and rotation process, respectively. D_{ODF} results from the application of the least squares method (equation (2.15)), so minimizing it, the optimal values of x_0, y_0, and ϕ are obtained. To enhance the optimization performance, the theoretical profile is generated with the system of equations (2.14) because its form is more similar to the measured curve. Figure 2.16 shows the adjustment of both curves, from where the form is removed (Figure 2.17) and the profile filtered following the ISO 4288 and $\lambda_c = 0.8\,\text{mm}$ (Figure 2.18) or it can be filtered out using the functional filtering method. In all of those figures, the x-axis is the contact path coordinate (ξ) that is the distance from the pitch point along the path of contact (Figure 2.19), normalized with the base pitch ($p_b = \pi m_n \cos\alpha_n$), where ξ=0 correspond to the pitch point.

$$\begin{cases} x_k = r_b \cdot (\cos\xi_y + \xi_y \cdot \sin\xi_y) \\ y_k = -r_b \cdot (\sin\xi_y - \xi_y \cdot \cos\xi_y) \end{cases} \tag{2.14}$$

$$D_{ODF} = \sum_{i=0}^{n} \|\mathbf{d}\|^2 \tag{2.15}$$

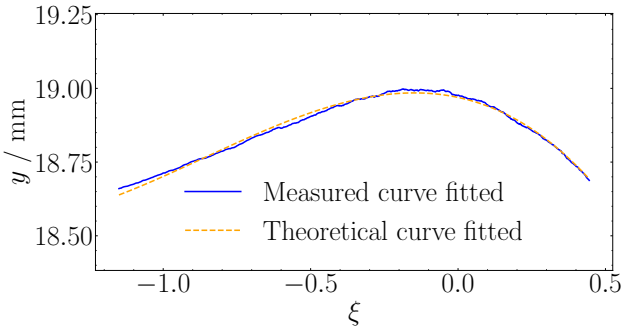


Figure 2.16: Fitted curves.

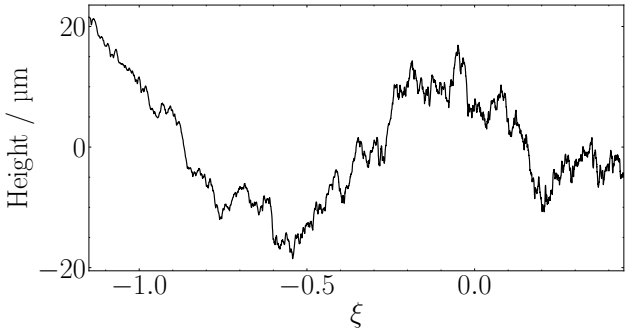


Figure 2.17: Profile with the form removed.

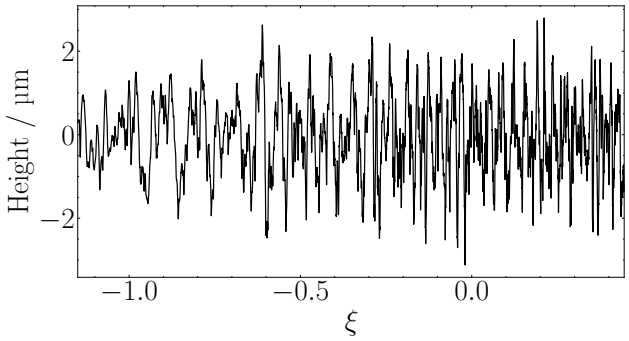


Figure 2.18: Roughness profile.

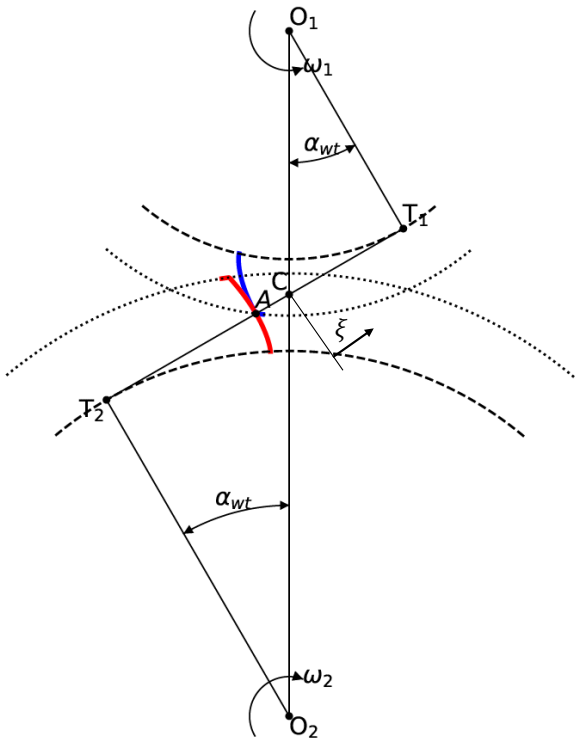


Figure 2.19: Contact path coordinate - Adapted from [18].

The Figure 2.15 represents both curves before the fitting process and since the theoretical curve can only rotate around the origin and the measured curve is close to the origin it is expected that the curves after the fitting process start around the base circle, meaning the norm of the translation vector (x_0, y_0) must be similar to r_b, so the following restriction in the optimization problem was imposed:

$$0.9 \cdot r_b \leq \sqrt{x_0^2 + y_0^2} \leq 1.1 \cdot r_b \tag{2.16}$$

It was also imposed that all those optimization variables (x_0, y_0, and ϕ) are greater than 0 and ϕ must be lower than $\pi/2$, which ensures that the fitting process always occurs

in the first quadrant.

The results of this method are highly related to the capacity of ensuring that a point in the measured curve is fitted to the correct point in the theoretical curve. To solve this problem, in each iteration, the theoretical curve with coordinates $(x'_k,\ y'_k)$ is generated with an estimation of the value of ξ_y, manipulating the equation (2.13):

$$\begin{cases} x_i + x_0 = x'_k \cos\phi - y'_k \sin\phi \\ y_i + y_0 = x'_k \sin\phi + y'_k \cos\phi \end{cases} \tag{2.17}$$

Solving the linear system of equations (2.17) and using the Newton-Raphson method for obtaining ξ_y from the value of x'_k. With ξ_y, the theoretical curve is created, and the distance to the measured one is calculated.

2.3 Roughness parameters of the summits

Regardless of the procedure used to obtain the roughness, it is important to understand how a summit is defined. With the summits defined, the process to calculate the relevant properties is explained. During the contact between the two surfaces, only the summits of each surface will contact each other, so those summits must be identified. With a discrete measurement, in the Faraon's work [19], a summit is defined as a point higher than all its surrounding 8 points, that is, a point is a summit if that point is the biggest point in a 3x3 matrix centred at that point. This definition, which will be called Faraon's definition, is more influenced by noise problems, can select summits in valley zones that aren't expected to contact the other surface, and can select the same asperity more than once.

With the results used in the Chapter 5, the use of this definition will result in a model that over-selects the summits and does not adjust to the experimental values, so another criterion to define a summit is selected. The matrix from which the central point has to be the highest for it to be considered a summit was increased, making the selection window bigger than twice the asperity radius in each direction, ensuring that one summit is only selected one time.

Therefore, the new method proposed consists in selecting an adequate matrix size that makes the matrix window bigger than the asperity diameter in each direction. This approach has the disadvantage of defining a summit using a rectangular matrix in which the central point is at different distances from the matrix's limits, resulting in a different minimal distance between summits for each direction. To exemplify this the Figure 2.20 shows the process to select the point 5 as a summit with a (3x3) matrix. The distance between points 5 and 6 is the step distance in the x direction (Δx), and the distance between points 5 and 8 is the step distance in the y direction (Δy). Even if Δx and Δy are equal, the distance between the point 5 and 9 is $\sqrt{\Delta x^2 + \Delta y^2}$ that is higher than Δx and Δy. This results in a minimal distance between summits of $2\Delta x$ in the x direction,

$2\Delta y$ in the y direction, and $2\sqrt{\Delta x^2 + \Delta y^2}$ in the diagonal. Even with this problem, it has the advantage of being a quick selection method.

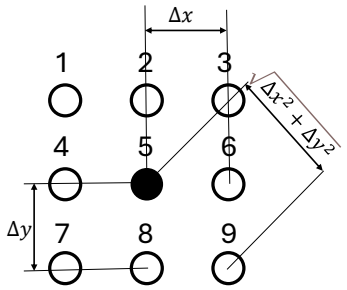


Figure 2.20: Example of a matrix for the summit selection.

To overcome that limitation, a distance-based search process could be implemented, where only the points below a minimal distance are compared with the central point, to identify that point as a summit. While this approach almost ensures a constant minimal distance between summits, it is more computationally demanding and, if not correctly implemented, with run times similar to the deterministic models.

A different approach to select summits in profiles, consists in selecting a summit if it first passes through a lower threshold and then through an upper threshold [20]. Although this definition is interesting, it is more computationally demanding and can create some problems when expanded to a 3D surface.

2.3.1 Summit Parameters

The roughness parameters needed for the statistical model to model the surface in the Chapter 3 are the standard deviation of the summit heights (σ_s), summit density (n), and asperity radius (β), and to calculate them, there are two different approaches. The first approach, used in this dissertation, involves identifying the summits on the surface and calculating those properties using the number and height of those summits. The other one uses the zeroth, second, and fourth moments of the power density, m_0, m_2, and m_4, respectively, to estimate the roughness parameters.

For the first method, the summits are selected by the procedure previously described, and the standard deviation of the height of those summits is calculated. To account for the roughness of both surfaces, σ_s results from the combination of σ_s of each surface (equation (2.18)). Dividing the number of summits (N_s) by the area of the measured surface ($A_{surface}$), the asperity density of each surface is calculated (equation (2.19)) and averaged to get the asperity density of the combined surface [19].

$$\sigma_s = \sqrt{\sigma_{s1}^2 + \sigma_{s2}^2} \tag{2.18}$$

$$n_i = \frac{N_{s,i}}{A_{surface,i}} \tag{2.19}$$

$$n = \frac{n_1 + n_2}{2} \tag{2.20}$$

The radius of the summit j is calculated in both directions (β_{xj} and β_{yj}) with the equation (2.21) and (2.22), respectively, where Δx and Δy are the measurement step in the x and y directions. The equivalent radius of each summit (β_j) is calculated (equation (2.23)), and the equivalent radius of each summit is then averaged to obtain the average asperity radius of each surface (β_i). With equation (2.25), the radius of the asperities of the combined surface is calculated. If a roughness profile is utilized, parameters labeled with subscript (y) are disregarded [19]. While in this dissertation only a statistical model is implemented, it is possible to implement a deterministic model where the unique radius of each asperity is used, which allows to capture the individual characteristics of every asperity in a more meaningful way. Yet, this deterministic approach results in a more computationally demanding process.

$$\beta_{xj}^{-1} = \frac{z(x-\Delta x, y) - 2z(x,y) + z(x+\Delta x, y)}{\Delta x^2} \tag{2.21}$$

$$\beta_{yj}^{-1} = \frac{z(x, y-\Delta y) - 2z(x,y) + z(x, y+\Delta y)}{\Delta y^2} \tag{2.22}$$

$$\beta_j = \sqrt{\beta_{xj} \cdot \beta_{yj}} \tag{2.23}$$

$$\beta_i = \frac{1}{N_s} \sum_{j=1}^{N_s} \beta_j \tag{2.24}$$

$$\frac{1}{\beta} = \frac{1}{\beta_1} + \frac{1}{\beta_2} \tag{2.25}$$

As an alternative, for statistical methods, it is possible to use statistical parameters to estimate the necessary values. Using the zeroth, second, and fourth moments of the power density, m_0, m_2, and m_4, respectively, n and β can be estimated in equations (2.30) and (2.29), respectively [21].

$$m_0 = E[z^2] \tag{2.26}$$

$$m_2 = E\left[\left(\frac{dz}{dx}\right)^2\right] \tag{2.27}$$

$$m_4 = E\left[\left(\frac{d^2z}{dx^2}\right)^2\right] \tag{2.28}$$

Where E[ ] denotes the statistical expectation.

$$n = \frac{m_4 m_2}{6\pi\sqrt{3}} \tag{2.29}$$

$$\overline{\beta} = \frac{3}{8}\sqrt{\frac{\pi}{m_4}} \tag{2.30}$$

$$\overline{\zeta_1} = \frac{4\sqrt{m_0}}{\sqrt{\pi\alpha}} \tag{2.31}$$

$$\sigma_s = \sqrt{\left(1 - \frac{0.8968}{\alpha}\right) m_0} \tag{2.32}$$

Where $\overline{\zeta_1}$ is the mean height of the summits [22], σ_s is the standard deviation of summit heights and α is given by:

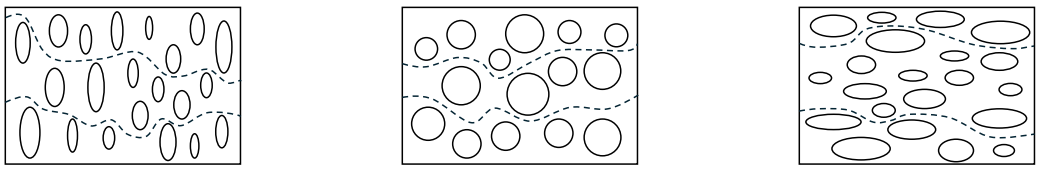
$$\alpha = \frac{m_0 m_4}{m_2^2} \tag{2.33}$$

If the moments of the power density are different in the other directions, it is calculated an equivalent moment (m_{ie}) with the equation (2.34), where m_{imax} and m_{imin} are the maximum and minimum moment of order i. If both surfaces are considered rough, the moments of each surface are summed together [23].

$$m_{ie} = \sqrt{m_{imax} m_{imin}} \tag{2.34}$$

2.4 Surface Pattern

The surface pattern (Figure 2.21) reflects the orientation of the asperities on a surface, and it is characterized by the surface pattern parameter (Γ). If the parameter equals 1, the pattern is isotropic. If it is less than 1, the surface shows a transverse roughness orientation, that is commonly seen in gears. If it is greater than 1, the surface shows a longitudinal orientation.



(a) Transverse ($\Gamma < 1$). (b) Isotropic ($\Gamma = 1$). (c) Longitudinal ($\Gamma > 1$).

Figure 2.21: Diferent surface patterns - Adapted from [23].

2.5 Statistical distributions of the roughness profiles

Before discussing the statistical distributions of the summit heights, it is important

to discuss the first the surface as a whole. Figure 2.22 shows a comparison between the distribution of the surface heights before and after running-in, where it is clear that the running-in process mostly wears away the higher points of the surface. Besides that, it is shown how a Gaussian distribution models a surface, and after the running-in process, it is clear that the accuracy of the Gaussian distribution is reduced.

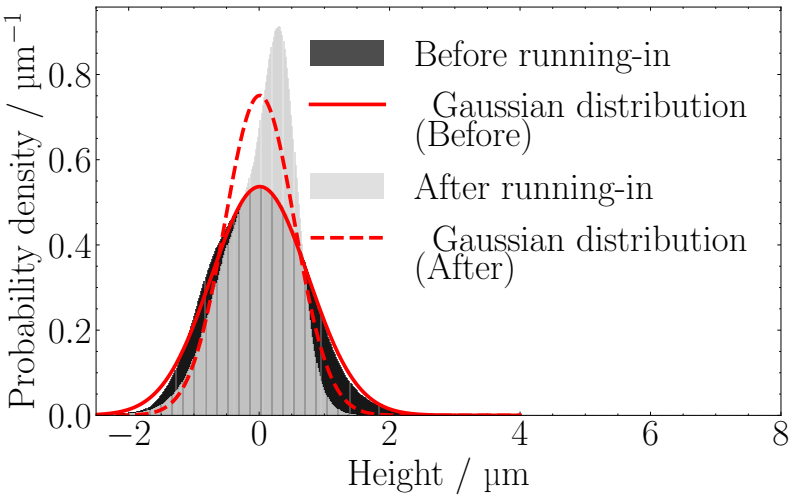


Figure 2.22: Height distribution of the surface fitted to a Gaussian distribution before and after running-in.

In the literature, it is typically selected the Gaussian distribution to model the summit heights, but that selection is not the most accurate when considering samples after the running process. Figure 2.23 shows the evolution of the summits before and after running-in and it is clear that a new surface, obtained by processes like grinding and polishing, can be approximated by a Gaussian distribution. In opposition, after running-in, the Gaussian distribution does not model the summit heights with the same precision because, during the running-in, the higher summits suffer wear that leads to an asymmetrical height distribution. As shown in Figure 2.23, higher summits are present before the running-in process, and after running-in, the higher summits are lower, and there is a bigger concentration around the mean height of the summits.

Since the Gaussian distribution is the most used, it will be more detailed in Chapter 4 where the model is discussed.

In the remainder of this section, several distributions are individually explained, how the relevant parameters are estimated, and then compared with surfaces that have already completed the running-in process. While in some distributions it is possible to make a good approximation of the necessary parameters using the statistical properties, in others, that approximation is not recommended or it is difficult, so those parameters can be calculated using the most likelihood estimation (MLE), so before the explanation of each distribution, the most likelihood method will be explained.

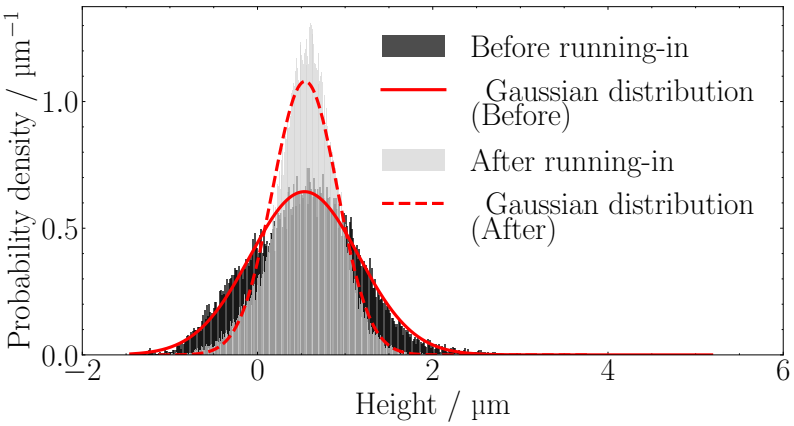


Figure 2.23: Height distribution of the summits fitted to a Gaussian distribution before and after running-in.

2.5.1 Most likelihood method

The most likelihood method, in a simple definition, estimates the characteristic parameters of a distribution that better adjust to the available data [24]. Assuming $f(z)$ as a generic distribution, the Likelihood function $L(X)$ is given by:

$$L(X) = \prod_{i=1}^{n} f(z_i) \tag{2.35}$$

Where X is the vector with the distribution's parameters and z_i is the height of a summit. Taking the log operator on both sides of the equation (2.35) it is obtained the equation (2.36). Now, maximizing the logarithm of the likelihood, vector X is obtained, and the distribution is defined.

$$\log\left(L(X)\right) = \log\left(\prod_{i=1}^{n} f(z_i)\right) \tag{2.36}$$

2.5.2 Weibull distribution

Figure 2.24 shows the Weibull distribution adjusted to a post running-in surface, where a better fit is achieved at the extremes, while no great improvements are seen to the remaining heights. From the work of Abubakar et al. [25], the probability density function is:

$$f\left(x; k_w, \lambda_w, x_w\right) = \begin{cases} \dfrac{k_w}{\lambda_w}\left(\dfrac{x - x_w}{\lambda_w}\right)^{k_w - 1} \exp\left[-\left(\dfrac{x - x_w}{\lambda_w}\right)^{k}\right], & x \geq x_w \\ 0, \quad x < x_w \end{cases} \tag{2.37}$$

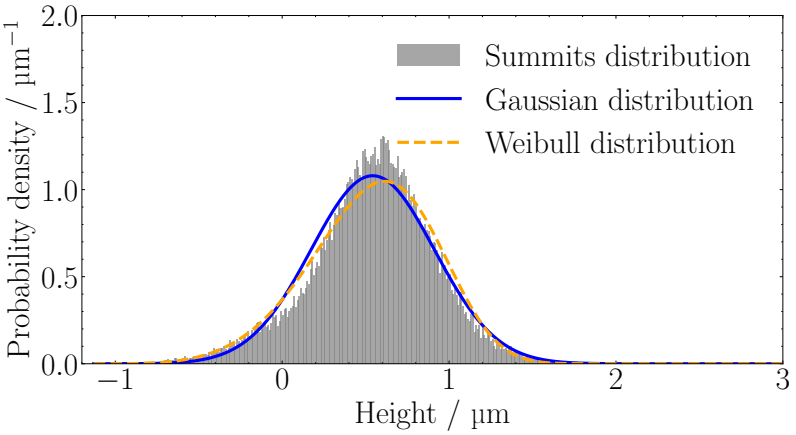


Figure 2.24: Height distribution of the summits fitted to a Weibull distribution.

Where k_w is the shape parameter and λ_w is the scale parameter, and x_w is the shift parameter, which represents the starting point of the function. While those parameters can be estimated with the equations (2.38) and (2.39) [25], it is not accurate, so the MLE is used.

$$\mu = \lambda_w \Gamma\left(1 + \frac{1}{k_w}\right) + x_w \tag{2.38}$$

$$\sigma^2 = \lambda_w^2 \left[\Gamma_{\mathrm{w}}\left(1 + \frac{2}{k_w}\right) - {\Gamma_{\mathrm{w}}}^2\left(1 + \frac{1}{k_w}\right)\right] \tag{2.39}$$

An important aspect of this distribution is that, since $f(x) = 0$ if $x < x_w$, it is ensured that the probability of a summit have an height bellow x_w is 0 and all the summits are above x_w, as opposed to the other distributions, where there is no lower bound.

2.5.3 Laplace distribution

Following the same approach, Figure 2.25 shows the fit of the Laplace distribution with the summit heights and the probability density function is defined in equation (2.40) [26], where is seen a great increase of the accuracy at the lower summits at the cost of a bad fit around the central values.

$$f\left(x; s_L, \theta_L\right) = \frac{1}{2s_L} \exp\left(-\frac{1}{s_L}\left|x - \theta_L\right|\right) \tag{2.40}$$

Where θ_L is the median value and s_L is the shape parameter, which can be calculated by equation (2.41), or using the most likelihood method. Yet, the same result is achieved independent of the selected method.

$$s_L = \frac{1}{N_s} \sum_{i=1}^{N_s} \left|x_i - \theta_L\right| \tag{2.41}$$

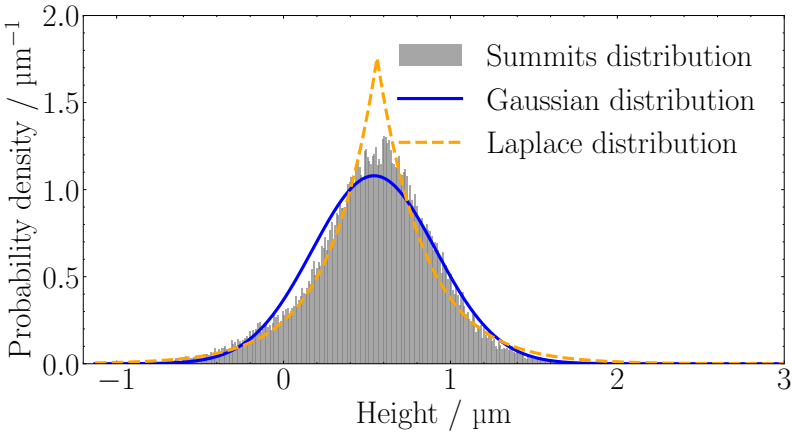


Figure 2.25: Height distribution of the summits fitted to a Laplace distribution.

2.5.4 Asymmetrical Laplace distribution (ALD)

The Asymmetrical Laplace distribution is similar to the classic Laplace distribution, but it allows different decays below and above the value of θ_{AL} and the probability density function follows equation (2.42) where θ_{AL} is the median value of x, σ_{AL} is the scale parameter and κ_{AL} is the skewness parameter obtained with the most likelihood method [26]. Figure 2.26 shows the fit of the ALD to the summits distribution and its comparison to the Laplace distribution, where no relevant changes are noticed, keeping the same vantages and disadvantages as the Laplace distribution.

$$f\left(x;\kappa_{AL},\sigma_{AL},\theta_{AL}\right)=\frac{1}{\sigma_{AL}}\cdot\frac{\kappa_{AL}}{\left(1+\kappa_{AL}^{2}\right)}\begin{cases}\exp\left[-\dfrac{\kappa_{AL}}{\sigma_{AL}}\left(x-\theta_{AL}\right)\right], & x\geq\theta_{AL}\\[2ex] \exp\left[\dfrac{1}{\sigma_{AL}\kappa_{AL}}\left(x-\theta_{AL}\right)\right], & x<\theta_{AL}\end{cases} \tag{2.42}$$

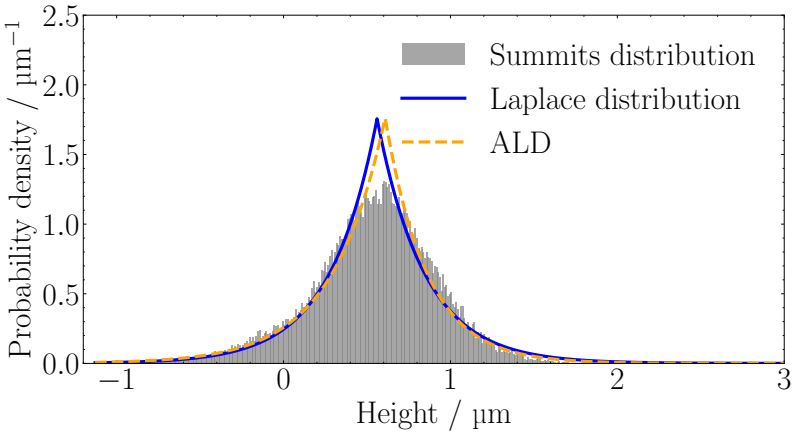


Figure 2.26: Height distribution of the summits fitted to an Asymmetrical Laplace distribution.

2.5.5 Ex-Gaussian distribution

As was already shown, the accuracy of the Gaussian distribution to model the summits after running-in is reduced when compared with summits before running-in, so it could be interesting to study a distribution that allows the higher summits to present an exponential behavior. That distribution is called Ex-Gaussian distribution (equation (2.43)) and mixes both distributions [27], where σ_E is the shape parameter of the Gaussian component, τ_E is the shape parameter of the Exponential component and μ_E is the location parameter.

The distribution parameters are calculated with the most likelihood method, and Figure 2.27 shows the fit of the Ex-Gaussian distribution to the summit heights, and there are no differences when compared to the Gaussian distribution. This happens because the analyzed sample does not present an exponential behavior, and as a consequence, the exponential component (τ_E) is negligible when compared to the Gaussian component (σ_E). Nonetheless, the importance of this distribution will be better discussed in Chapter 5 when other samples are presented.

$$f\left(x;\tau_E,\sigma_E,\mu_E\right)=\frac{1}{\tau_E\sqrt{2\pi}}\exp\left(\frac{\sigma_E^2}{2\tau_E^2}-\frac{x-\mu_E}{\tau_E}\right)\int_{-\infty}^{\frac{x-\mu_E}{\sigma_E}-\frac{\sigma_E}{\tau_E}}\exp\left(-\frac{y^2}{2}\right)dy \tag{2.43}$$

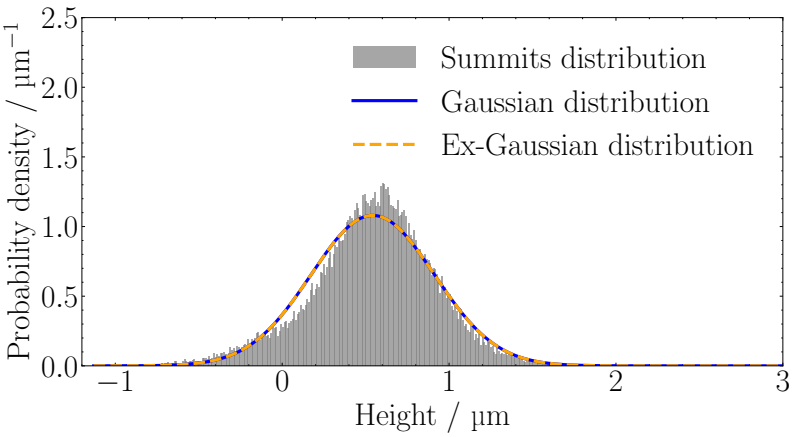


Figure 2.27: Height distribution of the summits fitted to an Ex-Gaussian distribution.

2.5.6 Skew-Normal distribution

The Skew-Normal distribution is very similar to a Gaussian distribution (Figure 2.28), but it allows the function to be asymmetrical, which ensures a better fit. If the heights do not show that asymmetrical behavior (called skewness), the distribution transforms into a classic Gaussian distribution, so the Skew-Normal distribution can be defined as an extension of the normal distribution. This is achieved by introducing a new parameter

α_{SN} in the probability density function (equation (2.44)) [28].

$$f(x;\lambda_{SN},\delta_{SN},\alpha_{SN}) = \frac{2}{\delta_{SN}}\,\phi\left(\frac{x-\lambda_{SN}}{\delta_{SN}}\right)\Phi\left(\alpha_{SN}\frac{x-\lambda_{SN}}{\delta_{SN}}\right) \tag{2.44}$$

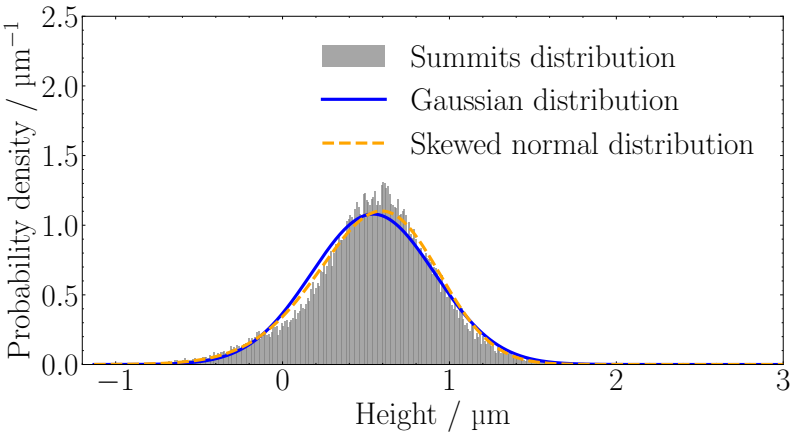


Figure 2.28: Height distribution of the summits fitted to a Skewed normal distribution.

Where δ_{SN} is the scale parameter, α_{SN} is the shape parameter, λ_{SN} is the location parameter. ϕ and Φ are, respectively, the probability density function and cumulative distribution function of the standard normal distribution.

With all the distributions explained, Figure 2.29 shows the comparison between all distributions described here. Generally, all the distributions have better behavior in different zones. Both Laplace distributions fit better to extreme values, but they are the worst around mean height values. The Weibull and Skew normal distributions improve the

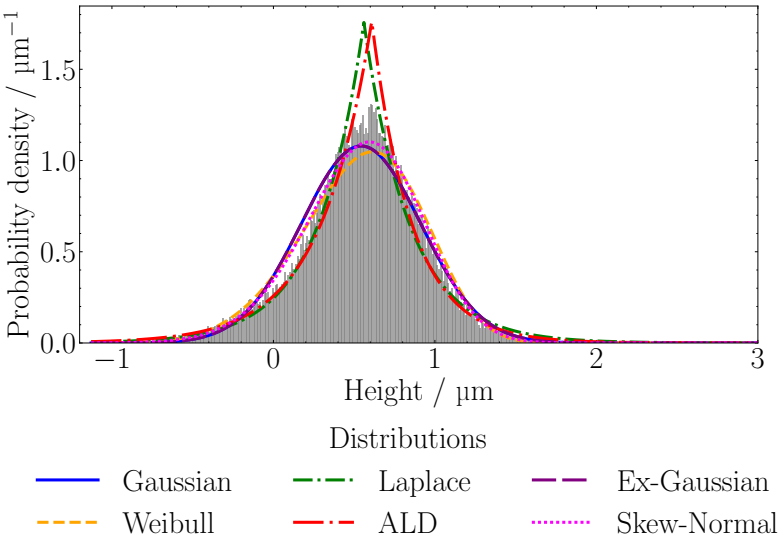


Figure 2.29: Height distribution of the summits fitted to several distributions.

model process of the summits, which means that they are the most relevant to model post-running-in surfaces. With this sample, no conclusion can be made for the Ex-Gaussian distribution, but, as will be discussed, it will have a greater relevance in modeling the samples before running-in.

2.5.7 Combination of two rough surfaces

The Greenwood and Williamson's asperities contact model was developed considering that one surface is rough while the other is flat. To overcome this problem, it was considered a contact between one flat and one rough surface that combines the roughness of both surfaces.

When a Gaussian distribution is assumed, this process is simplified because the equivalent surface also follows a Gaussian distribution, and that could be the main reason why this distribution is widely used even in surfaces that have already suffered running-in.

However, when other distributions are considered, that equivalent surface does not follow the same distribution as the individual components. In other words, if both follow a Weibull distribution, the resultant surface will not follow a Weibull distribution. Therefore, it is necessary to find a way to combine both distributions. The combination of two or more probability distributions is done using an operator called convolution:

$$f(s) = [h_1 * h_2](s) = \int_{-\infty}^{\infty} h_1(x)h_2(s-x)dx \tag{2.45}$$

Where h_1 and h_2 are the probability distribution functions of each surface, and $f(s)$ is the distribution of the combined surfaces. Figure 2.30 shows the height of the summits from two different surfaces in contact that, as an example, were assumed to follow a Weibull distribution and the distribution that results from the convolution of those functions. As expected, the equivalent surface will have higher summits and a wider range of heights.

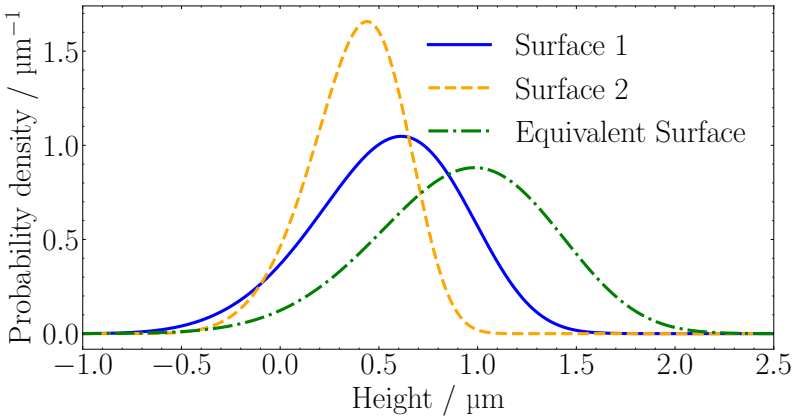


Figure 2.30: Example of the process to obtain the equivalent surface.

This convolution often does not have an analytical solution, so it is solved numerically. After this process is done, to ensure that $f(s)$ is a probability distribution function, $f(s)$

is normalized to ensure that the integral of the resulting function is one, meaning that:

$$\int_{-\infty}^{\infty} f(s)ds = 1 \tag{2.46}$$

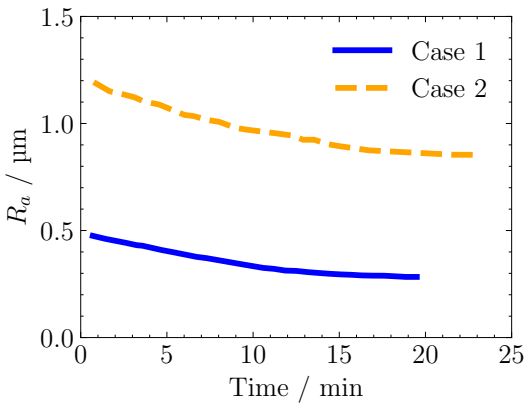
Chapter 3

Running-in, Wear and Friction

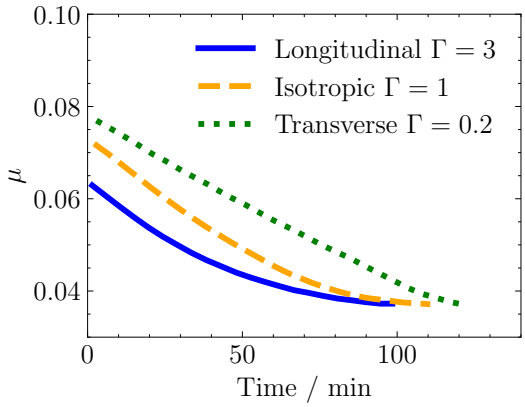
3.1 Running-in

While the concept of running-in is not very consensual [29], it is generically defined as the process in which the wear rate, surface roughness or friction reaches equilibrium by smoothing and deforming the asperities [29]. That means that, for gears, there is a reduction of the surface roughness (Figure 3.1a) and coefficient of friction (Figure 3.1b) until it reaches a steady-state value.

Running-in is not only a process of reducing the parameters previously referred, it is a process where the micro-geometry of the surfaces conform with each other, so if the relative position of the run-in surfaces change, the hydrodynamic performance can be reduced [30].



(a) Evolution of the roughness over time - Data from [23].



(b) Evolution of the friction over time - Data from [23].

Figure 3.1: Example of the influence of the running-in process in the roughness and friction.

In the Tribology Handbook [31], the procedures to run-in components like piston rings, gears, and cams are explained. Since the main focus of this thesis are spur gears and they

are one of the components with a higher need for the running-in process, it is crucial to understand how it works and what the recommendations and consequences of the running-in process of gears are. For gears it is recommended to avoid [31]:

- High speeds and high loads, causing high temperatures and scuffing;
- Low speed and high loads, causing poor elastohydrodynamic conditions and plastic flow;
- High speed and shock loading, causing scuffing.

To monitor the progress of running-in [31], it is important to be aware of the oil temperature, oil composition (presence of debris and remaining additives), surface roughness and gear efficiency. In Figure 3.2 is shown the influence of an unsuccessful running-in process in the oil temperature, where severe conditions lead to a great increase in the oil temperatures.

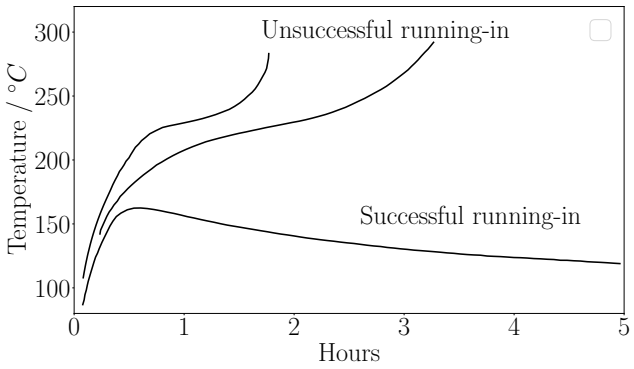


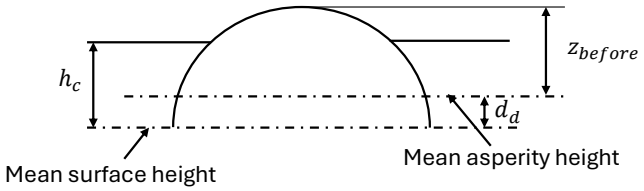
Figure 3.2: Evolution of the temperature during the running-in - Adapted from [31].

To evaluate the running-in process in lubricated spur gears, Fernandes [1] uses a FZG test rig to measure both the evolution of coefficient of friction and surface roughness over time.

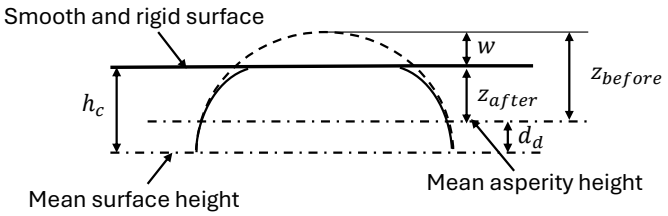
This running-in happens because the two new surfaces only contact at the highest summits, creating a smaller contact area than the theoretical one. This leads to higher contact pressure in the asperities, and consequently a smoothing of those summits due to wear, and elastic, and plastic deformation (Figure 3.3), reducing the roughness and increasing the specific film thickness [1]. During this process, the surfaces are subject to wear, whose severity depends on several factors [32]:

- Surface roughness;
- Environmental factors;
- Material properties;

- Load applied;
- Operating speeds.



(a) Before contact.



(b) After contact and plastic deformation.

Figure 3.3: Schematics of an asperity - Based on [33].

Where, in Figure 3.3, h_c is the central film thicknes, w is the displacement and d_d is the difference between the mean surface height and mean asperity height.

Besides the surface and wear rate, the friction also changes. This change occurs because the roughness change leads to a variation in the specific film thickness, that is, a change in the lubrication regime. This variation will influence the temperature due to the frictional heat generated and the formation of oxide films [34].

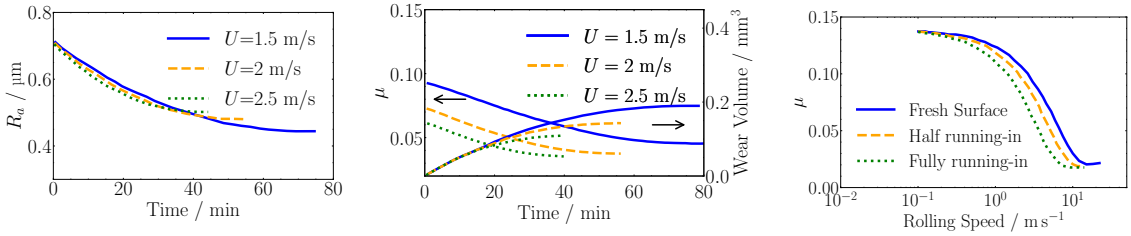
With the running-in process clearly defined, it is essential to recognize how certain parameters affect the steady-state properties and the duration of the running-in process.

From the work of Blau [34], it is shown that the number of cycles to friction reach steady-state tends to be higher than number of cycles needed for a constant wear rate. This fact could be important to model the running-in process, in order to choose a stopping criterion and ensure that the running-in phase is completed.

Since this process is characterized by the deformation (both elastic and plastic) and wear of the peaks, it is proven, by Scanning Electron Microscope (SEM), that the valleys do not change and that the hardness of the material has a great influence on the reduction of the roughness [30].

The easiest parameters to tune in a running-in process are the speed and load applied to the contact, so Akbarzadeh uses his model, for linear contacts, to do a parametric study on the running-in of a line contact [23].

In Figure 3.4, it is shown the influence of the rolling speed. With the increase of the speed, the duration of the process, friction and wear volume are reduced, but it leads to an increase in the roughness after the running-in. Those results are expected because a higher speed creates a higher film thickness, protecting more asperities, resulting in a higher final roughness. The increase of the load decreases the final roughness and increases the wear rate (Figure 3.5). This shows the importance of choosing the right parameters to optimize the process of running-in. First of all, it is necessary to conjugate the final result with the time (number of cycles) needed for the process. Besides that, higher speeds, which generate a higher specific film thickness, also generates large quantities of heat that can cause problems to the contact. Still, the lower specific film thickness generated by the lower speeds are also problematic, it can cause scuffing and severe damage. In a similar way, an extreme load on the contact reduces the film thickness resulting in scuffing or pitting of the surface [23].



(a) Influence of the rolling speed in the surface roughness during running-in.

(b) Influence of the rolling speed in friction and wear volume during running-in.

(c) Stribeck curves during running-in.

Figure 3.4: Influence of the rolling speed in the running-in process - Data from [23].

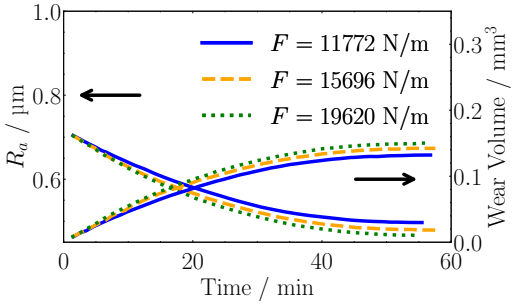


Figure 3.5: Influence of the contact load in the running-in process - Data from [23].

3.2 Wear mechanisms

During its life, a mechanical component suffers what is called wear, until it reaches the end of life. Wear is the damage that a solid surface, in our case metals, suffers and is associated with the removal and displacement of the material in the surface because of the relative movement of the surfaces [8].

In a quest to categorize the wear of a mechanical component, Varenberg tries to unify the categorization of wear [35]. He characterizes wear by answering three questions, "why", "how" and "where". The first question, "why" is answered by dividing wear on five classes shown by Figure 3.6 [35]:

1. *Fretting* (Oscillating in the work of Poletto [8]) - relative cyclic motion between two solid bodies;
2. *Sliding* - relative one-directional motion between two solid bodies;
3. *Rolling* - relative motion between two non-conforming solid bodies;
4. *Impact* - relative motion caused by the contact of two bodies where one comes out of contact;
5. *Flow* - relative motion between a body and a fluid.

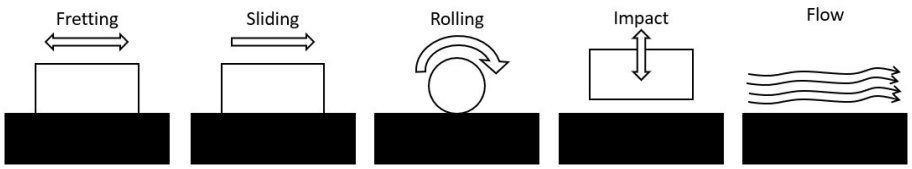


Figure 3.6: Relative motion - Adapted from [35].

To answer "how", it is important to understand that the relative movement generates work that must be dissipated. Since the amount of dissipated energy is related to how the surface is damaged, it can be used to characterize it. That work can generate defects in the bodies or heat, increasing their interaction with the environment. Those defects can be separated into two groups, *Storage of defects* when the defects accumulate in specific positions, and *Motion of defects* when the defect leaves the body. The generated heat can increase the *Chemical interaction* or *Physical interaction* [35]. Figure 3.7 illustrates how the surface disturbance is grouped.

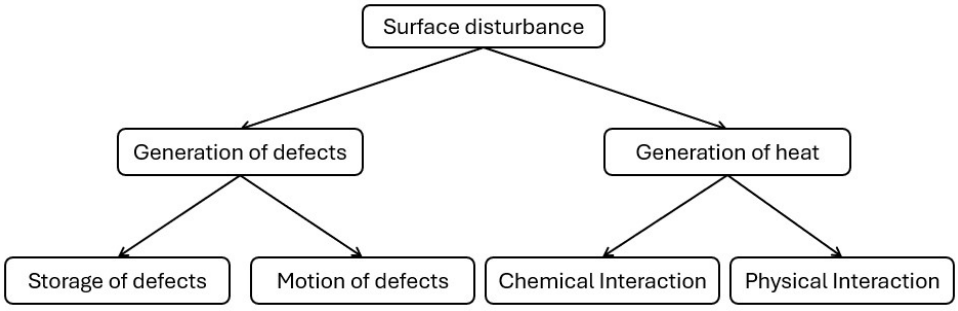


Figure 3.7: Surface disturbance - Adapted from [35].

The last question, "where" is answered by dividing it into *Normal state* and *Pathological state*. In *Normal state*, the wear is located in the outer surface layers due to the formation

and destruction of secondary surface films, while in *Pathological state*, the wear is due to the lack of film thickness [35]. With those classifications, Varenberg creates a 3D classification space, which can be reduced to the Table 3.1 3.2, and 3.3. Tribo-chemical wear is caused by the electrochemical reactions that happen between the surface and environment [8]. This type of wear englobes the other types of wear, and under certain circumstances can even be beneficial because generates a continuous self-regenerating protective layer (called secondary surface), which stops the destruction of the main surface [35]. In situations where the corrosion is harmful or when the wear debris removes the protective layer, the surface's wear is accelerated [8].

Table 3.1: Categorization of the normal wear types [35].

Types	**Generation of defects**		**Generation of heat**	
of Wear	**Storage**	**Motion**	**Chemical interaction**	**Physical interacton**
Fretting **Sliding** **Rolling** **Impact** **Flow**			Tribo-chemical wear	

Table 3.2: Categorization of the generation of defects of the pathological wear types - Adapted from [35].

Types	**Generation of defects**	
of Wear	**Storage**	**Motion**
Fretting	Fretting fatigue	Fretting wear
Sliding	Fatigue Wear	Abrasive wear
Rolling	Pitting	Solid-particle crushing
Impact	Impact wear	Solid-particle crushing
Flow	Liquid-impact erosion	Solid-particle erosion

Table 3.3: Categorization of the generation of heat of the pathological wear types - Adapted from [35].

Types	**Generation of heat**	
of Wear	**Chemical interaction**	**Physical interacton**
Fretting	Fretting wear	Fretting wear
Sliding	Abrasive wear	Adhesive wear
Rolling	Solid-particle crushing	Adhesive wear
Impact	Solid-particle crushing	Adhesive wear
Flow	Solid-particle erosion	Ablation erosion

Fretting fatigue and fretting wear normally work together, being one of them the dominant, they appear due to the vibration and temperature variation in a nominally motionless contact and, as a consequence, they are caused by oscillatory movements, not having signs of sliding direction. A sign of fretting fatigue and fretting wear is the high presence of powder oxide debris and fatigue cracks in the contact area [35].

The cyclic stress, slightly below the surface, develops and propagates cracks to the surface, resulting in fatigue wear in contacts with sliding, pitting with rolling motion and impact wear with impact motion [35]. While these types of motions can be present separately, in many systems these three motions are seen simultaneously, subjecting the surface to all of these wear types.

Fatigue wear has a crucial role in the surface's wear, once most of the other wear types can be mitigated by an appropriated lubrication system. The justification for this is that the fatigue is related with the stresses in the contact that are uneffected by the lubrication [8].

When the contact is subjected to sliding motion, some cavities called pits can develop, also known as pitting. It can be categorized by its scale (micropitting and macropitting) and by its location (surface and subsurface pitting). Micropitting are microcracks and microcraters in the asperity-scale, common in contacts in mixed and elastohydrodynamic lubrication, while macropitting creates bigger cracks and pits [8].

The asperities or hard particles of one surface scratches the other surface leaving marks in the sliding direction, that are called abrasive wear [35]. The abrasive wear is divided as two-body when only two bodies are in contact and three-body, when, beside the two main bodies in contact, there are the presence of a third body (particles, fluid or both) in the interior of the contact [35].

The heat generated in a contact subjected to sliding, rolling or impact will promote the physical interaction, leading to adhesion between the surfaces. In the literature, several theories try to explain this phenomena. The mechanical-interlocking theory claims that the origin of these forces is the interlocking of asperities, the absorption theory where the origin are the intermolecular and intramolecular forces, the diffusion theory, where the atoms diffuse from one surface to the other and electronic theory blames the electrostatic forces. The adhesion wear is very common in situations in which the lubrication is inappropriate [35].

Solid-particle crushing is caused by the hard particles trapped in the middle of the contact, similar to abrasive hear [35]. The flow-related wear is related to the bombardment of the surface with fluids (Liquid-impact erosion), particles (Solid-particles erosion) or gas or electric charges (Ablation erosion).

3.2.1 Wear calculation

Although the wear rate is not constant during the running-in process, it is important to understand the steady-state phenomena first for a dry contact and then expand it to

mixed lubrication contacts.

To calculate the wear volume V, the most used method is Archard's equation (equation (3.1)), where K is a proportionality constant, also known as Achard's wear coefficient, H is the hardness and L is the sliding distance [32].

$$V = K\frac{F_n L}{H} = K\frac{F_f L}{\mu H} \tag{3.1}$$

From equation (3.1), the wear volume and the energy dissipated by friction ($F_f L$) are directly proportional [32]. As referred by Akbarzadeh [23], the accuracy of this equation depends on the selection of an appropriate value for K. After that, the equation was expanded by Rowe to take into account the effectiveness of lubricant [23].

$$V = K_m \alpha L\frac{F_T}{H} \tag{3.2}$$

Where K_m is a dimensionless constant, dependent on the materials in contact and independent on the lubricant and α is the ratio of the number of sites on the friction surface unoccupied by molecules (N_m) and total number of sites on the friction surface (N_r), that is:

$$\alpha = \frac{N_m}{N_r} \tag{3.3}$$

Beheshti and Khonsari [36], presented a similar method to account for the presence of lubricant. Based on the theory of thermal desorption, uses a Ψ parameter, that is the probability of two asperities entering in contact, without the presence of any lubricant molecule. Ψ depends on the lubricant and the surface temperature, being calculated by equation (3.4). Having in consideration that only some of the load is carried by metal-to-metal contact, the wear is given by equation (3.5), where K_I is the wear coefficient in mixed lubrication regime, a_χ is the diameter if the area associated with an absorbed molecule, t_0 is the fundamental time of vibration of the molecule in the absorbed state, E_a is the heat absorption of the lubricant in the surface, R_g is the gas constant, and T_s is the absolute temperature of the surface.

$$\Psi = 1 - \exp\left\{-\left[\frac{a_\chi}{v_g t_0}\exp\left(-\frac{E_a}{R_g T_s}\right)\right]\right\} \tag{3.4}$$

$$V = \left(\frac{K\Psi}{\gamma_2}\right)\frac{F_n L}{H} = K_I \cdot \frac{F_n L}{H} \tag{3.5}$$

Both K and K_I can be experimentally determined on pin on disk dry sliding test or be calculated using numerical models [36]. From the literature, wear particles are generated as a consequence of contact fatigue (Figure 3.8). That leads to consider the wear coefficient (K) as 1/3 of the probability of, when two asperities contact each other, a wear fragment is created [37].

Further analysis indicates that there is a link between fatigue and sliding wear, where the wear coefficient is 1/3 of the inverse of the number of cycles necessary to break an asperity. With that relation, the wear coefficient can be estimated with a fatigue analysis of the asperities [37].

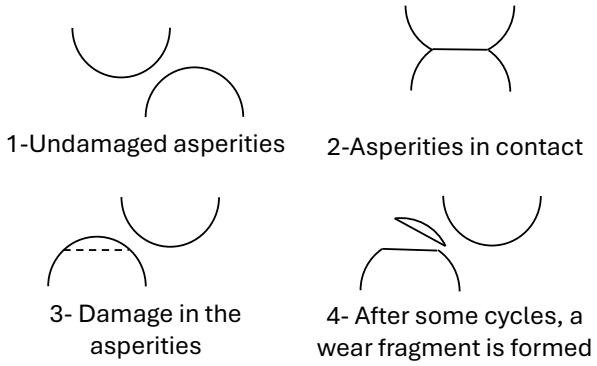


Figure 3.8: Schematic of the wear of an asperity - Adapted from [37].

3.2.2 Gear wear

In the normal functioning of gears, there will be present rolling, sliding and impact motion. Rolling and sliding during the contact of the teeth and possible impact in the meshing point. So the main wear problems of gear will be related to these three types of motion.

In gear's wear, the term scuffing is used to refer to adhesive wear. While non-consensual, some authors also use the term scoring to adhesive wear and others to abrasive wear [8].

Podgornik [38] defines scuffing as the damage occurring due to the solid-phase welding between the surfaces caused by the extreme temperature surface, where the surface becomes rough and heavily deformed, increasing vibration, noise and friction. On the other hand, scoring is the tearing out of small particles that were welded together because of a lubrication failure in the contact. Podgornik differentiates them between wear causing material transfer, scoring, and the wear causing plastic deformation due to the high temperatures, scuffing [38].

The impact wear originated in the meshing process or if the system is subjected to shock load. The impact caused in the meshing process is dependent on the contact ratio, a higher contact ratio results in a smoother meshing process and, as a consequence, lower impact.

While the wear can sometimes lead to very small cracks and pits, they grow, initiating bigger problems, that, in the last instance, lead to the fracture of a gear's tooth.

3.3 Coeficient of friction

The coefficient of friction is a crucial parameter when analyzing mechanical components in relative movement. In gears, friction is highly related to the power loss and wear of gearboxes [2]. Moreover, as discussed in Section 3.1, there is a reduction of the coefficient of friction during the running-in. As a consequence, it is important to be able to estimate the coefficient of friction.

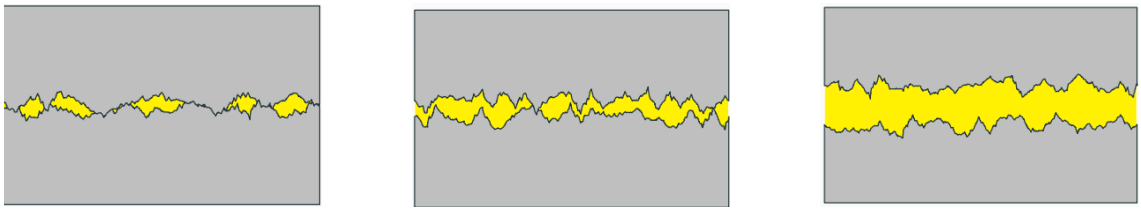
In literature, the coefficient of friction can be estimated using the load sharing concept developed by Johnson [3]. The approach used in this thesis applies the concept numerically, while, in several sources, an empirical approach is used.

However, the empirical methods are crucial because they are backed up with experimental data, and define a equation for the coefficient of friction that, has a reduced accuracy, but it is simpler and faster than the model.

Before introducing the models, it is important to understand the concept of lubrication regime and specific film thickness (Λ) that relates the film thickness (h) with the roughness of the surface (equation (3.6)). The lubrication regimes are called boundary lubrication, mixed lubrication, and elastohydrodynamic lubrication.

In the boundary lubrication regime, Λ is very small ($\Lambda < 0.7$ for gears [39]) and exists contact between the asperities, which leads to a higher friction (Figure 3.9a). On the contrary, in the elastohydrodynamic lubrication ($\Lambda > 2.0$ [39] for gears), a full separation of the bodies is achieved, leading to a high value of Λ and smaller friction (Figure 3.9c). Between those regimes, the contact is in the mixed lubrication regime, where the surfaces are not fully separated and some metal-to-metal contact still exists (Figure 3.9b).

$$\Lambda = \frac{h}{R_q} \tag{3.6}$$



(a) Boundary lubrication regime

(b) Mixed lubrication regime

(c) Elastohydrodynamic regime

Figure 3.9: Lubrication regimes [40].

The Stribeck curve plots the friction as a function of the entrainment speed (Figure 3.10), where the different regimes can easily be differentiated.

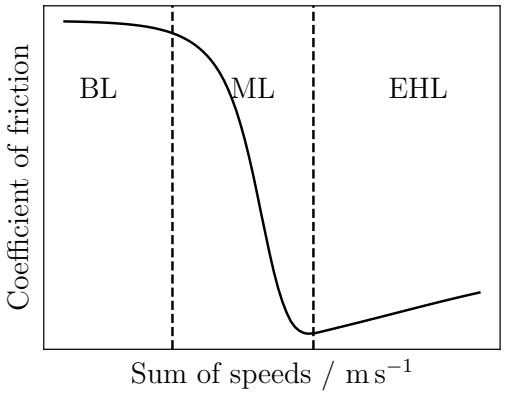


Figure 3.10: Stribeck curve.

3.3.1 Load Sharing Concept

The Load sharing concept states that, in a mixed lubricated regime, the load (F_n) is carried in some part by the asperities (F_c) and the remaining carried by the lubricant(F_H). Which means:

$$F_c = \frac{F_n}{\gamma_2} \tag{3.7}$$

$$F_H = \frac{F_n}{\gamma_1} \tag{3.8}$$

$$F_n = F_c + F_H \Leftrightarrow F_n = \frac{F_n}{\gamma_2} + \frac{F_n}{\gamma_1} \Leftrightarrow 1 = \frac{1}{\gamma_2} + \frac{1}{\gamma_1} \tag{3.9}$$

Where γ_1 and γ_2 are the lubricant and asperity load carrying factor, respectively. This method is the base of the work of Gelinck and Schipper [41], Akbarzadeh [23] and Faron [19]. This thesis will implement this method, so it will be discussed in more detail in the next chapters. Yet, to give a general idea, after γ_1 and γ_2 are calculated, the coefficient of friction is given by [23]:

$$F_f = \mu F_n = F_{f,H} + F_{f,c} \Rightarrow \mu F_n = F_{f,H} + \mu_c F_c \Rightarrow \mu = \frac{F_{f,H} + \mu_c F_c}{F_n} \tag{3.10}$$

Where F_f is the friction force, $F_{f,H}$ is the hydrodynamic friction force, $F_{f,c}$ is the asperities friction force, μ_c is the coefficient of friction of the asperities and μ is the coefficient of friction.

$F_{f,H}$ depends on the rheological behaviour of the lubrication. Akbarzadeh considers a Newtonian lubricant [23] and after expanding it to a shear thinning lubricant, while Gelinck and Schipper [41] and Faron [19] consider a lubricant behaviour following the Ree-Eyring's fluid model.

3.3.2 Empirical Methods

A different approach used in the literature is to characterize the friction by adjusting a parameter X of equation (3.11). This approach states that the friction in a contact is partly caused by the asperities' contact and in part by the elastohydrodynamic lubrication. The relevance of this approach is that typically is used reference values for the coefficient of friction in the boundary and elastohydrodynamic lubrication (μ_{BL} and μ_{EHL}, respectively) [42]. In literature, X is commonly defined as the ratio between the real contact area and the Hertzian contact area [43].

$$\mu = X\mu_{BL} + (1 - X)\mu_{EHL} \tag{3.11}$$

Rearranging equation (3.11), an equation to compute X as a function of the coefficients of friction in the boundary, mixed, and elastohydrodynamic lubrication regimes is obtained (equation (3.12)).

$$X = \frac{\mu - \mu_{EHL}}{\mu_{BL} - \mu_{EHL}} \tag{3.12}$$

Greenwood and William [4] considering an exponential (equation (3.13)) and Gaussian (equation (3.14)) distributions for the summit heights, to estimate the value of X, where c is related with the fact that the surface standard deviation is different from the summit standard deviation, but normally is used the value of 1 [44], and $F_{3/2}$ is calculated with equation (4.45). Both equations follow the limitation of the Greenwood and Williamson's model, that considers one rough surface in contact with one flat surface.

$$X = e^{-c\Lambda} \tag{3.13}$$

$$X = \frac{F_{3/2}(c\Lambda)}{F_{3/2}(0)} \tag{3.14}$$

Solving that limitation, the contact of two rough surfaces is considered in the work of Greenwood and Tripp model [45] from where equation (3.15) is obtained, $F_{5/2}$ is calculated with equation (4.45).

$$X = \frac{F_{5/2}(c\Lambda)}{F_{5/2}(0)} \tag{3.15}$$

With Bush's model, where the asperities are considered paraboloids with height peaks following a Gaussian distribution [46], the equation (3.16) is obtained. Coy [47] used a linear approximation to calculate the coefficient of friction, where $X = 0$ for $\Lambda > 3$ (equation (3.17)) [44].

$$X = \operatorname{erfc}\left(\frac{\Lambda}{\sqrt{2}}\right) \tag{3.16}$$

$$X = \left(1 - \frac{\Lambda}{3}\right) \tag{3.17}$$

Doleschel [48] approximates the asperity interaction only occurs for $\Lambda < 2$ and applied a second order polynomial function (equation (3.18)) to the calculation of X, where Λ_a is in Table 3.4 [42].

$$X = \left(1 - \frac{\Lambda_a}{2}\right)^2 \tag{3.18}$$

Other authors also developed some equations adjusted to experimental values, but with a more restrict applicability (equations (3.19), (3.20) and (3.21))[44].

$$X = 1 - 0.84\Lambda^{0.23} \tag{3.19}$$

$$X = 1 - \frac{1.21\Lambda^{0.64}}{1 + 0.37\Lambda^{1.26}} \tag{3.20}$$

$$X = \left(1 - \frac{\Lambda}{4}\right)^{6.804} \tag{3.21}$$

Matsumoto and Morikawa [49] points that R_z is more related with the coefficient of friction and it is used to calculate the specific film thickness. So in equation (3.22), the Λ used is stated in Table 3.4. Following the work of Diab et al [50], Arana et al. [43] proposed the equation (3.23) to achieve a better result having in consideration the measured limits, that is, $X(\Lambda = 0) = 1$ and $X(\Lambda \approx 2) = 0$ [43], with Λ defined in Table 3.4.

$$X = \frac{1}{2}\log_{10}\left(\frac{1}{\Lambda_m}\right) \tag{3.22}$$

$$X = 1 - \mathrm{erf}(\Lambda) \tag{3.23}$$

Taylor and Sherrington [44] expanded the concept of S-curve, more specifically the reverse S-curve (equation (3.25)), used to model growth/decay processes to be applied in mixed lubrication, and then they compared it to other equations to calculate X. However, before them, Oliver and Spikes [51] had already used an equation similar to the S-curve (equation (3.24)). Concerning k and a from equation (3.25) were obtained by fitting the data using the sum of the normalized squares of the difference between the curve and the experimental data, resulting in $k = 1.453$ and $a = 1.32$.

$$X = \frac{1}{(1+\Lambda)^2} \tag{3.24}$$

$$X = \frac{1}{(1+\Lambda^k)^a} = \frac{1}{(1+\Lambda^{1.453})^{1.32}} \tag{3.25}$$

In Fernandes's equation (equation (3.26)), the constant a and b are adjusted based on experimental data, but is possible to use just one without significant differences. While a shifts the curve vertically, b introduces an inflection point [42]. In his work, Fernandes corrects the film thickness due to the temperature effect (ϕ_T) (Table 3.4).

$$X = \frac{1}{e^{a \cdot \Lambda^b}} \tag{3.26}$$

Table 3.4: Specific Film thickness - Adapted from [42].

Author	Specific Film Thickness	Domain
Dolleschel	$\Lambda_a = \frac{2\phi_T h_0}{R_{a_1}+R_{a_2}}$	$\Lambda_a \in [0,2]$
Diab	$\Lambda = \frac{\phi_T h_0}{\sqrt{R_{q_1}^2+R_{q_2}^2}}$	$\Lambda \in [0,3]$
Masumoto	$\Lambda_m = \frac{\phi_T h_m}{R_{z_1}+R_{z_2}}$	$\Lambda_m \in [0.01,1]$
Arana	$\Lambda = \frac{\phi_T h_0}{\sqrt{R_{q_1}^2+R_{q_2}^2}}$	$\Lambda \in [0,2]$

The experimental values used by Taylor and Sherrington [44] were obtained by using Mini Traction Machine with Spacer Layer Imaging (MTM-SLIM) and Fernandes [42] by using an EHD2 Ultra Thin Film Measurement System (Figure 3.11), both in a contact with a disk and a sphere.



Figure 3.11: EHD2 Ultra Thin Film Measurement System [52].

With all of those equations previously described is clear a lack of coherence in the calculation of Λ parameter, where different parameters are used, and much of them result in the adjustment of a curve to experimental data, lacking precision when compared with each other and when usind in slightly different conditions.

3.3.3 Coefficient of friction in gears

The contact between two gears can be modelled as the contact between two cylinders (Figure 3.12) where, along the line of action, the radius of each cylinder and the number of pairs of teeth change and consequently, the coefficient of friction at each point of the line of action will change. Since it is not easy to experimentally measure the friction along the line of action, a constant mean value is typically used (μ_{mZ}).

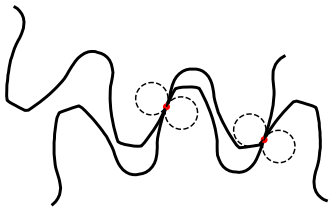


Figure 3.12: Contact between two gears - Adapted from [18].

The measurement of μ_{mZ} can be done in two different ways. The first one uses a FZG gear test rig (Figure 3.13), seen in the works of Fernandes et al. [2] and a two-disk machine (Figure 3.14), seen in the work of Akbarzadeh and Khonsari [23], Moder et al. [53] and Diab et al. [54]. In those equipments, can be mounted a mechanism to measure the roughness of the tooth without the need to dismount the gears, shown in Figure 3.15.

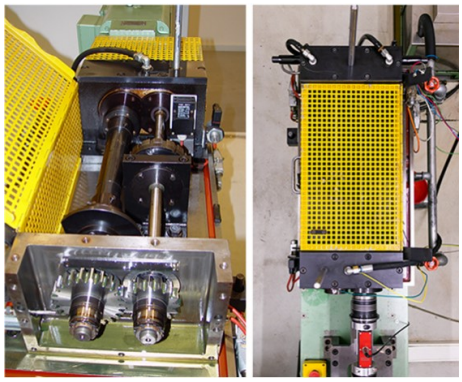


Figure 3.13: FZG gear test rig [1].

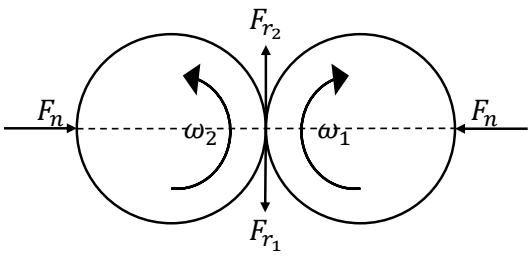


Figure 3.14: Scheme of a two disk machine - Adapted from [53].

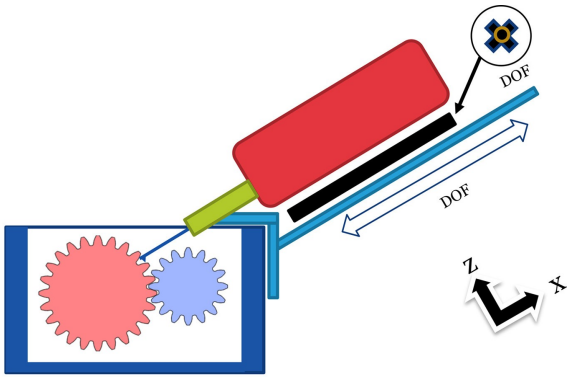


Figure 3.15: Schmatic of the measuring system [55].

In a two-disk machine, two rotating disks are put in contact and the friction is measured, but to have valid results to be compared with gears, the radius of the disks must be changed.

In a different approach, the FZG gear test rig uses gears to measure the power loss and then relate it with the coefficient of friction. The power loss is defined by [2]:

$$P_V^i = P_{VZ0} + P_{VZP}^i + P_{VL}^i + P_{VD} \tag{3.27}$$

Where P_V^i is the total power loss, P_{VZ0} is the load-independent power loss, P_{VZP} is the load-dependent power loss, P_{VL}^i is the rolling bearings power losses and P_{VD} is the seals power losses.

Both P_{VL} and P_{VD} can be estimated by several models, but P_{VZ0} can only be calculated in specific conditions, so it is measured experimentally. P_{VZP} can be calculated at each meshing point using equation (3.28).

$$P_{VZP}(x) = F_n(x) \cdot \mu_Z(x) \cdot v_g(x) \tag{3.28}$$

Integrating over the line of action (between the point A and point E), the load-dependent power loss is obtained by equation (3.29), where v_g is the sliding speed.

$$P_{VZP} = \frac{1}{p_b} \int_A^E F_n(x) \cdot \mu_z(x) \cdot v_g(x) dx \tag{3.29}$$

Considering a constant friction (μ_{mZ}) along the path of contact and working the equation (3.29) [2]:

$$P_{VZP} = \mu_{mZ} \cdot F_{bt} \cdot v_{tb} \cdot \frac{1}{p_b} \int_A^E \frac{F_n(x)}{F_{bt}} \cdot \frac{v_g(x)}{v_{tb}} dx \tag{3.30}$$

Where $\frac{1}{p_b} \int_A^E \frac{F_n(x)}{F_{bt}} \cdot \frac{v_g(x)}{v_{tb}} dx$ is the gear loss factor H_{VL}, F_{bt} and v_{bt} are, respectively, the gear tangential force and speed on the base plane. Using a FZG gear test rig (Figure

3.13), and measuring the power loss, the coefficient of friction is calculated with equation (3.31) [2].

$$\mu_{mZ}^{exp} = \frac{P_V^{exp} - (P_{VZ0} + P_{VL} + P_{VD})}{P_{in} H_{VL}} \tag{3.31}$$

Based in the work of Schlenk, in the ISO 14179-2 is stated the most used expression to calculate μ_{mZ} [2].

$$\mu_{mZ} = 0.048 \left(\frac{F_{bt}/b}{v_{\Sigma C} \cdot R_{xC}} \right)^{0.2} \eta^{-0.05} R_a^{0.25} X_L \tag{3.32}$$

Where $v_{\Sigma C}$ is the sum of speeds at the pitch point, η is the dynamic viscosity and α is the pressure-viscosity coefficient of the lubricant, R_{xC} is the equivalent radius at the pitch point, b is the face width and X_L is the lubricant factor.

Fernandes et al. [2] tried to apply the concept of load sharing to gears, using the modified Hersey parameter (S_p) previously used by Brandão et al. [56]. This parameter is then adapted to gears (equation (3.33)). With experimental data, it is shown that X has a linear dependence with $\log(S_p)$, but only takes into account the lubrication conditions, so it includes a gear geometric parameter (S_g).

$$S_p^{gear} = \frac{v_{\Sigma C} \cdot \eta \cdot \alpha^{1/2}}{F_{bt}^{1/2}} \tag{3.33}$$

S_g tries to include the contact geometry in the equation, taking into account the surface finishing, face width (b), equivalent radius at the pitch point(R_{xC}), contact ratio (ϵ_α) and base helix angle (β_b) (equation (3.34)). With the Buckingham theorem the exponents of equation (3.35) were obtained. So X is defined by equation (3.36).

$$S_g = \frac{R_a^{A_g}}{R_{xC}^{B_g} \cdot (\epsilon_\alpha b \cos\beta_b)^{C_g}} \tag{3.34}$$

$$S_g = \frac{R_a}{(R_{xC} \cdot \epsilon_\alpha b \cos\beta_b)^{1/2}} \tag{3.35}$$

$$X = 0.5 \log(S_p S_g \cdot 10^9) \tag{3.36}$$

After that, Fernandes et al. [2] also simplified the procedure referring that since μ_{mZ} is linearly dependent of $m \log(S_p S_g \cdot 10^9) + b$, it could be defined as:

$$\mu_{mZ} = 0.014 \left(\frac{1}{S_p} \right)^{1/4} S_g^{1/4} \cdot X_L \tag{3.37}$$

Chapter 4

Mixed lubrication model

To develop a model to calculate the coefficient of friction it is important to first introduce some concepts that will be useful to understand and implement the model in Python. As is well known, gears normally work in a mixed-lubricated regime. Yet, as will be explained later, it is important to understand the full film lubrication and boundary lubrication regimes.

In order to simplify the explanation, a line contact will be considered, and then expanded to gears. In the Appendix A, a model for the elliptical contact is explained that will be used to validate the model with ball-on-disk experimental results. An elliptical contact is also useful for gears with crowning modifications.

4.1 Hertzian contact

In a contact problem, the Hertzian properties are normally the most important ones and essential to implement more complex models (example in Figure 4.1). Those properties are the reduced radius (R_x), reduced elasticity modulus (E'), Hertzian pressure (p_h), contact half-width (a) and the nominal contact area (A_c), being calculated with equations (4.1) to (4.5).

$$R_x = \left(\frac{1}{R_{x1}} + \frac{1}{R_{x2}}\right)^{-1} \tag{4.1}$$

$$E' = \left[\frac{1}{2}\left(\frac{1-\nu_1^2}{E_1} + \frac{1-\nu_2^2}{E_2}\right)\right]^{-1} \tag{4.2}$$

$$p_h = \sqrt{\frac{F_n E'}{2\pi b R_x}} \tag{4.3}$$

$$a = \sqrt{\frac{8}{\pi}\frac{F_n R_x}{b E'}} \tag{4.4}$$

$$A_c = 2ab \tag{4.5}$$

Where R_{xi} is the contact radius, ν_i is the Poisson ratio, E_i is the Young's modulus, all referent to the body i, and b is the gear width.

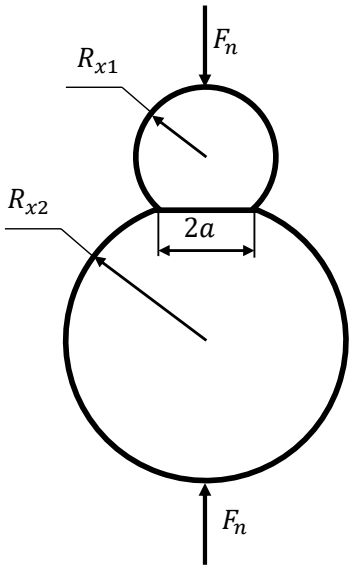


Figure 4.1: Contact between two cylinders - Adapted from [57].

4.2 Elastohydrodynamic Lubrication (EHL)

Under elastohydrodynamic lubrication conditions, the study of the physical properties of the lubricant is of extreme importance.

4.2.1 Lubricant properties

The experimental results used in Chapter 5 to validate the model were obtained using the lubricant PAO ISO VG 150, so it is important to measure the physical properties. Firstly will be discussed the lubricant properties and how to calculate the film thickness under EHL conditions, and after that the lubricant behavior and how to calculate the coefficient of friction in this regime will be discussed. Table 4.1 shows the kinematic viscosity of the lubricant, and it was considered a lubricant density (ρ) of 854 kg/m^3 at 15 °C [1]. With those values and applying Vogel's Law (equation (4.6)), the Vogel's parameters are obtained (Table 4.2) and the variation of the kinematic viscosity is shown in Figure 4.2a.

$$\nu = K \exp\left(\frac{b}{\theta + c}\right) \tag{4.6}$$

Multiplying the kinematic viscosity by the density, the dynamic viscosity is obtained (η) [39].

$$\eta = \nu\rho \tag{4.7}$$

Table 4.1: Kinematic viscosity of the ISO VG 150 - Values from [1].

T / °C	ν / cSt
40	151.96
70	46.51
100	18.89

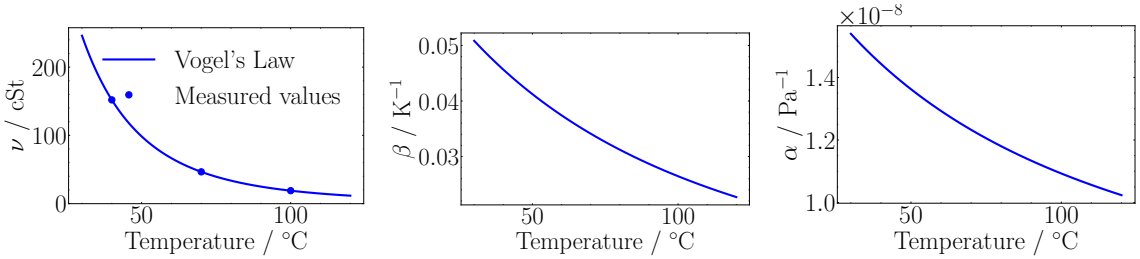
Table 4.2: Vogel's Law parameters.

Parameter	Value
K	0.02468
b	1667.31
c	151.09

The thermoviscosity (β) is calculated by applying its definition (equation (4.8)) to Vogel's law and the piezoviscosity (α) calculated with Gold's equation (equation (4.9)) with s=7.382 and t=0.1335 [42]. The thermal conductivity (k) and heat capacity (c_p) of the oil used in this thesis was considered 0.18 $\mathrm{W\,m^{-1}\,K^{-1}}$ and 2090 $\mathrm{J\,kg^{-1}\,K^{-1}}$ [58].

$$\beta = \frac{b}{(\theta + c)^2} \tag{4.8}$$

$$\alpha = s \cdot \nu^t \cdot 10^{-9} \tag{4.9}$$



(a) Influence of the temperature on the viscosity.

(b) Influence of the temperature on the thermoviscosity.

(c) Influence of the temperature on the piezoviscosity.

Figure 4.2: Temperature effects on the lubricant properties.

To account for the pressure effect in the lubricant, the Roelands' equation was applied (equation (4.10)), where T_0 is the inlet temperature of the lubricant, p_H is the hydrodynamic pressure, η_0 is the dynamic viscosity at T_0 and ambient pressure. The Roelands'

exponent for temperature (S_0) and pressure (Z) are calculated using equations (4.11) and (4.12), respectively. In Subsection 4.4.3, the model is verified with Faraon's results, where the heating in the contact is not considered, so the temperature related component of equation (4.10) becomes 1.

$$\eta(p,T) = \eta_0 \exp\left\{[\ln(\eta_0) + 9.67]\left[\left(\frac{T-138}{T_0-138}\right)^{-S_0}(1+5.1\times10^{-9}p_H)^Z - 1\right]\right\} \tag{4.10}$$

$$S_0 = \frac{\beta(T_0-138)}{\ln(\eta_0)+9.67} \tag{4.11}$$

$$Z = \frac{\alpha}{5.1\cdot10^{-9}[\ln(\eta_0)+9.67]} \tag{4.12}$$

While equation (4.10) is used in this model, Bair and Habchi [59] state that it is not accurate to preform EHL analyses using the Roelands' equation and that α is not related with the pressure, being, in reality, just a correction factor to compensate the inaccurate assumptions of the Newtonian inlet zone.

4.2.2 Line contact

4.2.2.1 Film thickness

The solution for the EHL problem must respect the Reynolds equation, considered the elasticity of the surfaces and consider the pressure generated in the contact that results in the deformation of the surface. Some solutions for the film thickness can be found in the literature, but it will be used the dimensionless numbers introduced by Downson and Higgison, and Moes [60].

From the work of Downson and Higgison, the following dimensionless numbers are introduced [41]:

$$\overline{h} = \frac{h}{R} \tag{4.13}$$

$$U_\Sigma = \frac{\eta_0(U_1+U_2)}{E'R_x} \tag{4.14}$$

$$W = \frac{F_N}{bE'R} \tag{4.15}$$

$$G = \alpha E' \tag{4.16}$$

Where U_i is the speed of the body i, $\overline{h}$ is the dimensionless film thickness, U_Σ is the dimensionless speed number, W is the dimensionless load number and G is the dimensionless lubricant number.

From those numbers, Moes proposed the Moes' dimensionless film thickness (H), Moes' dimensionless load number (M), and Moes' dimensionless lubricant number (L) [41]:

$$H = \overline{h} U_{\Sigma}^{-\frac{1}{2}} \tag{4.17}$$

$$M = W U_{\Sigma}^{-\frac{1}{2}} \tag{4.18}$$

$$L = G U_{\Sigma}^{\frac{1}{4}} \tag{4.19}$$

With those numbers, the Moes' dimensionless central film thickness (H_c) is calculated.

$$H_c = \left[\left(H_{RI}^{\frac{7}{3}} + H_{EI}^{\frac{7}{3}} \right)^{\frac{3}{7} s_M} + \left(H_{RP}^{-\frac{7}{2}} + H_{EP}^{-\frac{7}{2}} \right)^{-\frac{2}{7} s_M} \right]^{s_M^{-1}} \tag{4.20}$$

Where:

$$s_M = \frac{1}{5} \left(7 + 8 e^{-2 \frac{H_{EI}}{H_{RI}}} \right) \tag{4.21}$$

$$H_{RI} = 3 M^{-1} \tag{4.22}$$

$$H_{RP} = 1.287 L^{\frac{2}{3}} \tag{4.23}$$

$$H_{EI} = 2.621 M^{-\frac{1}{5}} \tag{4.24}$$

$$H_{EP} = 1.311 M^{-\frac{1}{8}} L^{\frac{3}{4}} \tag{4.25}$$

Each of the asymptotes presented in equations (4.22) to (4.25) represents the solution for four different problems. The RI-asymptote (equation (4.22)) represents the rigid-isoviscous solution, for which $H_c \to H_{RI}$ when $M \to 0$. The RP-asymptote (equation (4.23)) solves the heavy load problem under rigid-piezoviscous lubrication, where $H_c \to H_{RP}$ when $L \to \infty$. The EI-asymptote (equation (4.24)) is used for heavy loads under elastic-isoviscous lubrication, resulting in $H_c \to H_{EI}$ when $M \to \infty$ and $L \to 0$. Lastly, the EP-asymptote (equation (4.25)) for which the heavy load problem under elastic-piezoviscous lubrication is solved, resulting in $H_c \to H_{EP}$ when $M \to \infty$ [60].

Furthermore, heavy-loaded line contact operates in the Elasto-Piezoviscous regime, resulting in the Koets' Conditions (equation (4.26)), which must be respected to apply this method. Figure 4.3 shows the dependence of H_c on M and L and has the Koets' condition represented. The central film thickness (h_c) is calculated with equation (4.27) that was obtained by rearranging the equations (4.13) and (4.17) [41].

$$L\sqrt{M} > 13.3 \text{ and } M > 0.1 L^{\frac{2}{3}} \tag{4.26}$$

$$h_c = H_c U_{\Sigma}^{\frac{1}{2}} R_x \tag{4.27}$$

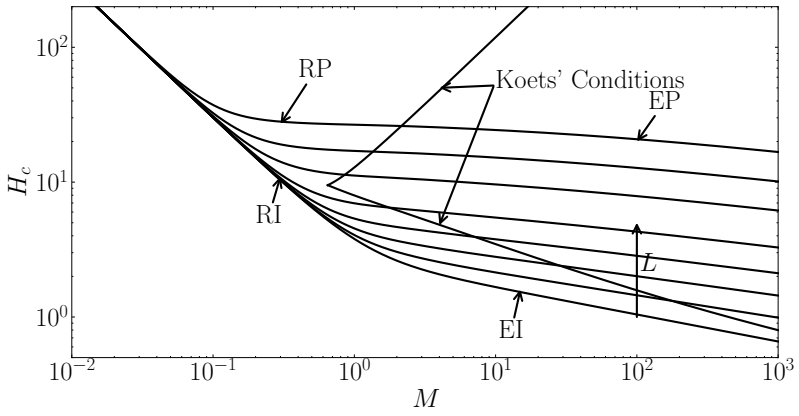


Figure 4.3: Moes' Diagram (Adpted from [41]).

4.2.2.2 Rheological behavior

In an EHL contact, the friction forces have two components: the rolling friction, due to the velocity gradient in the inlet region, and sliding friction, due to the shear stress in the lubricant. However, in EHL conditions, the rolling friction is typically negligible compared with the sliding friction [61]. So the shear stress, τ_H, is function of shear rate, $\dot{\gamma}$, so it comes that:

$$F_{f,H} = \iint_{A_H} \tau_H(\dot{\gamma})\, dA_H \tag{4.28}$$

Where A_H is the hydrodynamic contact area.

The shear stress of the lubricant depends on the rheological behaviour of the lubricant. To define that behaviour, the Deborah number, D, was introduced in the equation (4.29). The Deborah number is defined by the ratio between relaxation time and the time of passage of the lubricant in the contact area[62].

$$D = \frac{\eta/G}{a/V_e} = \frac{\eta U}{Ga} \tag{4.29}$$

Where G is the shear modulus of the lubricant and V_e is the entrainment speed. For values of $D << 1$, the viscosity behaviour is dominant, that is, the relaxation time is very small when compared with the passing time in the contact. On the other hand, for $D >> 1$, the relaxation time is much bigger than the passing time, thus the elastic behaviour is dominant [61].

In Figure 4.4, the possible rheological behaviour of a lubricant is shown. Eyring shear stress (τ_0) and limit shear stress (τ_L) represent the value at which the fluid behaves linearly and the value from which a fluid exhibits plastic behavior, respectively. Consequently, Figure 4.4 is separated into 4 zones (Elastic, Linear viscous, Non-linear viscous, and Plastic).

In Curve I, while $\tau < \tau_0$, the lubricant has a Newtonian behaviour, having a non-Newtonian behaviour near τ_0. In Curve II, a non-linear viscous fluid is present. Bell et al. (1964) applied Eyring's fluid model (equation (4.30)) to calculate $\dot{\gamma}$ [61].

$$\dot{\gamma} = \frac{\tau_0}{\eta} \sinh\left(\frac{\tau_H}{\tau_0}\right) \tag{4.30}$$

For lubricants with a curve similar to Curve III, where part of the behaviour is elastic the following formulation was introduced by Johnson and Tevaarwerk (1977), where the shear rate is the sum of the elastic shear rate and viscous shear rate [61]:

$$\dot{\gamma} = \dot{\gamma}_e + \dot{\gamma}_v = \frac{\dot{\tau}}{G} + \frac{\tau_0}{\eta} \sinh\left(\frac{\tau_H}{\tau_0}\right) \tag{4.31}$$

This new model incorporates the elastic and non-linear viscous behaviour, but incorporates as well the Newtonian behaviour when $D << 1$ and $\tau << \tau_0$ [61]. However, there is no limit to the shear stress increase. To solve this problem, Bair and Winer expanded it to consider a limit shear stress called τ_L [19].

$$\dot{\gamma} = \frac{\tau_L}{\eta} \operatorname{arctanh}\left(\frac{\tau_H}{\tau_L}\right) \tag{4.32}$$

Since in gear transmissions, $\dot{\gamma}_e$ can be neglected [43], this thesis will firstly apply the Eyring model to verify the model with results from Faraon [19] and in the experimental validation of this model will be used the model in equation (4.32).

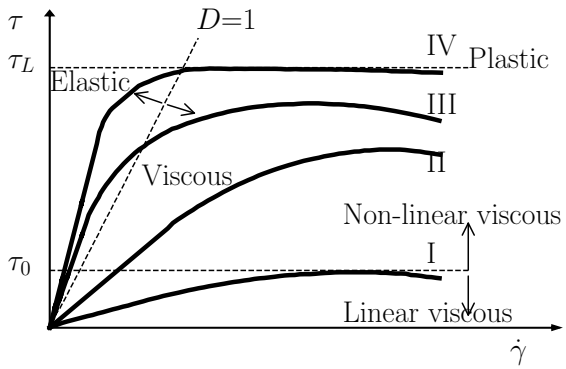


Figure 4.4: Example of traction curves of lubricants - Adpated from [61].

4.3 Boundary Lubrication

In the boundary lubrication regime, the film thickness is almost non-existent or, in some cases, even absent, resulting in the constant contact between the asperities. A trivial conclusion from this is the extreme severity of wear and friction in this regime, so it is crucial to ensure that a contact is not under the boundary lubrication regime. While

the literature demonstrates that the friction coefficient of the asperities (μ_c) changes with velocity, temperature and environment [19], it is mostly dependent on the slide-to-roll ratio (SRR), so it is considered that the coefficient of friction of the asperities follows the equation (4.33) represented in Figure 4.5 [63].

$$\mu_c = \mu_{c,max} \frac{2}{\pi} \arctan\left(\frac{\pi}{2} \frac{SRR}{S_{ep}}\right) \tag{4.33}$$

Where $\mu_{c,max}$ is the maximum value of μ_c and S_{ep} is related to the transition from the elastic to plastic behavior of the boundary layer.

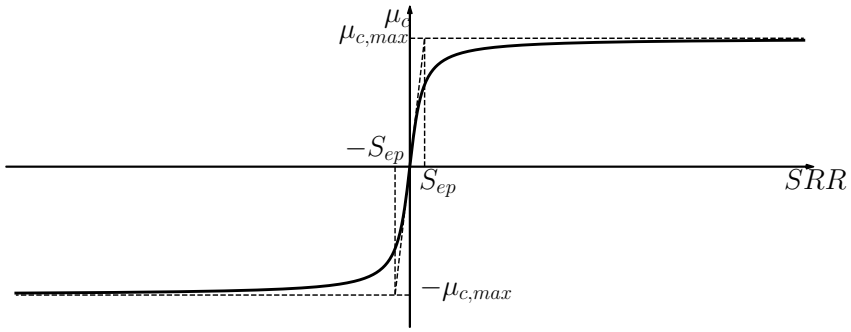


Figure 4.5: Example of the influence of SRR in the μ_c.

4.4 Mixed Lubrication-Statistical model

The mixed lubrication model implemented follows Johnson's Load Sharing Concept [3]. In that model is stated that the load carried in the contact is carried by the fluid and by the asperities (equation (4.36)) and that the asperities' load and fluid's load are, respectively, given by:

$$F_c = \frac{F_n}{\gamma_2} \tag{4.34}$$

$$F_H = \frac{F_n}{\gamma_1} \tag{4.35}$$

$$F_n = F_c + F_H \Leftrightarrow F_n = \frac{F_n}{\gamma_2} + \frac{F_n}{\gamma_1} \Leftrightarrow 1 = \frac{1}{\gamma_2} + \frac{1}{\gamma_1} \tag{4.36}$$

Following that principle, the equations to calculate the Moes' central film thickness dimensionless number are adjusted, where the parameter γ_1 was included, obtaining the equation (4.37) [19].

$$H_C = \left[\gamma_1^{s_M}\left(H_{RI}^{\frac{7}{3}} + \gamma_1^{-\frac{14}{15}} H_{EI}^{\frac{7}{3}}\right)^{\frac{3}{7}s_M} + \left(H_{RP}^{-\frac{7}{2}} + H_{EP}^{\frac{-7}{2}}\right)^{-\frac{2}{7}s_M}\right]^{s_M^{-1}} \tag{4.37}$$

Where:

$$s_M = \frac{1}{5}\left(7 + 8\mathrm{e}^{\left(-2\frac{H_{EI}}{H_{RI}}\gamma_1^{-\frac{2}{5}}\right)}\right) \tag{4.38}$$

4.4.1 Greenwood and Williamson's asperity contact model

Greenwood and Williamson's asperity model [4] was developed based on Gaussian or exponential distributions of the summit heights and considered one equivalent rough surface considering the roughness of both surfaces against one rigid smooth flat surface. The asperities are considered with a spherical tip, and all have the same radius calculated as explained in Section 2.3.

While the scope of this thesis is to apply other distributions, this chapter will focuses more in the equations for the Gaussian distribution since it is the most used distribution. Under this model, the probability of a summit contacting the other surface is given by:

$$P(s > h) = \int_h^\infty f(s)ds \tag{4.39}$$

$$f(s) = \frac{1}{\sigma_s\sqrt{2\pi}}e^{\left(\frac{-s^2}{2\sigma_s^2}\right)} \tag{4.40}$$

Where $f(s)$ is the probability density function, σ_s is the standard deviation of the summit heights, and P is the probability of a summit being higher than the central film thickness (h), which represents the probability of both surfaces contacting each other. The equations (4.41) to (4.44) are, respectively, for the calculation of the number of asperities in contact (N), real contact area (A), load carried by the asperities (F_c^{GW}) and average contact pressure in the asperities ($\overline{p_c^{GW}}$) [19].

$$N = nA_c\int_h^\infty f(s)ds = nA_c\,\mathrm{F}_0\left(\frac{h}{\sigma_s}\right) \tag{4.41}$$

$$A = \pi nA_c\beta\int_h^\infty (s-h)f(s)ds = \pi nA_c\beta\sigma_s\,\mathrm{F}_1\left(\frac{h}{\sigma_s}\right) \tag{4.42}$$

$$F_c^{GW} = \frac{2}{3}nA_cE'\beta^{\frac{1}{2}}\int_h^\infty (s-h)^{\frac{3}{2}}f(s)ds = \frac{2}{3}nA_cE'\beta^{\frac{1}{2}}\sigma_s^{\frac{3}{2}}\,\mathrm{F}_{\frac{3}{2}}\left(\frac{h}{\sigma_s}\right) \tag{4.43}$$

$$\overline{p_c^{GW}} = \frac{F_c}{A_c} = \frac{2}{3}nE'\beta^{\frac{1}{2}}\sigma_s^{\frac{3}{2}}\,\mathrm{F}_{\frac{3}{2}}\left(\frac{h}{\sigma_s}\right) \tag{4.44}$$

Where β is the average asperity radius, n is the asperity density and F_j is given by :

$$\mathrm{F}_j\left(\frac{h}{\sigma_s}\right) = \int_{h/\sigma_s}^\infty \left(\overline{s} - \frac{h}{\sigma_s}\right)^j \phi(\overline{s})d\overline{s} \tag{4.45}$$

Where $\phi(\overline{s})$ is the normalized Gaussian distribution function:

$$\phi(\overline{s}) = \frac{1}{\sqrt{2\pi}} \exp\left(\frac{-\overline{s}^2}{2}\right) \tag{4.46}$$

It is important to note that to consider a different distribution it is possible to replace $f(s)$ for the desired distribution discussed in Section 2.5.

The reference plane of the EHL model passes through the mean line of the surface, while the mean line of the summits are used as reference of the asperity model components, so that difference (d_d) must be accounted for in equations (4.47) to (4.50) (Figure 4.6) [41]. The value of d_d can be estimated directly from the roughness surface, but in the literature it is considered $d_d = 1.15\sigma_s$, that was used in this dissertation [64].

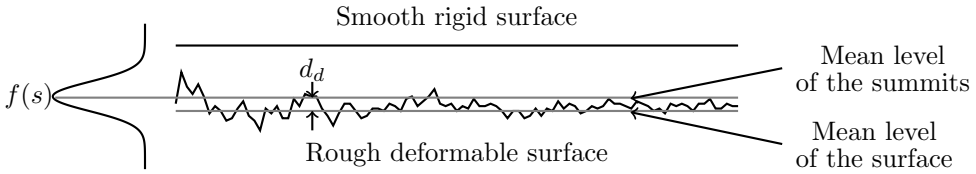


Figure 4.6: Example of the contact of one smooth surface and a rough surface that follows a Gaussian distribution - Adapted from [19].

$$N = nA_c \mathrm{F}_0\left(\frac{h-d_d}{\sigma_s}\right) \tag{4.47}$$

$$A = \pi nA_c\beta\sigma_s \mathrm{F}_1\left(\frac{h-d_d}{\sigma_s}\right) \tag{4.48}$$

$$F_c^{GW} = \frac{2}{3}nA_cE'\beta^{\frac{1}{2}}\sigma_s^{\frac{3}{2}} \mathrm{F}_{\frac{3}{2}}\left(\frac{h-d_d}{\sigma_s}\right) \tag{4.49}$$

$$\overline{p_c^{GW}} = \frac{F_c}{A_c} = \frac{2}{3}nE'\beta^{\frac{1}{2}}\sigma_s^{\frac{3}{2}} \mathrm{F}_{\frac{3}{2}}\left(\frac{h-d_d}{\sigma_s}\right) \tag{4.50}$$

Faraon [19] in his model considered the film thickness proposed by Johnson et al. [3]. This different definition for the film thickness is explained by the fact that in the model, it is considered a contact between one rough and one flat surface, instead of the two rough surfaces. When two rough surfaces are considered, the asperities of each surface can either be aligned or misaligned, so it is important to consider that and use the mean separation (h') in equations (4.47) to (4.50). Figure 4.7 shows the differences from h_c and h', and for lower speeds, a small difference between them can be noticed, but for higher speeds, that difference can be neglected.

$$h' = \int_{-\infty}^{h_c} (h_c - s) f(s) ds \tag{4.51}$$

In literature, Akbarzadeh [23], fitted the equation for the average contact pressure of the asperities in a rough line contact as proposed by Gelinck and Schipper [41], introducing

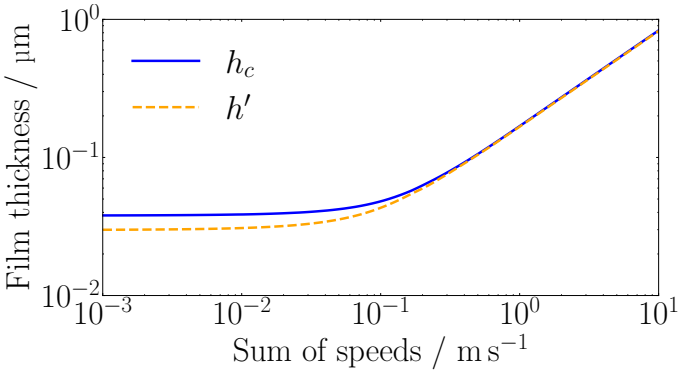


Figure 4.7: Comparision between h_c and h'.

a new formulation (equation (4.52)). On the other hand, Faraon used the equation (4.53), but no relevant difference between them was noticed [19].

$$\overline{p_c} = \frac{1}{\gamma_2}\sqrt{\frac{F_n E'}{2\pi b R_x}}\left[1+\left(1.558(nR_x\sqrt{\beta R_x})^{0.0337}\left(\frac{\sigma_s}{R_x}\right)^{-0.442}W^{0.4757}\right)^{-1.7}\right]^{-0.5882} \tag{4.52}$$

$$\overline{p_c} = p_h\left[1+(a_1\overline{n}^{a_2}\overline{\sigma_s}^{a_3})^{a_4}\right]^{1/a_4} \tag{4.53}$$

Where a_i are fit parameters ($a_1 = 0.953$, $a_2 = 0.0337$, $a_3 = -0.442$, and $a_4 = -1.70$) [19], $\overline{n}$ is the normalized asperity density (equation (4.54)) and $\overline{\sigma_s}$ is the normalized standard deviation of the summit heights (equation (4.55)).

$$\overline{n} = \frac{32}{\pi}\frac{nF_n}{bE'}\sqrt{\beta R_x} \tag{4.54}$$

$$\overline{\sigma_s} = \frac{\pi\sigma_s bE'}{8F_n} \tag{4.55}$$

The asperity pressure calculated with equations (4.50) and (4.52) must be equal. So to solve this problem, the system of equations (4.56) must be solved to obtain γ_1 and γ_2. Due to the complexity of the system, it will be solved with the numerical method defined in the Figure 4.8.

$$\begin{cases} \dfrac{2}{3}nE'\beta^{\frac{1}{2}}\sigma_s^{\frac{3}{2}}\,\mathrm{F}_{\frac{3}{2}}\left(\dfrac{h'-d_d}{\sigma_s}\right) = \\ = \dfrac{1}{\gamma_2}\sqrt{\dfrac{F_n E'}{2\pi b R_x}}\left[1+\left(1.558(nR_x\sqrt{\beta R_x})^{0.0337}\left(\dfrac{\sigma_s}{R_x}\right)^{-0.442}W^{0.4757}\right)^{-1.7}\right]^{-0.5882} \\ \dfrac{1}{\gamma_1}+\dfrac{1}{\gamma_2} = 1 \end{cases} \tag{4.56}$$

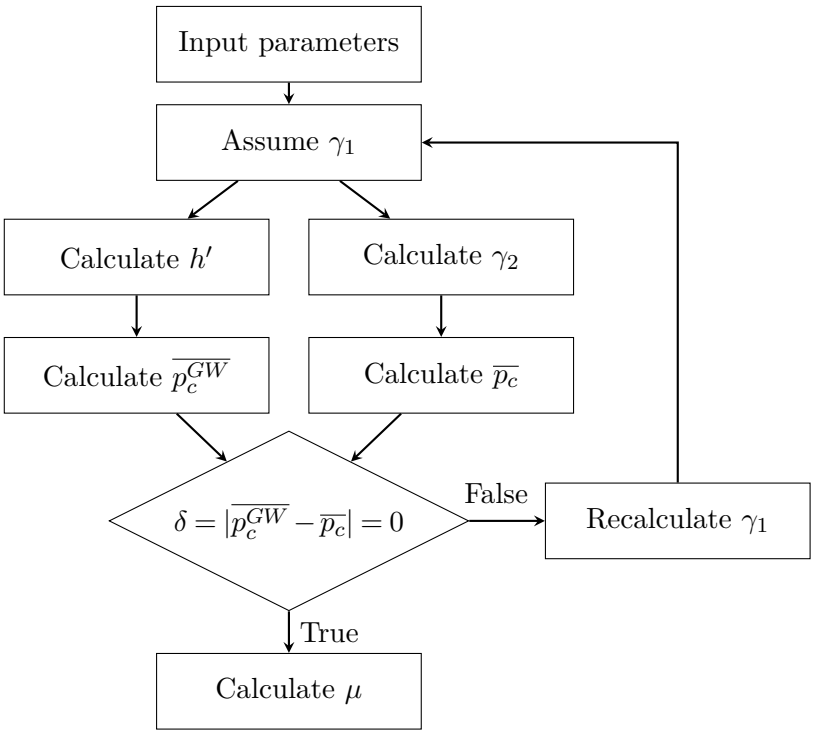


Figure 4.8: Flowchart of the numerical method with pressure convergence.

Another possible convergence criterion is, instead of converging the pressures, converging the asperity force in equations (4.34) and (4.49), resolving the system of equations (4.57) and following the Figure 4.9. This convergence criterion will be the one used in this dissertation because it is not based in fitted parameters.

$$\begin{cases} F_c = \dfrac{2}{3} n A_c E' \beta^{\frac{1}{2}} \sigma_s^{\frac{3}{2}} \mathrm{F}_{\frac{3}{2}} \left(\dfrac{h - d_d}{\sigma_s} \right) \\ \\ \dfrac{1}{\gamma_1} + \dfrac{1}{\gamma_2} = 1 \end{cases} \tag{4.57}$$

When the convergence is achieved, the coefficient of friction can be calculated.

$$\mu = \frac{\mu_c F_c + F_{f,H}}{F_n} \tag{4.58}$$

For example, assuming the lubricant follows the Eyring model:

$$\mu = \frac{\mu_c F_c + \tau_0 \operatorname{arcsinh}\left(\frac{\eta v_g}{h_c \tau_0}\right) A_H}{F_n} \tag{4.59}$$

Where:

$$A_H = A_c - A \tag{4.60}$$

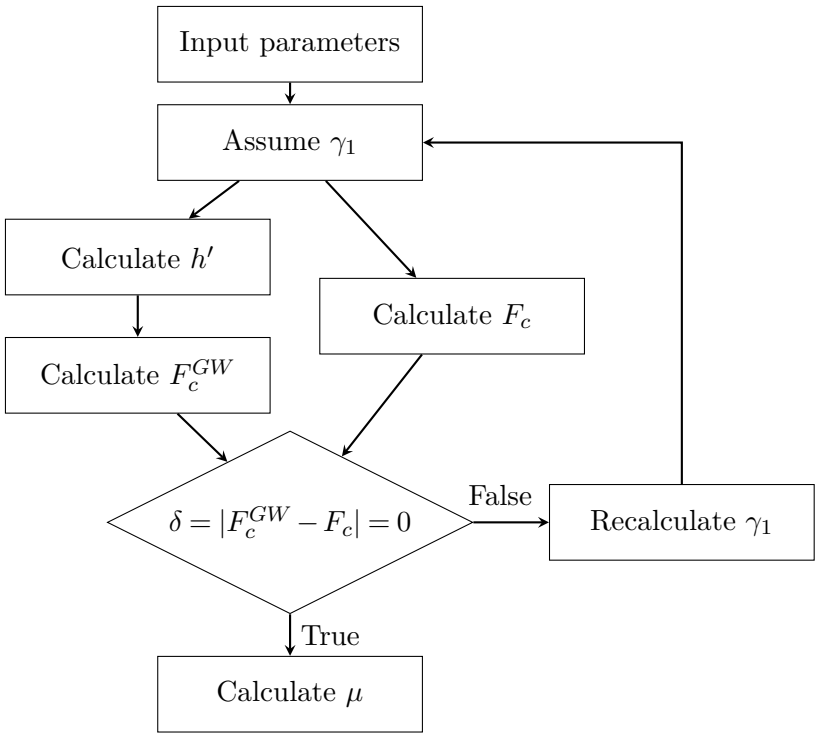


Figure 4.9: Flowchart of the numerical method with force convergence.

$$p_H = \frac{F_H}{A_H} \tag{4.61}$$

To plot the Stribeck curve, the friction is calculated for different speeds; therefore, it is important to ensure that the runtime is as short as possible. To decrease the runtime, the iterative code was vectorized, and only the speeds that didn't converge were used in a new iteration.

4.4.2 Convergence Algorithm

At the first iteration, a value for γ_1^k is selected and at the end of that iteration, a new value (γ_1^{k+1}) must be selected for the next iteration, but there are no previous value of γ_1 and δ to apply the equation (4.62), so it was defined that $\gamma_1^{k+1} = 0.9\gamma_1^k$. From the second iteration until the convergence, the value in the iteration $k+1$ of γ_1 is calculated using the gradient descent method.

$$\gamma_1^{k+1} = \gamma_1^k - \alpha_{\gamma_1} \operatorname{sgn}\left(\frac{\Delta\delta}{\Delta\gamma_1}\right) \tag{4.62}$$

Where α_{γ_1} is the step length, sgn is the sign function defined by the equation (4.63), and $\frac{\Delta\delta}{\Delta\gamma_1}$ is an approximation of the derivative of δ.

$$\operatorname{sgn}\left(\frac{\Delta\delta}{\Delta\gamma_1}\right) = \begin{cases} +1 & \text{if } \frac{\Delta\delta}{\Delta\gamma_1} > 0 \\ 0 & \text{if } \frac{\Delta\delta}{\Delta\gamma_1} = 0 \\ -1 & \text{if } \frac{\Delta\delta}{\Delta\gamma_1} < 0 \end{cases} \tag{4.63}$$

The minimal value of a module function is 0, so optimization techniques can be used to minimize δ, ensuring the convergence of the model. Using δ and γ_1 from the previous iteration (δ^{k-1} and γ_1^{k-1}), the gradient of δ is obtained with equation (4.64). Since this optimization problem has only one optimization variable, the gradient is used only to obtain the direction that minimizes δ, and the step length is fully controlled by α_{γ_1}.

$$\frac{\Delta\delta}{\Delta\gamma_1} = \frac{\delta^k - \delta^{k-1}}{\gamma_1^k - \gamma_1^{k-1}} \tag{4.64}$$

From an abstract point of view, it is not strictly necessary to use only the sign of the gradient, but this way, a better control of the step length is obtained. From equation (4.36), the value of γ_1 must be greater than 1, a low value of γ_1 will turn γ_2 negative, implying a negative asperity force, which is impossible. So the optimization problem has one restriction:

$$\gamma_1 > 1 \tag{4.65}$$

To ensure this restriction, if γ_1 calculated with equation (4.62) is lower than 1, the algorithm falls back one iteration and α_{γ_1} is reduced, trying that in the next iteration the lower step gives $\gamma_1^{k+1} > 1$.

During the optimization process, an iteration can increase the difference of pressure, which indicates that the optimal value of γ_1 is between the value of γ_1^{k-1} and γ_1^k. Therefore, the solution is, once again, to reduce α_{γ_1}.

This dynamic approach for α_{γ_1} reduces the iterations needed for convergence because it allows bigger steps in the first iterations and reduces them along the iterations.

4.4.3 Model verification

Another important step is the verification of the model, for which, according to the literature, it is used a Gaussian distribution, so a more exhaustive verification using this distribution is made [19]. The reference values used by Faraon [19] are in Table 4.3, only missing the viscosity-pressure index. To overcome that problem, the parameter is calculated with equation (4.12), obtaining a value of $z = 0.680$. The values were extracted from figures in Faraon's thesis, what may result in a slight residual difference.

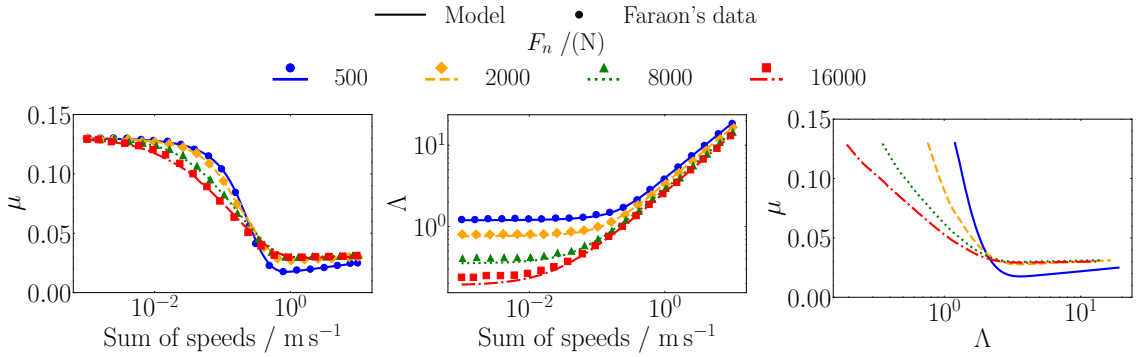
Comparing the two stop criteria, the force criteria achieved better results with R^2=0.997, while the pressure criteria, R^2=0.989, so the force criteria will be used and, because of the high value of R^2, it can be said that the model verification was successfully done . In the

Table 4.3: Reference values for the model verification [19].

Property	Value
n / $(1/m^2)$	1×10^{11}
β / m	1×10^{-5}
σ_s / m	5×10^{-8}
b / m	0.01
E' / GPa	231
R_x / m	0.02
η_0 / (Pa s)	0.0202
α / Pa^{-1}	2×10^{-8}
τ_0 / MPa	2.5
μ_c	0.13
F_n / N	500

verification of this model, it was considered that $U_1 \neq 0$ and $U_2 = 0$, resulting in a pure sliding scenario, and that μ_c is constant and independent of the SRR.

In Figures 4.10 to 4.13, the cases presented by Faraon [19] are replicated to verify the model, and where the Λ is calculated using the ratio between h_c and σ_s that is the standard deviation of the summit heights. In Figure 4.10, the influence of the normal force is studied and, as expected, as F_n increases, the transition between the mixed lubrication and Elastohydrodynamic lubrication is delayed because a higher force reduces the film thickness and consequently, the specific film thickness reduces.



(a) Influence of the normal force in the Stribeck curves.

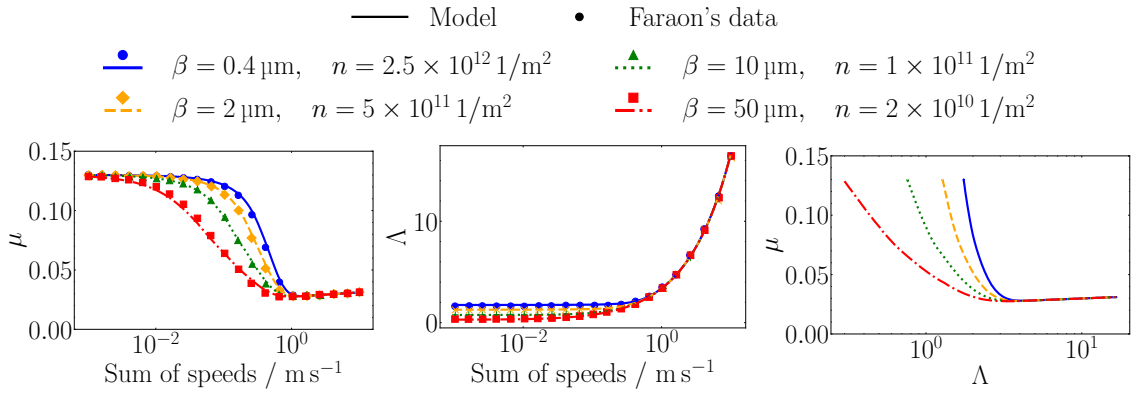
(b) Influence of the normal force in the specific film thickness.

(c) Friction vs. Specific film thickness.

Figure 4.10: Influence of the normal force.

In the work of Greenwood and Tripp [45] is stated that $n\beta\sigma_s$ be between 0.03 and 0.05, so assuming a value of 0.05, Faraon changed two of the three roughness parameters. Figure 4.11 shows the decrease of the speed needed for the transition from mixed lubrication and elastohydrodynamic. A lesser number of asperities, but higher asperity radius, creates a smoother contact, resulting in a smaller coefficient of friction in the boundary and mixed

lubrication regimes and an early transition between lubrication regimes.



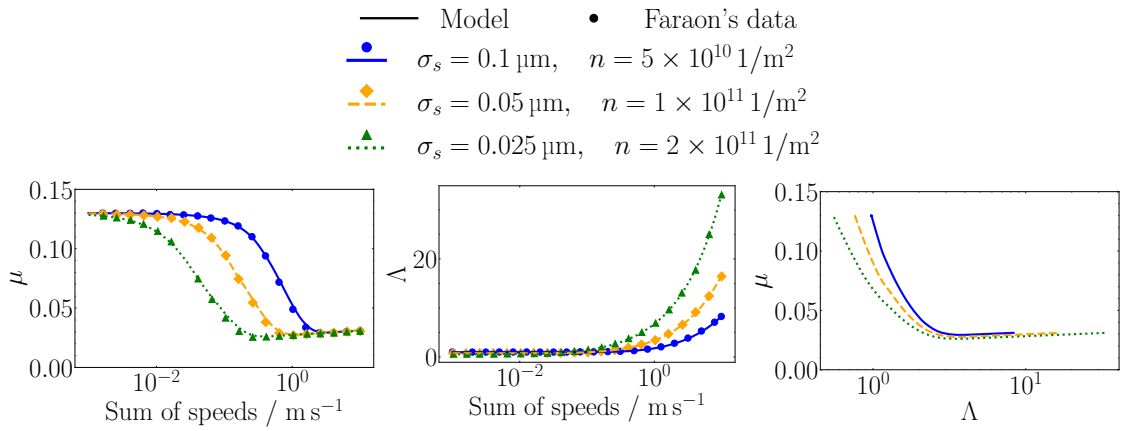
(a) Influence of β and n in the Sribeck curves.

(b) Influence of the β and n in the specific film thickness.

(c) Friction vs. Specific film thickness.

Figure 4.11: Influence of β and n (F_n= 2000 N and $\sigma_s = 0.05\,\mu m$).

Figure 4.12 shows clearly the influence of σ_s in the Stribeck curves, the standard deviation is directly connected to the specific film thickness, highly influencing the transition to full film. Lower values of σ_s increase Λ for a given film thickness, which promotes an early transition between the lubrication regimes.



(a) Influence of σ_s and n in the Sribeck's curve.

(b) Influence of σ_s and n in the specific film thickness.

(c) Friction vs. Specific film thickness.

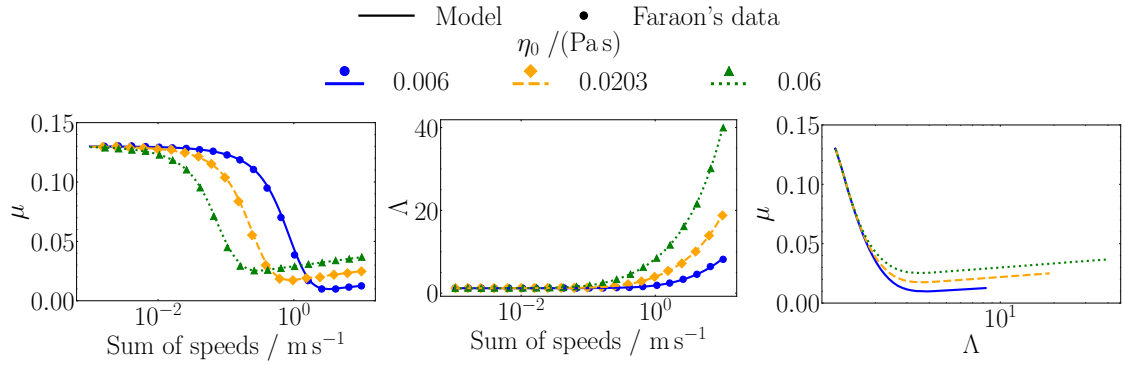
Figure 4.12: Influence of σ_s and n (F_n= 2000 N and $\beta = 10\,\mu m$).

In Figure 4.13, the inlet viscosity is varied, where, for the same speed, a higher η_0 creates a higher film thickness, reducing the needed speed to achieve full film conditions. The viscosity also highly influences the friction at the elastohydrodynamic regime and the minimal friction, where both of them are increased with η_0.

At last, in Figure 4.14, it is interesting to vary the sliding rate (V_s) (equation (4.66)). As expected, when $V_s = 0$, the difference in speeds is 0 and consequently the friction at elastohydodynamic regime approaches 0 and, since the sum of speeds are kept constant,

varying V_s is changing the difference between both speeds, meaning that no differences in the transition between the lubrication regimes are shows and the unique difference is the value of the coefficient of friction in the elastohydrodynamic regime.

$$V_s = \frac{|U_1 - U_2|}{(U_1 + U_2)} \tag{4.66}$$

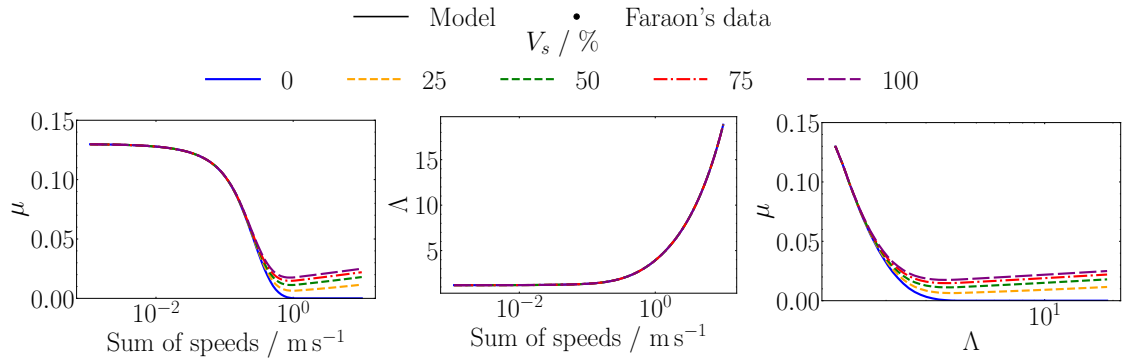


(a) Influence of η_0 in the Sribeck's curve.

(b) Influence of the η_0 in the specific film thickness.

(c) Friction vs. Specific film thickness.

Figure 4.13: Influence of η_0 (F_n= 500 N).



(a) Influence of the V_s in the Sribeck's curve.

(b) Influence of V_s in the specific film thickness.

(c) Friction vs. Specific film thickness.

Figure 4.14: Influence of the sliding rate in the Sribeck's curve.

4.4.4 Faraon's asperity contact model

Expanding Greenwood and Tripp's model, Faraon proposes a contact model between two rough surfaces where the radius and density of the asperities of each surface are different, that is, when $\beta_1 \neq \beta_2$ and $n_1 \neq n_2$ [19]. From equations (4.67) to (4.70), the asperities force, area, number of the asperities in contact, and pressure, respectively.

$$F_c = \frac{8}{15}\pi n_1 n_2 E' \beta^{1/2}(\beta_1 + \beta_2)\sigma_s^{5/2} A_c F_{5/2}\left(\frac{h - d_d}{\sigma_s}\right) \tag{4.67}$$

$$A_r = \pi^2 n_1 n_2 \beta (\beta_1 + \beta_2) \sigma_s^2 A_c F_2 \left(\frac{h - d_d}{\sigma_s} \right) \tag{4.68}$$

$$N = 4\pi n_1 n_2 \sigma_s (\beta_1 + \beta_2) A_c F_1 \left(\frac{h - d_d}{\sigma_s} \right) \tag{4.69}$$

$$p_c = \frac{8}{15\pi} E' \sqrt{\frac{\sigma_s}{\beta}} \frac{F_{5/2}\left(\frac{h-d_d}{\sigma_s} \right)}{F_2 \left(\frac{h-d_d}{\sigma_s} \right)} \tag{4.70}$$

Using the values of Table 4.3, changing the roughness to the ones stated in Table 4.4, a comparison between the Faraon's asperity contact model and the results obtained by Faraon is made in Figure 4.15, and good results are achieved [19].

Table 4.4: Roughness parameters for cases A and B - Values from [19].

Parameter	**Case A**	**Case B**
$\boldsymbol{\sigma_{s1}}$ / **µm**	0.49	0.31
$\boldsymbol{\beta_1}$ / **µm**	2.6	8.8
$\boldsymbol{n_1}$ / $(\mathbf{1/m^2})$	13×10^9	12.5×10^9
$\boldsymbol{\sigma_{s2}}$ / **µm**	0.064	0.4
$\boldsymbol{\beta_2}$ / **µm**	40.8	9
$\boldsymbol{n_2}$ / $(\mathbf{1/m^2})$	13×10^9	10×10^9

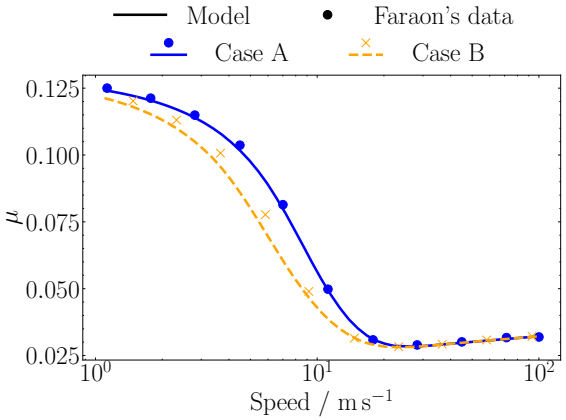


Figure 4.15: Faraon's new model comparison.

4.4.5 Thermal model

To account for the heat generated in contact, the film thickness must be corrected due to the inlet shear heating effect (equation (4.73)) [43]. The thermal reduction parameter (ϕ_T) is calculated with equation (4.71) where L is the thermal loading parameter (equation (4.72)), SSR is the slide-to-roll ratio, and V_e is the entrainment speed.

$$\phi_T = \frac{1 - 13.2 \cdot \frac{p_h}{E'} \cdot L^{0.42}}{1 + 0.213 \cdot (1 + 2.23 \cdot SSR^{0.83}) \cdot L^{0.64}} \tag{4.71}$$

$$L = \frac{\eta_0 \beta V_e^2}{k} \tag{4.72}$$

$$h_{cT} = \phi_T h_c \tag{4.73}$$

Under the work of Arana et al. [43], the oil temperature in the contact is calculated with the equations (4.74) to (4.81). The heat flux generated in the contact ($\dot{q}$) heats both the surfaces and due to the material properties of the bodies 1 and 2, the flux that goes to each surface may not be equal. The heat partitioning parameter (ϵ) describes the heat flux that goes to surface 1, where M_i and B_i are the steady state and transient thermal resistances of body i, respectively. The equations (4.76) and (4.77) are adapted from the work of Paouris et al. [58], using A_H of a linear contact, as explained by Olver [65].

$$\dot{q} = \mu \cdot p_m \cdot v_g \tag{4.74}$$

$$\epsilon = \frac{1.06 B_2 + M_2}{1.06 \cdot (B_1 + B_2) + M_1 + M_2} \tag{4.75}$$

$$B_i = \frac{1}{A_H k_{s,i}} \sqrt{\frac{\chi_i a}{U_i}} \tag{4.76}$$

$$M_i = \frac{h_{cT}}{2 A_H k} \tag{4.77}$$

$$\chi_i = \frac{k_{s,i}}{\rho_i c_{p_i}} \tag{4.78}$$

Where p_m is the average hertzian pressure, $k_{s,i}$ is the thermal conductivity of the body i, ρ_i is the density of the body i, and c_{p_i} is the specific heat capacity of the body i. The values of $k_{s,i}$, ρ_i and c_{p_i} for steel are given by Table 4.5.

Table 4.5: Steel properties [66].

Property	**Value**
$\boldsymbol{k_{s,i}}$ **/ (W m^{-1} K^{-1})**	45
$\boldsymbol{\rho_i}$ **/ (kg/m^3)**	7800
$\boldsymbol{c_{p_i}}$ **/ (J kg^{-1} K^{-1})**	460

With the heat flux and partition calculated the average flash temperature rise ($\Delta\overline{T}_{Fl}$) and the average oil film increase ($\Delta\overline{T}_{oil}$), which gives the average film temperature ($\overline{T}_f$) in equation (4.81). Since the gears will be in a controlled bath, T_0 is constant.

$$\Delta\overline{T}_{Fl} = \frac{1.06 \cdot \epsilon \cdot \dot{q}}{k_{s,1}} \cdot \left(\frac{\chi_1 \cdot a}{U_1} \right)^{1/2} \tag{4.79}$$

$$\Delta\overline{T}_{oil} = \frac{h_{cT} \cdot \dot{q}}{8k} \tag{4.80}$$

$$\overline{T}_f = T_0 + \Delta\overline{T}_{Fl} + \Delta\overline{T}_{oil} \tag{4.81}$$

As the oil temperature changes, the lubricant properties will change, resulting in an iterative process (Figure 4.16). In the first iterations, $\overline{T_f}$ is considered equal to T_0 and the stop criteria is a difference between $\overline{T_f}$ of two iterations being less than 1%.

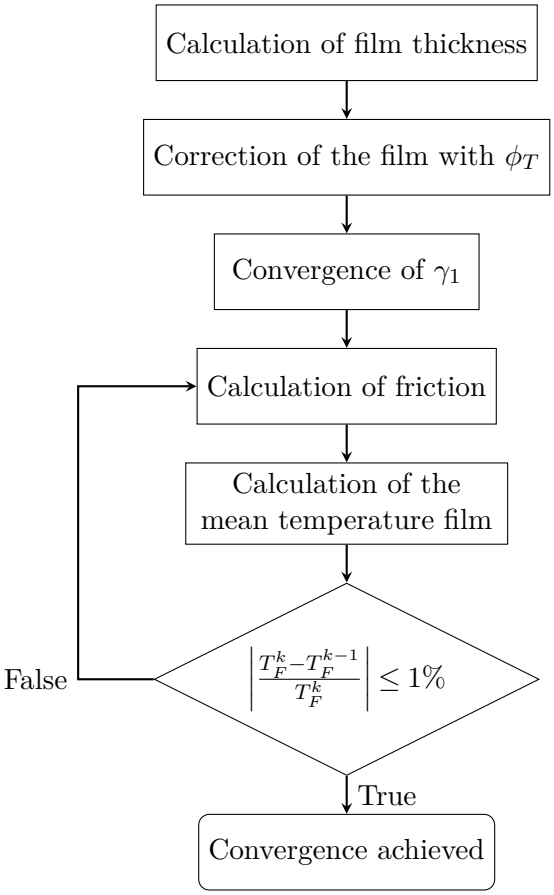


Figure 4.16: Flowchart of the thermal model iterative process.

4.4.6 Application of the model to gears

To implement in the friction model for spur gears is crucial to understand their geometry and kinematics. A gear is defined as an object that is rotationally symmetric and has a tooth system [17]. The most used tooth profile is the involute profile because that profile is easily manufactured, keeps the gear ratio constant even when the center distance is changed and has a constant pressure angle, ensuring a smooth gear meshing [18]. Because of that, the geometry of those gears will be discussed and implemented in the model.

When two gears mesh, the smaller is called a pinion and the bigger is called a wheel. In the following equations, the subscript 1 correspond to the quantities related with the pinion and the subscript 2 related to the wheel.

During the functioning of the gears, the number of pairs of teeth in contact changes. So it is interesting to calculate the contact ratio (ϵ_α) of the pair of gears (equation (4.82) [18]). ϵ_α is the ratio between the length of line of contact and the transverse base pitch

(p_{bt}) and represents the mean number of pairs of teeth in contact.

$$\epsilon_\alpha = \frac{\overline{AE}}{p_{bt}} = \frac{\sqrt{r_{a1}^2 - r_{b1}^2} + \sqrt{r_{a2}^2 - r_{b2}^2} - a_w \sin(\alpha_{wt})}{\pi m_n \cos \alpha_t} \tag{4.82}$$

In the meshing process, the line formed by all the contact points is called the path of contact (Figure 4.17), that is tangent to the base circle of the pinion and wheel in the points T_1 and T_2, respectively and passes through the point C, known as pitch point. The engagement of the gears starts at point A, where the line of action intercepts the active tip diameter of the driven gear (Figure 4.17). At E, the engagement ends in the interception of the path of contact and the active tip diameter of the driving gear (Figure 4.18). If the contact ratio is greater than 1, it means that, on average, more than or pair of teeth are in contact at the same time. This results in moments where the load is transmitted by only one contact, so appears more two relevant points (B and D).

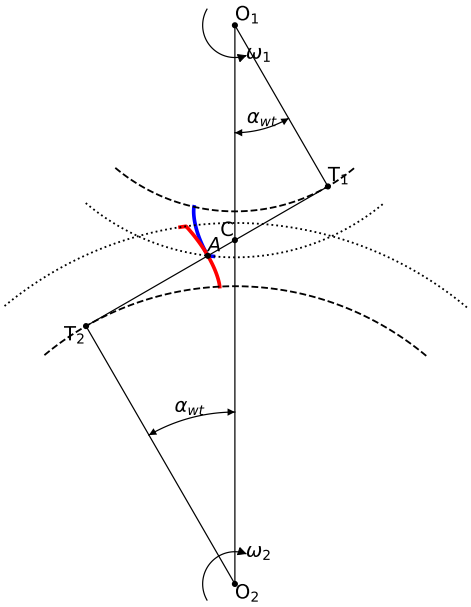


Figure 4.17: Start of gear tooth meshing – Adapted from [18].

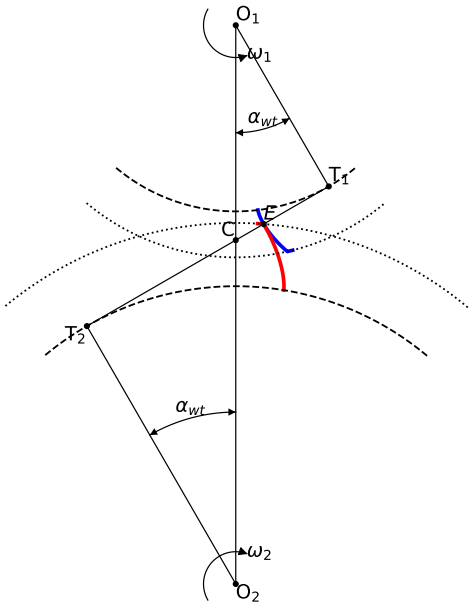


Figure 4.18: End of gear tooth meshing – Adapted from [18].

At the start of the engagement between A and B, there is still contact between the previous pair of teeth, so there are two pairs of teeth in contact. At point B, the previous teeth pair disengage and, until point D, the load is supported by only one pair of teeth. From D until E, the next pair of teeth engage and the load is supported again by two pairs of teeth.

Therefore, this will lead to a load carried by a tooth that varies along the path of contact. Figure 4.19 shows the variation of the normal force along the path of contact, where points A, B, D and E are represented. As expected, the load is increased between

the points B and D at correspond to the zone in the path of contact that only one pair of teeth are in contact.

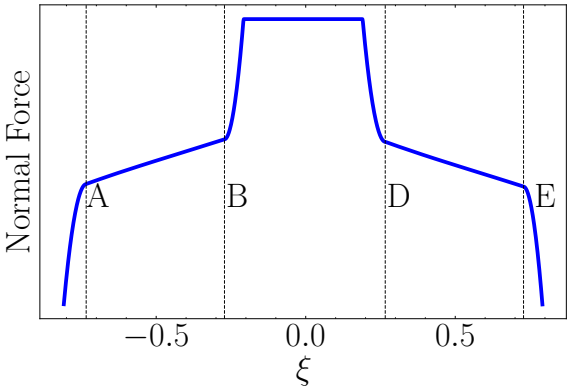


Figure 4.19: Example of the normal force along the path of contact [67].

In the path of contact, since the distance of Y to the center of each gear and speed direction change, yet in the direction normal to the contact, the speed must be equal to ensure the continuity of transmission of the load [18]. In the tangential direction of the contact, the speeds vary, which creates sliding in the surface with a sliding speed (v_g) given by equation (4.83), where ω_1 is the pinion angular speed and ρ_{Yi} is the contact radius (equation (4.84)).

$$v_g = \pm\omega_1 \left(\frac{\rho_{Y2}}{u} - \rho_{Y1} \right) \tag{4.83}$$

Where:

$$\rho_{Yi} = \overline{T_i Y} = \frac{z_i}{|z_i|} r_b \tan \alpha_{Yt} \tag{4.84}$$

Figure 4.20 shows the variation of the rolling speeds, sliding speed, and entrainement speed where it is important to note that the sliding speed is 0 in the pitch point that results in a coefficient of friction of 0 in that point, and Figure 4.21 shows the variation of the contact radius of the pinion and the wheel.

Incorporating those changes along the path of contact in the model it is possible to calculate the coefficient of friction. In order to increase the computational efficiency of the model, a first iteration is done, solving the numerical problem at the points A, C, E, and the midpoints between them. With this first iteration cycle the γ_1 for those points is obtained and used as initial guess for the remaining points closer to them along the path of contact, which means that, in the final iteration cycle, the points that are closer to the point A will have the initial value of γ_1. This approach of having different initial values of γ_1 for different conditions in the contact decreases the time needed to run the model.

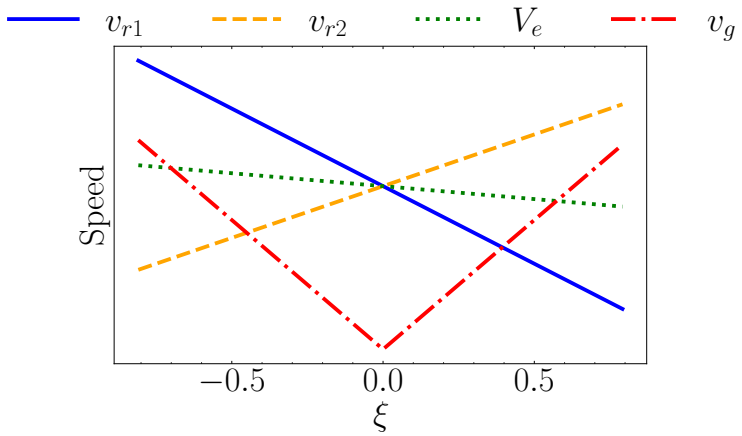


Figure 4.20: Example of the speeds along the path of contact [67].

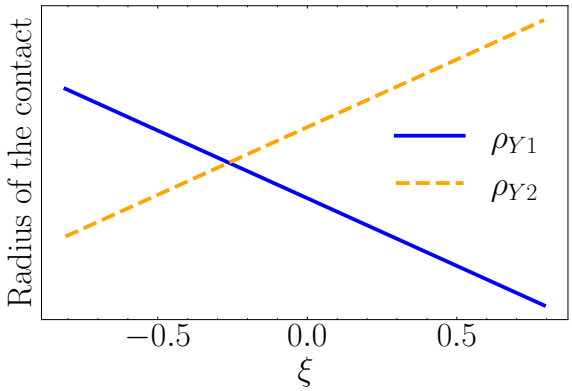


Figure 4.21: Example of the contact radius along the path of contact [67].

Chapter 5

Comparison with experimental results

5.1 Ball-on-disk - Gaussian Distribution

To validate the model, some traction and Stribeck curves for the oil PAO ISO VG 150 were used, with the use of an EHD2 machine (Figure 3.11) that performs ball-on-disk tests, measuring the friction between both surfaces. Since the contact generated during this test is circular, it is a special case of elliptical contact, so the equations in the Appendix A are applicable. During this comparison, the ball is considered body 1 and the disk is body 2.

The traction and Stribeck curves were measured following the procedure described in the work of Fernandes et al. [68], where several ball-on-disc tests were performed using the EHD2 machine (Figure 3.11) under controlled temperature. The ball and disc were made from chrome steel with the properties in Table 5.1. The oil properties are in Table 5.2 where K, b and c are the parameters for the Vogel's law, s and t are the parameters for the Gold's equation, Z and S_0 are the Roelands' exponents obtained in the work of Brandão et al. [66], and k and c_p are the thermal conductivity and heat capacity [58].

Table 5.1: Relevant properties for the EHD2 test machine [68].

Property	**Ball**	**Disk**
R_x / mm	9.525	∞
R_y / mm	9.525	∞
E / GPa	210	210
ν	0.29	0.29

During the traction curve measurements, the ball is pressed against the disk with a given entrainment speed, load, and operating temperatures, where the slide to roll ratio was increased from 1% to 100% and then from 100% to 1% while the entrainment speed was kept constant. The entrainment speeds, loads, and operating temperatures of the

Table 5.2: Lubricant parameters

Parameter	**Value**
ρ / (kg/m^3)	854
K	0.02468
b	1667.31
c	151.09
s	7.382
t	0.1335
Z	0.467
S_0	1.09
k / (W m^{-1} K^{-1})	0.18
c_p / (J kg^{-1} K^{-1})	2090

available traction curves are the combination of the properties in Table 5.3, all of them done to 3 different disks with the properties in Table 5.4.

Table 5.3: Properties of the traction curves

Test	$\boldsymbol{T_0}$ **/ °C**	$\boldsymbol{F_n}$ **/ N**	$\boldsymbol{U_1}$ **/ m s^{-1}**	**Disk**
Traction	40, 70, 100	20, 30, 50	0.5, 1, 2	1, 2, 3

Table 5.4: Roughness parameters of the disk used in the ball-on-disk tests

Parameter	**Ball**	**Disk 1**	**Disk 2**	**Disk 3**
$\boldsymbol{R_a}$ **/ µm**	0.0273	0.0079	0.188	0.558
$\boldsymbol{R_q}$ **/ µm**	0.0438	0.0160	0.266	0.881

For the Stribeck curves, the ball was loaded against the disks with F_n =50 N and the rolling speed was changed between 0.01m s^{-1} and 3m s^{-1}. The Stribeck curves available are all the combinations of properties in Table 5.5, and the disk's properties are in Table 5.4.

For both tests, the surfaces were leveled and filtered in Vision64 with $\lambda_c = 0.25$ mm, and the calculation of the summit parameters follows the procedure described in Chapter 2.

The EHD2 has the main purpose of measuring the film thickness, but it can be used to measure the friction. During each test, for a given sliding speed, there are two scenarios: the scenario where $U_1 > U_2$ and the one where $U_1 < U_2$. That difference will lead to differences associated with the thermal characteristics of the contact, and to solve this, the machine averages the result of both scenarios. With this in mind, in the developed model, both scenarios are considered, and the average values are compared with the experimental results, where the thinner lines correspond to the simulations with $U_1 > U_2$ and $U_1 < U_2$, and the thicker one to the average result.

Table 5.5: Properties of the Stribeck curves

Test	T_0 / °C	F_n / N	SRR / %	Disk
Stribeck	40, 70, 100	50	3, 50	1
			20	2
			20, 50	3

The comparison between the experimental and model results will be divided into two parts. The first analysis will use the traction curves, mainly the ones from disk 1 (with the lowest roughness), to verify the coefficient of friction under full film EHL conditions. Then, the Stribeck curves will be used to adjust the boundary regime, and the results obtained in the mixed lubrication regime will be analyzed. In Subsections 5.1.1 and 5.1.2, the roughness parameter follows Faraon's summits definition, but the inaccurate results in the mixed lubrication regime lead us to find an alternative method to select the summits. Therefore, in Subsections 5.1.4 and 5.1.3, the procedure is repeated using that alternative method for the calculation of the roughness parameters, in which the matrix size is related with the average asperity radius in each direction, resulting in a increase of the model´s precision.

5.1.1 Traction curves - Faraon's summits definition

During this part, the main focus is to validate the elastohydrodynamic part of the model, that is, the rheological behaviour of the lubricant and the relevant properties associated with that behaviour, using tests with the lower surface roughness, disk 1 in this case.

From the work of Ma et al. [69], a process to calculate the value of τ_L is stated, and as a consequence, the rheological behaviour follows the equation (4.32). Ma et al. state that only the traction curves completely within the elastohydrodynamic regime and without great thermal influence should be used in the estimation of τ_L (Figure 5.1) and that τ_L is defined by equation (5.1), where μ_{max} is the maximum coefficient of friction in the traction curve and p_m is the Hertzian mean pressure.

$$\tau_L = \mu_{max} p_m \tag{5.1}$$

Respecting that definition, the valid tests are shown in Figure 5.2, obtaining the values in Table 5.6. While Ma et al. considered that only the mean pressure influences τ_L, other authors, like Brandão et al. [66], state that the temperature also influences τ_L, so it was also considered a linear dependence between τ_L and temperature. Resulting in the following definition for τ_L:

$$\tau_L = a p_m + b T_0 + c \tag{5.2}$$

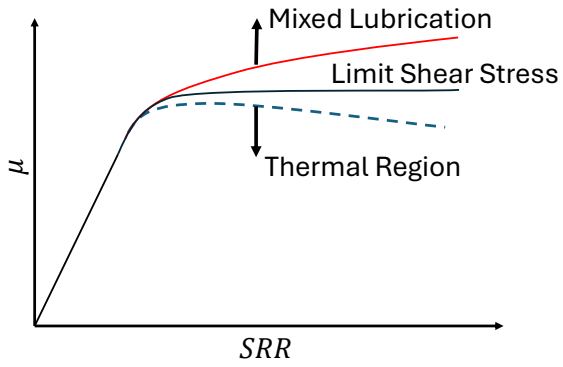


Figure 5.1: Selection criteria of the curves for the estimation of τ_L - Adapted from [69].

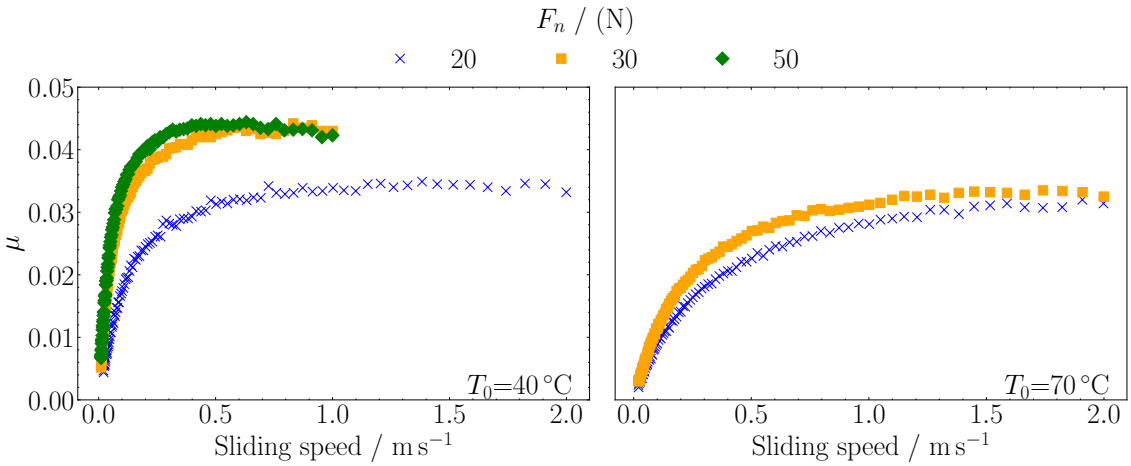


Figure 5.2: Traction curves used for estimating τ_L.

Table 5.6: Values for the estimation of τ_L.

Test	T_0/ °C	F_n / N	V_e / m s^{-1}	p_m / MPa	μ_{max}	τ_L / MPa
1	40.83	20	2	543.2	0.0349	18.96
2	72.02	20	2	543.2	0.0320	17.38
3	40.33	30	1	623.6	0.0442	27.56
4	71.67	30	2	623.6	0.0337	21.02
5	40.29	50	1	739.2	0.0446	32.97

With the values in Table 5.6, and using the method of least squares, the parameters a, b and c were obtained (Table 5.7) and compared with the experimental values in Table 5.8 and Figure 5.3.

Applying the selection method used by Faraon [19], the roughness parameters used in the model are stated in Table 5.9. In those tests are done with new surfaces, where there is no running-in process, so it is possible to consider that the surfaces follow a Gaussian

distribution (example in Figure 5.4a). Yet the Gaussian distribution does not model the ball surface as well (Figure 5.4b) and, since the ball has low roughness, especially compared with to disk 2 and 3 when the roughness is more relevant, its non-Gaussian behavior should not have great influence on the results. In other words, both surfaces will be considered Gaussian at first, and in Section 5.3 other distributions will be studied.

Table 5.7: Adjusted parameters for PAO ISO VG 150.

Parameter	**Value**
a	0.0659
b	-0.1239
c	-10.329

Table 5.8: Comparison between the experimental and adjusted values of τ_L.

Test	$\boldsymbol{\tau_L^{\text{Exp}}}$ **/ MPa**	$\boldsymbol{\tau_L}$ **/ MPa**	**Error**
1	18.96	20.39	7.6%
2	17.38	16.52	4.9%
3	27.56	25.75	6.6%
4	21.02	21.86	4.0%
5	32.97	33.37	1.2%

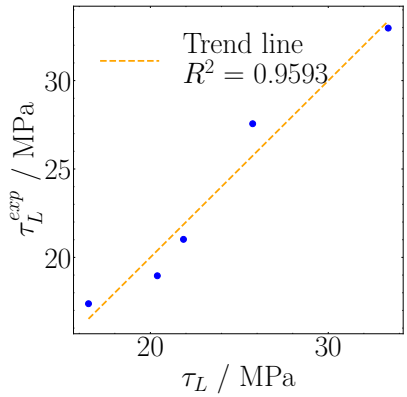
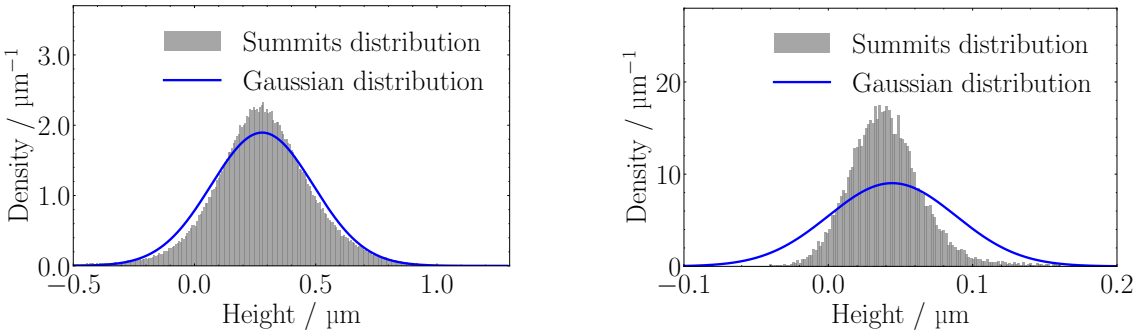


Figure 5.3: Comparison between the experimental and adjusted values of τ_L.

Table 5.9: Roughness parameters obtained with Faraon's summit selection method.

Parameter	**Ball**	**Disk 1**	**Disk 2**	**Disk 3**
$\boldsymbol{\sigma_s}$ **/ µm**	0.0442	0.009283	0.211	0.524
$\boldsymbol{\beta}$ **/ µm**	24.53	70.35	3.85	4.19
$\boldsymbol{n}$ **/ (1/m²)**	6.12×10^{10}	6.79×10^{10}	5.55×10^{10}	4.47×10^{10}



(a) Disk 2. (b) Ball.

Figure 5.4: Summit heights distribution.

With all the parameters defined, the traction curves of the lubricant with the lower roughness were modelled and compared to the experimental results in Figure 5.5. In a general way, the model presents good results, while it is important to note that a slightly worse result is obtained at $T_0 = 70\,°\mathrm{C}$ caused by the fact that the experimental curves do not reach a completely flat plateau which complicates the estimation of τ_L and that the assumption of a linear dependence of τ_L with the temperature isn't the most accurate, so in the future, a better method to calculate τ_L must be studied and implemented.

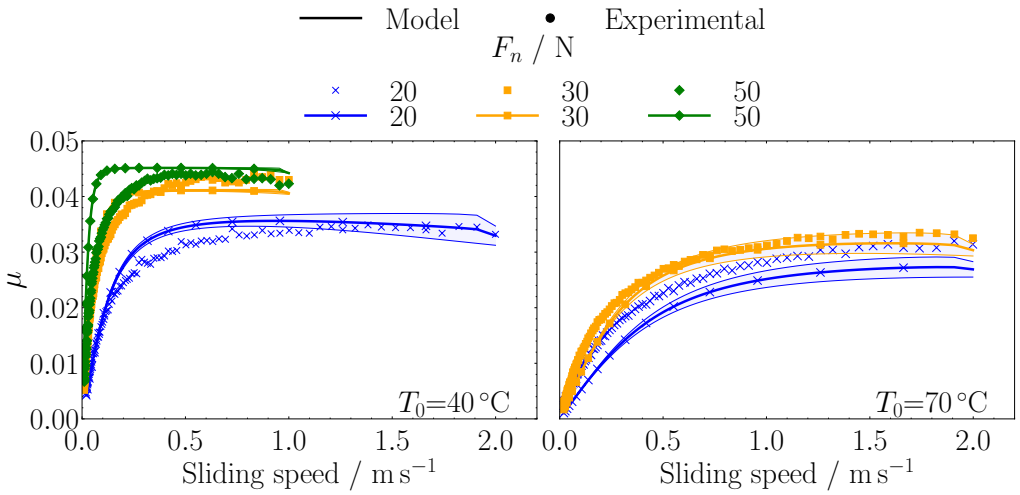
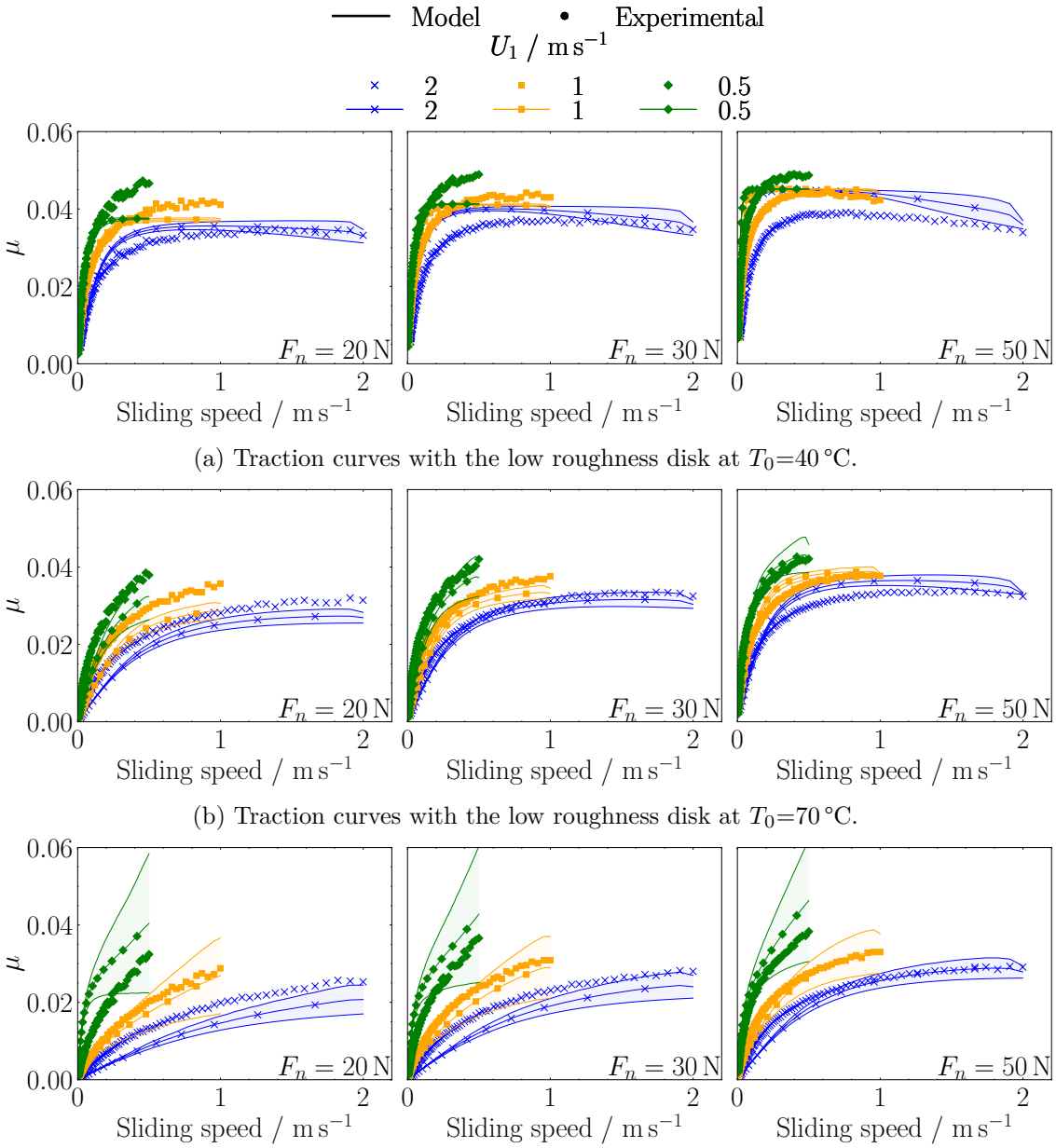


Figure 5.5: Traction curves used to estimate τ_L.

For lower sliding speeds, that is, lower SRR, the results have a deviation from the experimental values. Still, that problem is not relevant because the zone with higher friction in the gear contact has higher SRR.

Now that the elastohydrodynamic regime part of the model is validated, the traction curves with the surface of disk 1 (Table 5.9) are compared with the ones created by the model in the Figures 5.6a, 5.6b, and 5.6c. Those results increase the trust in the model behaviour in the EHL regime. In Figure 5.6c, an example is shown with $T_0 = 100\,°\mathrm{C}$, where it shows worse results caused mainly by the fact that in the estimation of τ_L, none



(a) Traction curves with the low roughness disk at T_0=40 °C.

(b) Traction curves with the low roughness disk at T_0=70 °C.

(c) Traction curves with the disk 1 at T_0=100 °C.

Figure 5.6: Traction curves with disk 1.

of the samples respect the criteria stated by Ma et al. [69], therefore the value of τ_L was an extrapolation from the the values obtained to $T_0 = 40\,°\text{C}$ and $T_0 = 70\,°\text{C}$.

The remaining tests with the other surfaces that have higher roughness were performed, but the obtained results are completely different from the experimental ones, meaning that the roughness parameters considered are not correct and must be study how to obtain the roughness parameters to obtain better results. Section 5.1.2 will discuss how to overcome this problem.

5.1.2 Stribeck curves - Faraon's summit definition

With a similar approach, the Stribeck curves for the disk 2 (Table 5.9) are computed and compared with the experimental results in Figure 5.7. For those results, the values of $\mu_{c,max}$ and S_{ep} were considered 0.13 and 0.10, respectively.

Now that both the boundary regime and elastohydrodynamic regime are fully defined, the mixed lubricated regime must be analysed. It is shown that both transitions between lubrication regimes are delayed, which means that a higher speed is needed to achieve mixed lubrication and the full film. The delay is explained by an overestimation of the roughness parameters used in the model, which evidences the necessity of an alternative method to obtain those parameters.

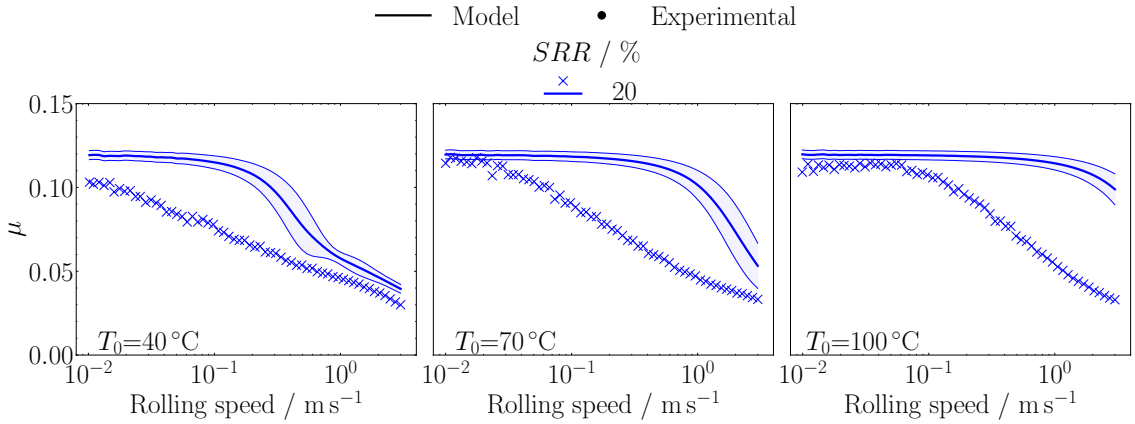


Figure 5.7: Stribeck Curves of disk 2 using Faraon's summit definition (F_n=50 N).

As it was explained in Section 2.3, the definition of a summit used by Faraon is not restrictive enough, allowing the selection of several points as summits, but in reality, those points can belong to the same summit that must only be counted as one. To better explain this, a profile from disk 2 was extracted, and Faraon's summit definition was used. Figure 5.8 shows a profile extracted from the surface used in the test, with length similar to the contact width ($2a$), where the summits are marked with red dots. From those summits, it is evident that some of them are too close to each other or, in reality, belong to the same contacting summit, like the ones highlighted in that figure. The selection of all of those points as a summit has the main consequence of artificially inflating n, which, when introduced in the model, generates a rougher contact than it is.

5.1.3 Stribeck curves - Proposed summit definition

Backed by the fact that the used definition do not fit experimental data, because some selected summits are bellow the mean line where is not expected to contact the other surface. To be sure of that, in the future a deterministic model should be used to verify that. A new strategy has been developed where the size of the matrix from which the

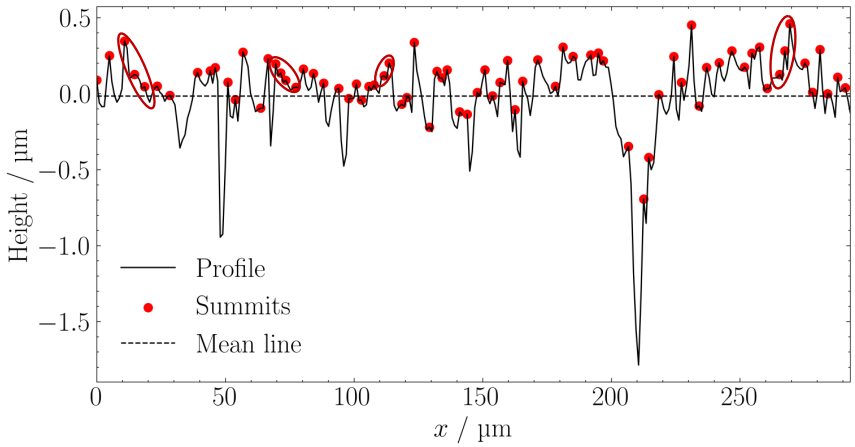


Figure 5.8: Profile showing the summit selection with a (3x3) matrix along Hertz contact width ($2a$).

central point must be the local maxima for it to be classified as a summit is increased. In conjunction with the measurement's resolution, this matrix size is related to an area in which a point must be the highest for it to be a summit. Since the right matrix size is unknown, a parametric study has been done to determine the influence of the matrix size on the Stribeck curves of the medium roughness sample.

With those parameters, each selection method was compared with the experimental results of disk 2's test at $T_0 = 40\,°\text{C}$ in Figure 5.9. While Table 5.10 clearly shows the influence of the matrix size on the roughness parameters, especially in the case of the asperities density, Figure 5.9 points out that the matrix size that best adjusts to the experimental results is the (7x7) matrix. Yet, it is important to analyze the selected summits of each matrix to make sure that the summit definition is accurate and if the matrix size is correct when used in other test samples.

Table 5.10: Roughness parameters to different matrix sizes.

Matrix	**Ball**			**Disk 2**		
size	$\boldsymbol{\sigma_s}$ **/ µm**	$\boldsymbol{\beta}$ **/ µm**	$\boldsymbol{n}$ **/ (1/m²)**	$\boldsymbol{\sigma_s}$ **/ µm**	$\boldsymbol{\beta}$ **/ µm**	$\boldsymbol{n}$ **/ (1/m²)**
(3x3)	0.0442	24.53	6.12×10^{10}	0.211	3.85	5.55×10^{10}
(5x5)	0.0496	20.4	3.14×10^{10}	0.186	2.93	2.35×10^{10}
(7x7)	0.0551	18.37	1.79×10^{10}	0.169	2.44	1.13×10^{10}
(9x9)	0.0646	16.66	1.10×10^{10}	0.159	2.15	5.94×10^{9}
(11x11)	0.0721	15.21	7.26×10^{9}	0.151	1.97	3.39×10^{9}

Using the same profile used in Figure 5.8, the selected summits for the matrix sizes of (5x5), (7x7) and (9x9) are represented in Figures 5.10 to 5.12, where in the Figure 5.10 it appear to still occur a over-selection of the summits and in Figure 5.12, it appears that some summits are not selected, so to compromise, it was selected the matrix size of (7x7) to obtain the summit parameters.

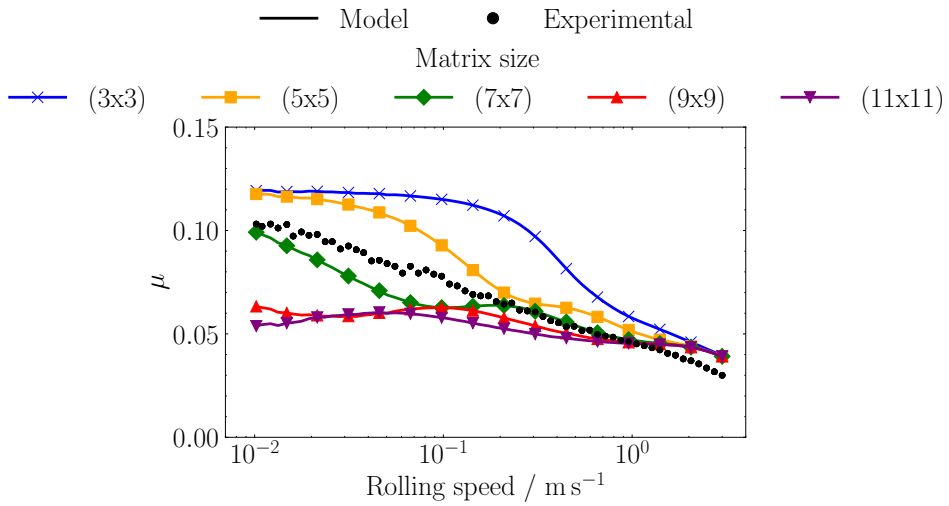


Figure 5.9: Stribeck curves with different matrix sizes for T_0=40 °C and F_n=50 N.

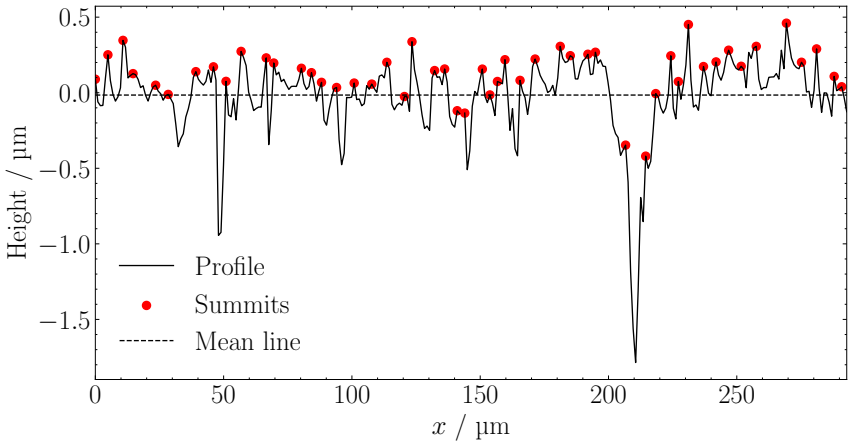


Figure 5.10: Profile showing the summit selection with matrix size of (5x5).

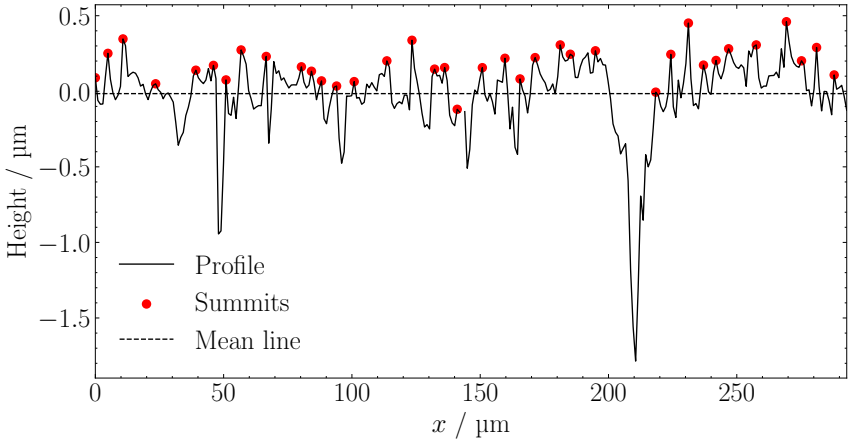


Figure 5.11: Profile showing the summit selection with matrix size of (7x7).

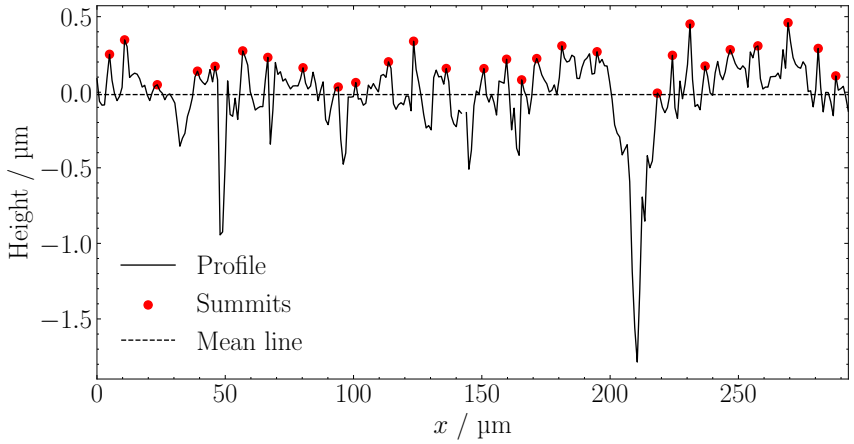


Figure 5.12: Profile showing the summit selection with matrix size of (9x9).

To further validate the selected size, other Stribeck curves are compared with the experimental results in Figures 5.13, 5.14 and 5.15, with the summit's parameters of all the surfaces using a matrix size (7x7) in the Table 5.11. Those figures show that the model presents overall good results, validating the model, but it also shows the importance of the summit's criteria selection, and that further work must be developed to better understand the asperity contact and define the relevant properties.

Table 5.11: Roughness parameters using a (7x7) matrix.

Parameter	**Ball**	**Disk 1**	**Disk 2**	**Disk 3**
$\boldsymbol{\sigma_s}$ **/ µm**	0.0551	0.0075	0.169	0.349
$\boldsymbol{\beta}$ **/ µm**	18.37	53.04	2.44	3.62
$\boldsymbol{n}$ **/ (1/m²)**	1.79×10^{10}	1.85×10^{10}	1.13×10^{10}	6.81×10^{9}

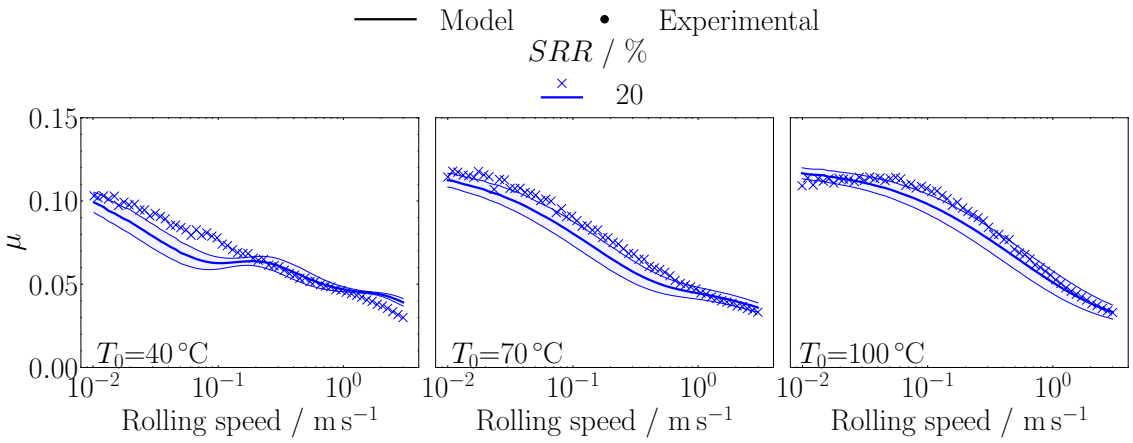


Figure 5.13: Stribeck Curves of the disk 2.

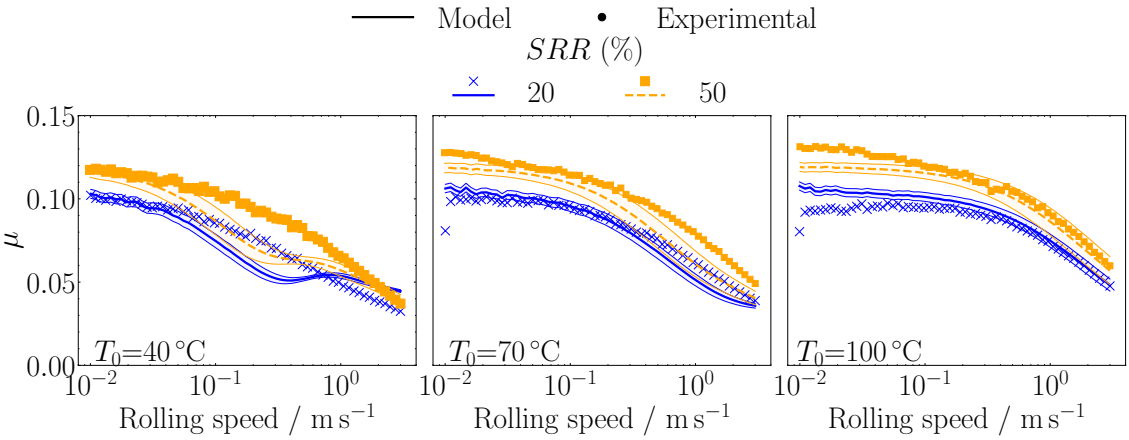


Figure 5.14: Stribeck Curves of the disk 3.

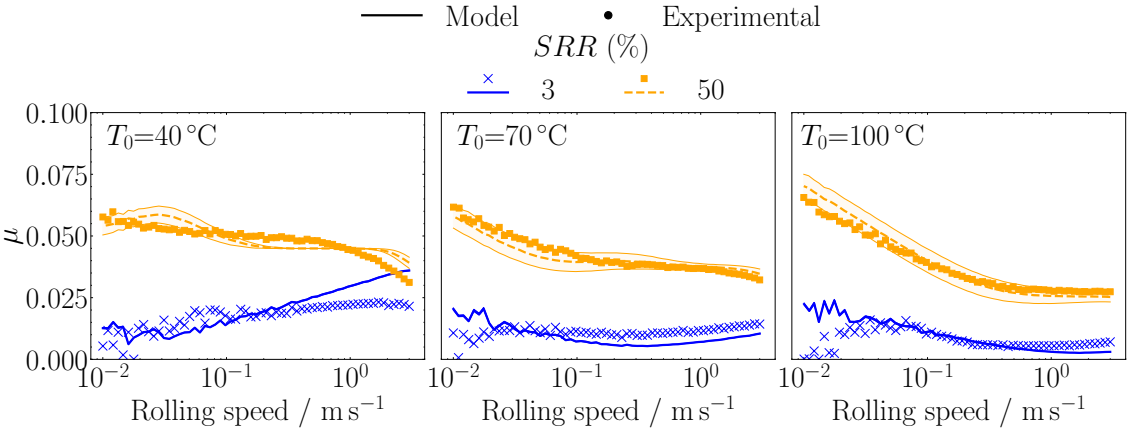


Figure 5.15: Stribeck Curves of the disk 1.

Furthermore, it is shown that the friction coefficient is highly dependent on the roughness parameters, so a simple parametric study, using the medium roughness surface at $T_0 = 40\,°\mathrm{C}$, was conducted by changing the roughness parameters σ_s, β and n by $\pm 10\%$, and $\pm 20\%$ in Figures 5.16, 5.17 and 5.18, respectively. As expected, increasing the roughness parameters leads to higher friction for a given rolling speed. Still, it is important to note that all the curves converge once the full film is reached.

While doing the selection of the matrix size with an empirical approach it was noticed that in disk 2, the (7x7) matrix size, with a $\Delta x = \Delta y \approx 1\mu\mathrm{m}$, corresponds to a 7 by 7 µm area, and the mean radius of the asperities in each direction ($\overline{\beta_x}$ and $\overline{\beta_y}$) are 2.66 µm, 2.59 µm. This leads to the idea of selecting the matrix size in order that the dimension of the matrix in each direction is twice the mean asperity radius in each direction (equations (5.3) and (5.4)). Where n_x and n_y are the matrix size in the x and y direction, respectively.

$$n_x \geq \frac{2\overline{\beta_x}}{\Delta x} \tag{5.3}$$

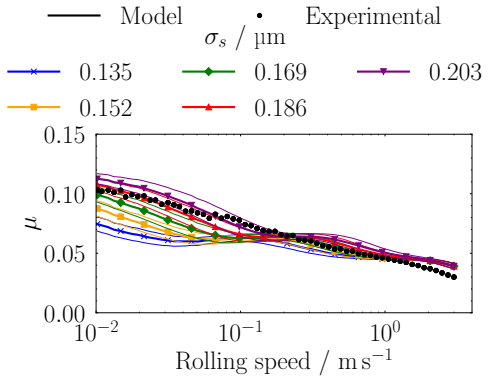


Figure 5.16: Influence of the summits standard deviation on the Stribeck curves.

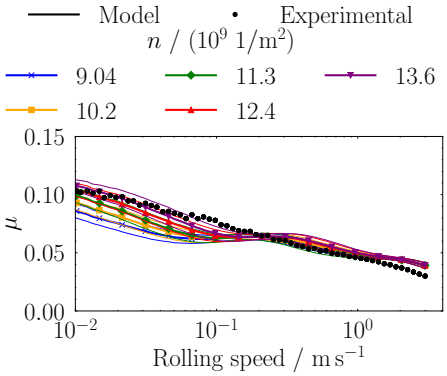


Figure 5.17: Influence of the summit density on the Stribeck curves.

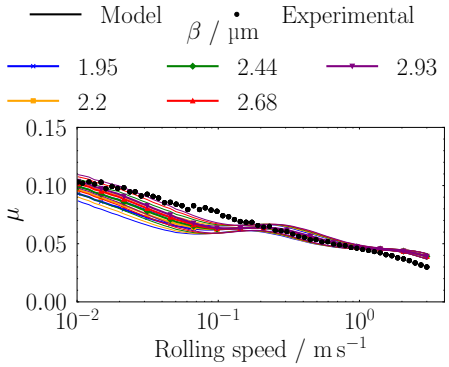


Figure 5.18: Influence of the asperities radius on the Stribeck curves.

$$n_y \geq \frac{2\overline{\beta_y}}{\Delta y} \tag{5.4}$$

Since the distance between summits resultant from this process is, in average, greater the asperity diameter, it is reduced the possibility of selecting the same summit more than once. To verify this the disks 2 and 3 will be studied, while the lower roughness of the remaining disk is very small it is almost in the elastohydrodynamic regime, so it is not so interesting to use it to study the roughness parameters. Since the roughness of the ball is much smaller than disks, its matrix size will be same than the disk. Table 5.12 shows

Table 5.12: Parameters to select the matrix size.

Parameter	**Disk 2**	**Disk 3**
$\overline{\beta_x}$ **/ µm**	2.66	3.73
$\overline{\beta_y}$ **/ µm**	2.59	3.69
$\overline{\beta_x}/\overline{\beta_y}$	1.03	1.01
Matrix size	(7x7)	(9x9)

the selection of the matrix size to the considered surfaces, and Table 5.13, and 5.14 the roughness parameters that result from that matrix size.

With those parameters the Stribeck curves in Figures 5.19 and 5.20 are obtained and a slight improvement is seen. Due to the accuracy of this selection criteria, it will be used in the comparison of the model with the experimental results of the gear tests.

Table 5.13: Roughness parameters for the disk 2's test.

Parameter	**Ball**	**Disk 2**
$\boldsymbol{\sigma_s}$ **/ µm**	0.0551	0.169
$\boldsymbol{\beta}$ **/ µm**	18.37	2.44
$\boldsymbol{n}$ **/ (1/m²)**	1.79×10^{10}	1.13×10^{10}

Table 5.14: Roughness parameters for the disk 3's test.

Parameter	**Ball**	**Disk 3**
$\boldsymbol{\sigma_s}$ **/ µm**	0.0646	0.309
$\boldsymbol{\beta}$ **/ µm**	16.66	3.43
$\boldsymbol{n}$ **/ (1/m²)**	1.10×10^{10}	3.29×10^{9}

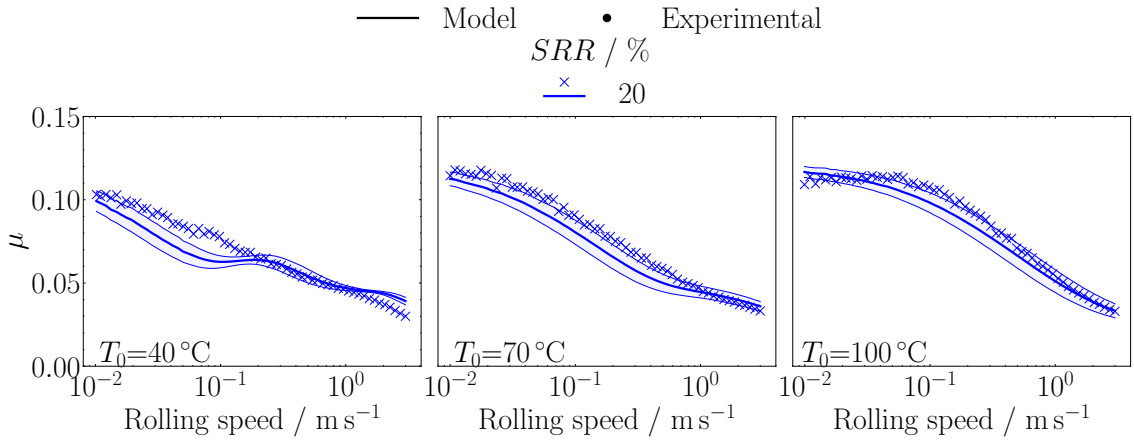


Figure 5.19: Stribeck Curves of the disk 2.

5.1.4 Traction curves - Proposed summit definition

To end up with this comparison, the traction curves are again done with the new procedure to identify the summits. In the disk 1's traction curves, since the specific film thickness (Λ) is high for both procedures, there are no relevant changes in the traction curves (example in Figure 5.21). In opposition, in the remaining disks, this procedure increases the accuracy of the model, yet the results of disk 3, the disk with the higher roughness, still have some divergences from the experimental results.

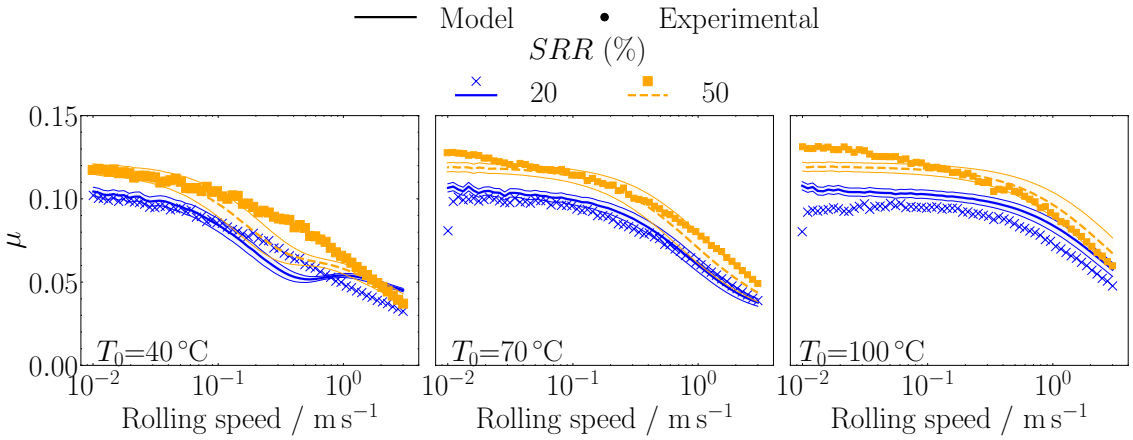


Figure 5.20: Stribeck Curves of the disk 3.

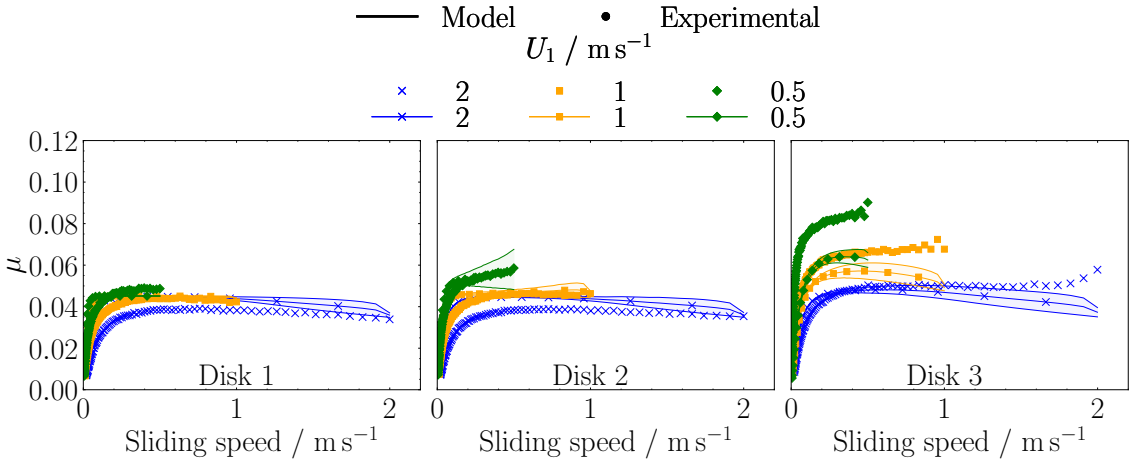


Figure 5.21: Traction curves at T_0=40 °C and F_n=50 N of each disk.

5.2 Gears - Gaussian Distribution

The work of Fernandes et al. [1] studied the influence of the running-in conditions in the running-in process and how it influences the steady-state coefficient of friction in gears. This comparison is divided into two parts, the first associated with the running-in and the second part, where the power loss is studied. The test procedure described by Fernandes et al. [1] is represented in Figure 5.22 and the surfaces used were measured by João Pais [70].

The gears in study have the properties stated in Table 5.15, and the lubricant is the PAO ISO VG 150 already used in the ball-on-disk tests (Table 5.2). In this comparison, there are several profiles available and the pinion's surface of the gear sets G1, G2, and G3 before and after running-in, so the main focus will be given to those gear sets.

In the running-in stage, the gear set is mounted in a FZG test rig (Figure 3.13) and the running-in process is done in the conditions of the Table 5.16, and it lasts 8 hours,

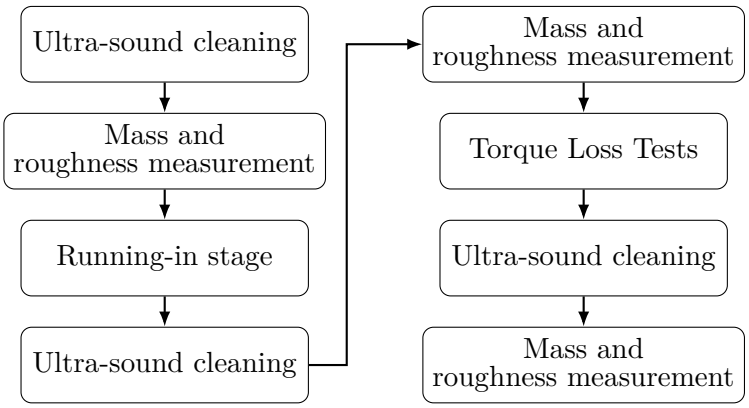


Figure 5.22: Experimental procedure to the gears' test [1].

corresponding to 144000 cycles of the pinion. This lower speed generates a very thin film ($\Lambda < 0.1$), promoting the wear of the surface. Within the Torque loss test, the gear set is under different load stages (K5, K7, and K9) and different speeds following the flowchart in Figure 5.23 at T_0=80 °C.

Table 5.15: Properties of the gears - Adapted from [1].

Parameter	**Pinion**	**Wheel**
z	16	24
m_n / mm	4.5	
a_w / mm	91.5	
α_n / °	20	
x	0.1817	0.1715
d_a / mm	82.64	118.54
ϵ_α	1.44	
Material	20MnCr5	
Treatment	Case hardened	

Table 5.16: Running-in conditions - Adapted from [1].

Gear set	**Load stage**	**Pinion Torque / N m**	T_0 / °C	**Wheel speed / rpm**
G1	K9	215.6	80	200
G2	K11	319.2	80	200
G3	K6	98.8	90	200
G4	K9	215.6	90	200
G5	K11	319.2	80	200

To compare the model to the results obtained by Fernandes et al [1], the mean coefficient of friction (μ_{mz}) is compared with the mean coefficient of friction calculated by the model.

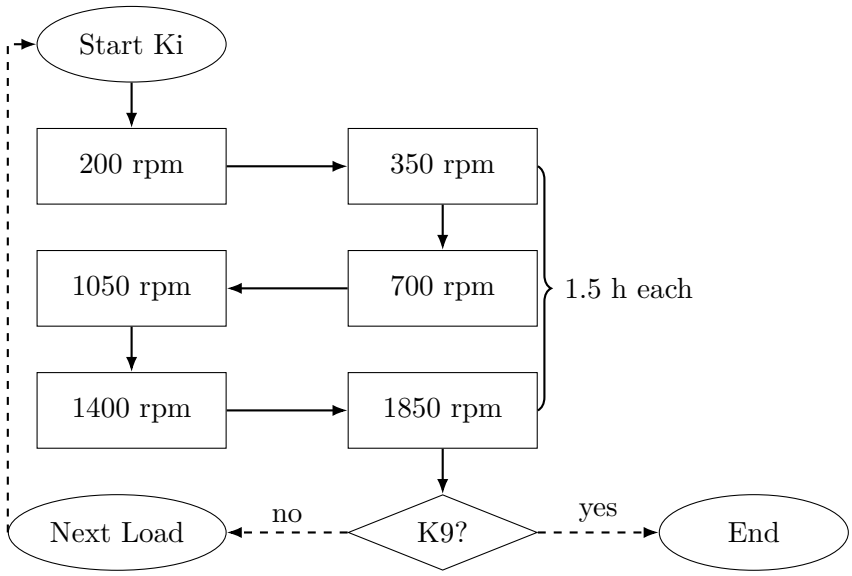


Figure 5.23: Flowchart of the torque loss test [1].

As it was explained in Chapter 2, to obtain the surface roughness, the form was removed with a 4th-order degree polynomial, and the waviness was removed using a Gaussian filter in Vision64. The cut-off length (λ_c) was selected using the concept of functional filtering, which defines λ_c as a value closer to the contact width. With the load stages of Table 5.16 the maximum contact width is around 0.5 mm in the load stage K11, but, in the beginning and ending of the path of the contact, the contact width is smaller (around 0.3 mm) because there are two pairs of teeth carrying the load. While it could be argued that a cut-off length of 0.25 mm is too small, most of the load stages will present lower loads and generate a contact width in the worst case similar to 0.25 mm. Besides that, the contact width is maximum in the central region of the path of contact where SRR tends to 0, which means that the friction component related to the asperities also tends to 0, meaning that the roughness in this region is less relevant.

Even though the use of surfaces is more accurate for calculating the roughness parameters two problems are encountered, the only measured surface is the pinion's surface and it measures an area of 3 mm by 7 mm in the tooth's tip, so the roughness properties of this zone are generalized to the entire tooth.

To overcome the problem of not having the surface of the wheels, the profiles were used to calculate the ratio between the roughness properties of the pinion and wheel, and use that ratio to adjust the properties when using the surfaces. Which means that if the difference between σ_s of the pinion and wheel is 10% when calculated from the profiles, it will be applied that difference to the parameters calculated with the pinion's surface, from where an estimation of the wheel parameters is done. So, in the future, more tests where both surfaces are measured are needed to ensure more accurate results.

Before a full comparison between the experimental results and the model, it is necessary

to select the value of $\mu_{c,max}$ and the matrix size to select the summits. Repeating the process done in the ball-on-disk the $\mu_{c,max}$ selected was 0.07, and the matrix size is selected based in the results of the Table 5.17.

Table 5.17: Values for the matrix size selection to each gear's sample

Gear Set		$\overline{\beta_x}$ / **µm**	$\overline{\beta_y}$ / **µm**	$\overline{\beta_x}/\overline{\beta_y}$	**Matrix Size**
G1	Before	11.17	2.34	4.77	23x7
	After	8.30	2.53	3.28	17x5
G2	Before	4.99	1.41	3.53	13x5
	After	6.60	2.36	2.80	15x5
G3	Before	7.59	2.08	3.65	17x5
	After	6.37	2.26	2.82	15x5

As expected, the asperities in a gear surface, are much larger in one direction than the other due to the finishing process applied to gears. This not only turn the selection matrix from a square matrix to a rectangular one, it also shows that the asperities are ellipsoids instead of being spherical as the model proposed.

Table 5.18 shows the difference between the properties of the pinion and wheel measured using the profiles, and looking up to those values, the gear samples before and after running-in present similar values. Table 5.19 shows the roughness parameters of the pinions and wheels, already taking into consideration the differences obtained from the profiles.

Table 5.18: Difference between the roughness properties of the pinion and wheel before and after the running-in

Gear set		$\boldsymbol{\sigma_s}$	$\boldsymbol{n}$	$\boldsymbol{\beta}$
G1	Before	−39.4%	5.8%	−3.9%
	After	−29.4%	1.8%	−4.2%
G2	Before	−18.7%	5.0%	−13.3%
	After	−31.7%	7.7%	7.0%
G3	Before	−18.3%	12.8%	−27.6%
	After	−34.1%	0.3%	15.7%

With all the properties defined, the mean coefficient of friction ($\overline{\mu}$) computed by the model, assuming a Gaussian distribution, is compared with the experimental values obtained by Fernandes et al. [1] in Table 5.20. Beside the reduction in accuracy of the model associated with the lack of the wheel surfaces to obtain theirs roughness parameters, some more comments must be made.

As discussed in Chapter 3, the coefficient of friction should reduce during the running in process, and that is seen in all the gear sets. While the results from G1 and G2 are

Table 5.19: Roughness parameters of the gears before and after running-in.

Gear Set		Pinion			Wheel		
		σ_s / µm	n / $(1/m^2)$	β / µm	σ_s / µm	n / $(1/m^2)$	β / µm
G1	Before	0.753	1.62×10^9	4.60	0.456	1.72×10^9	4.45
	After	0.421	4.12×10^9	4.11	0.297	4.19×10^9	3.94
G2	Before	0.630	9.60×10^9	2.36	0.517	10.1×10^9	2.07
	After	0.395	7.01×10^9	3.58	0.270	7.50×10^9	3.84
G3	Before	0.648	2.72×10^9	3.58	0.517	3.10×10^9	2.92
	After	0.426	4.72×10^9	3.39	0.281	4.75×10^9	3.90

close to the experimental, G3 has a larger error. However, it is important to note that the experimental values are obtained through indirect measurements, which may introduce some errors in the experimental values.

Table 5.20: Comparison between the coefficient of friction obtained in the model and experimentally.

Gear set	Model		Experimental		Difference	
	Before	After	Before	After	Before	After
G1	0.0528	0.0473	0.052	0.051	1.54%	−7.25%
G2	0.0604	0.0525	0.0594	0.0563	1.68%	−6.75%
G3	0.0593	0.0561	0.047	0.0399	26.17%	40.60%

Those results clearly shows the limitations of the model when the asperities are not spheres, but are in reality ellipsoids. While in the ball-on-disk test the ratio between the asperity radius in each direction is close to 1, meaning that they are almost spheres, in the gears, that number is closer to 3, even reaching a value of almost 5 in the gear set G1 before the running-in.

The difference between the model and the experimental results increased after the running-in, because before running-in, the surfaces have higher roughness being in the boundary lubrication regime, but, with the roughness reduction after the running-in, it is closer to the mixed lubrication regime where the limitations of the model are more evident.

So, to summarize it up, the accuracy of all the results are affected by uncertainty of the wheel parameters, and by the great ellipticity of the summits.

In Figure 5.24, the coefficient of friction along the path of contact of each gear set is compared (with a discretization of the path of contact in 200 points), and, as expected, after running-in, the coefficient of friction is reduced and the friction coefficient goes to 0 near the pitch point.

It is crucial to point out that in the extremes of the path of contact (beginning and end of the contact), the coefficient of friction has an increase that is caused by numerical

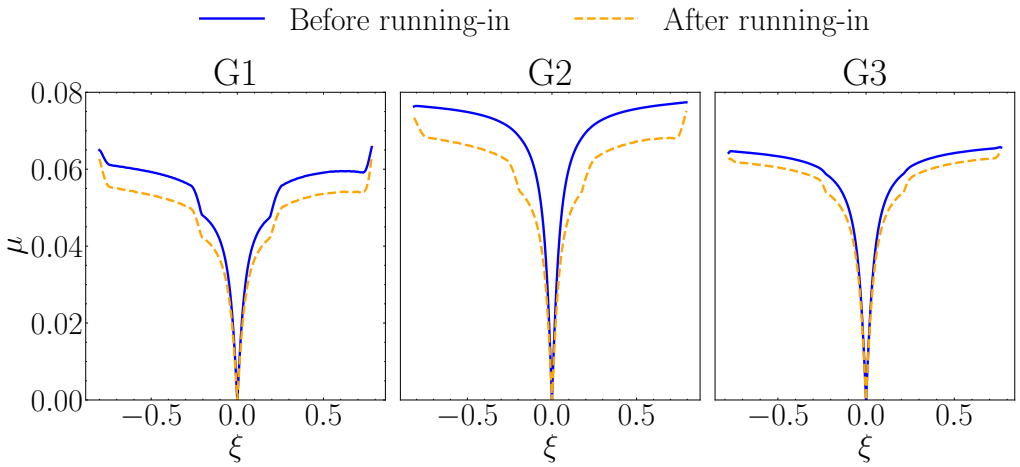


Figure 5.24: Coefficient of friction along the path of contact before and after the running-in process.

issues when F_n tends to lower values, μ tends to infinity. However, in literature [43], using numerical models, it is shown that in the contact borders the friction should decrease. This behavior can be implemented by not considering the elasticity of the tooth in the calculation of the contact force along the path of contact or artificially putting a minimum threshold of F_n to calculate the value of μ. Yet, to maintain the natural behavior of the model, it will not be changed.

After the running-in process, μ_{mz} was estimated for the load cases K5, K7 and K9 (70 N m, 132.5 N m and 215.5 N m, respectively) and for the wheel speed of 200 rpm, 350 rpm, 700 rpm, 1050 rpm and 1400 rpm. Figure 5.25 presents the comparison between the model and experimental results, where it is clear that the model does not predict the coefficient of friction accurately under certain conditions, mainly at lower loads. Two main factors contribute to this, one related to the implemented model and another related to the estimation of the roughness parameters.

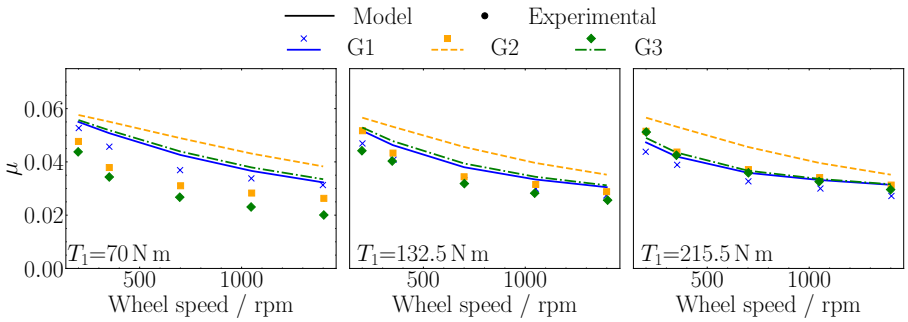


Figure 5.25: Influence of the wheel's speed on the mean coefficient of friction.

The coefficient of friction along the path of contact of the gear set G3 for T_1=70 N m and different wheel speed values is presented in Figure 5.26, where the speed increase leads to a decrease in the coefficient of friction.

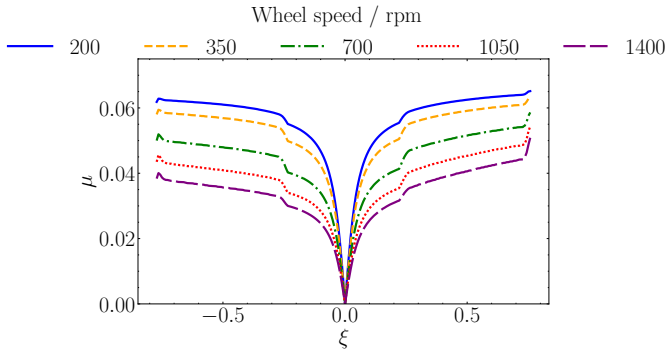


Figure 5.26: Influence of the wheel speed on the coefficient of friction along the path of contact.

The Greenwood and Williamson's contact model assumes that the asperities are spherical at the tip, while this assumption can be made in the ball-on-disk test, the manufacturing process of gears results in a surface with a highly accentuated transverse surface pattern. So the asperities should be ellipsoids or even cylinders, taking into account β_x and β_y independently instead of an equivalent asperity radius (β).

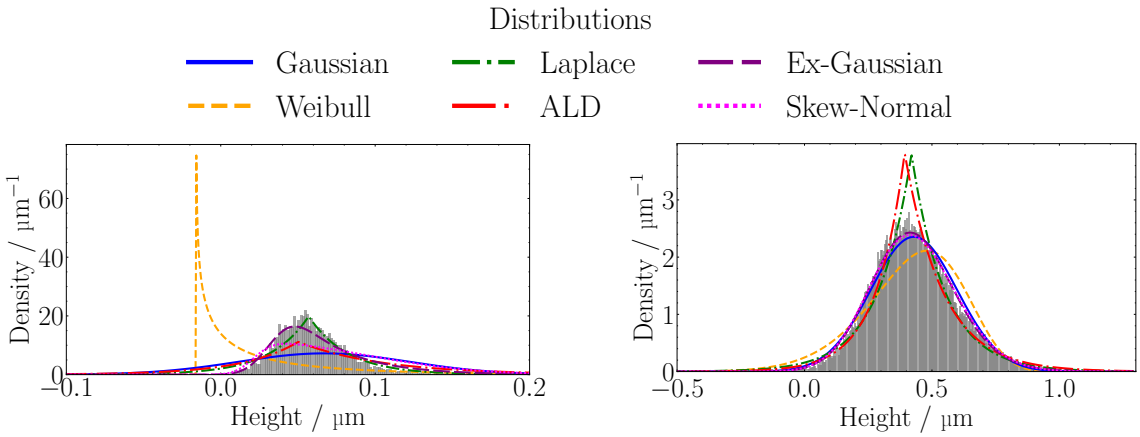
The model performance is highly dependent of the correct selection of the matrix size and, while it is proposed a criterion to select that value, a more in-depth study is need. It is also important to notice that during the torque loss test, so running-in process may still occur, resulting in a slight reduction in the roughness, because in the work of Fernandes et al. [1] the samples after the torque loss test present a reduction in the values of R_a, and R_q. However, there is no available surfaces after that test to be used in the model, so that slight reduction in roughness was not accounted.

5.3 Ball-on-disk - Non Gaussian distributions

Until now all it was always considered that the summits follow a Gaussian distribution, but that is not always true, especially in surfaces after running-in. With this in mind, the influence of other distributions is studied. But since it is assumed that the disks do not suffer running-in, different distributions should not have a great impact in the final results, so only one the disk 2 will be studied.

Figure 5.27 shows a comparison between the ball and disk 2 summit heights and the different distributions considered. While disk is well modeled with the Gaussian distribution, the ball is better modeled with other distributions, but due to its lower roughness, it will not have a great influence on the resultant Stribeck curves. To maintain the coherence, when the Stribeck curves are calculated, it is assumed that the same distribution is used for both surfaces.

The disk 2 (Figure 5.27b) is well modeled by the Gaussian distribution, yet distributions like the Ex-Gaussian and Skew-Normal distributions, increase the capacity to model the summit heights. Both Laplace and Asymmetrical Laplace distributions still



(a) Ball. (b) Disk 2.

Figure 5.27: Summit height distribution of ball and disk 2.

have problems in modeling the summits around the mean summit heights and the Weibull distribution reduces the accuracy when compared with the Gaussian.

The ball's surface (Figure 5.27a) has a low values of kurtosis, flattening the distribution, that makes the Gaussian and Weibull distributions to not adjust accurately to the summit heights distribution. While the Skew-Normal is more accurate than the Gaussian, the Ex-Gaussian is the one that better model the surface. Besides that, both Laplace still do not model the surface accurately and may be disregarded.

Therefore, since the Ex-Gaussian and Skew-Normal distributions are the non-Gaussian distributions that better model the summits, their parameters are in Table 5.21.

Table 5.21: Distributions parameters for Ball and Disks.

Distribution	**Parameter**	**Ball**	**Diks 2**
Ex-Gaussian	μ_E / 10^6	0.0336	0.343
	σ_E / 10^6	0.0124	0.146
	τ_E / 10^6	0.0333	0.0860
Skew-Normal	α_{SN}	7.309	1.173
	λ_{SN} / 10^6	-0.0213	0.300
	δ_{SN} / 10^6	0.0715	0.213

As previously stated, the Gaussian distribution is not ideal to model the ball's surface. However, the height of those summits is low when compared with disk 2, and after the convolution operator, the resultant surface is similar to the disk surface (Example in Figure 5.28).

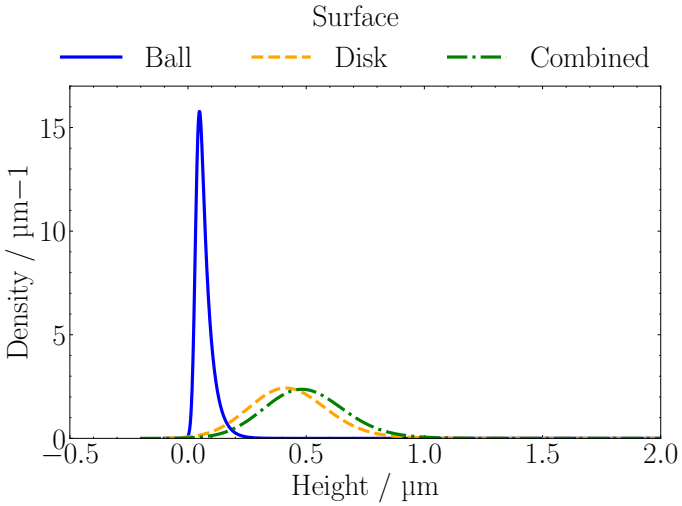


Figure 5.28: Example of the combined surface with a Ex-Gaussian distribution.

The impact of different distributions is more notable in the mixed lubrication regime, so the influence of different distributions will be studied using the Stribeck curve of disk 2. Figure 5.29 show the influence of the roughness distributions in the Stribeck curve, and, as expected, no significant changes are noticed. This happens because the Gaussian distribution already models the surfaces appropriately, and more significant changes are expected in samples where the Gaussian distributions are not a good approximation. This means that, if the disk 2 had a similar behaviour to the ball, where the Gaussian distribution is not accurate, the difference between the Gaussian curve and non-Gaussian curves will be bigger.

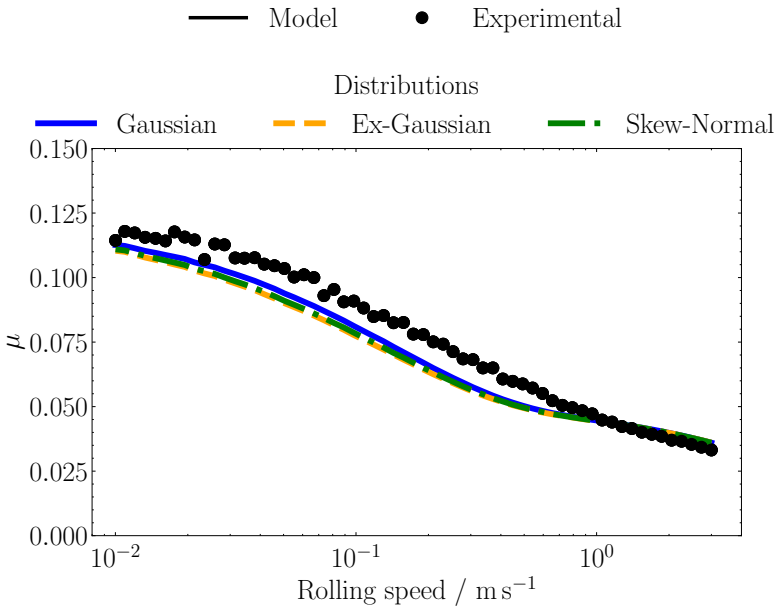
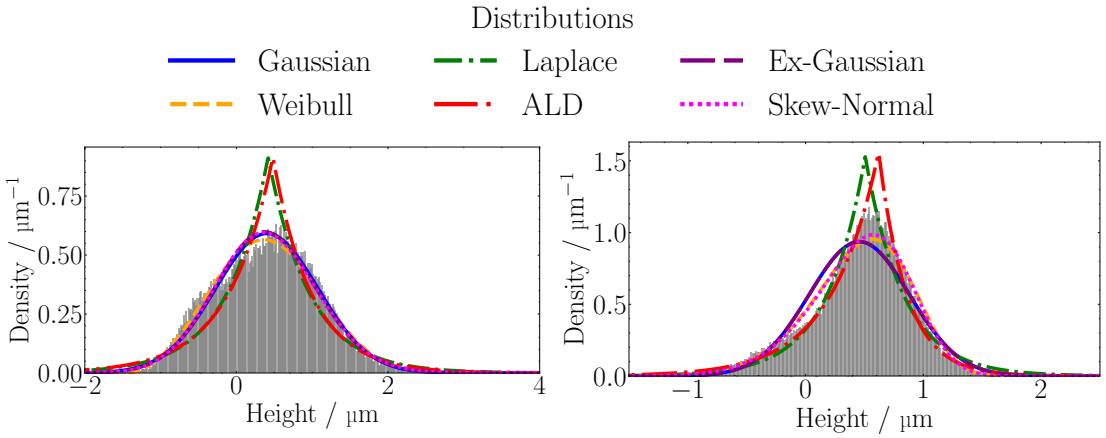


Figure 5.29: Stribeck curves of the medium roughness disk at T_0 =70 °C, F_n=50 N, and SRR=20%.

5.4 Linear contact - Non Gaussian distributions

The main advantage of using a non-Gaussian distribution is to increase the fit between the summit height distribution and the selected distribution of the post running-in surface. Therefore, in Figure 5.30, a comparison between the fit of all the studied distributions to the surface of the pinion G3 before and after the running-in is done, from where the distributions that better fit the surfaces are selected. Similar to the ball-on-disk tests, the most accurate distributions are the Gaussian, Ex-Gaussian, and Skew-normal.



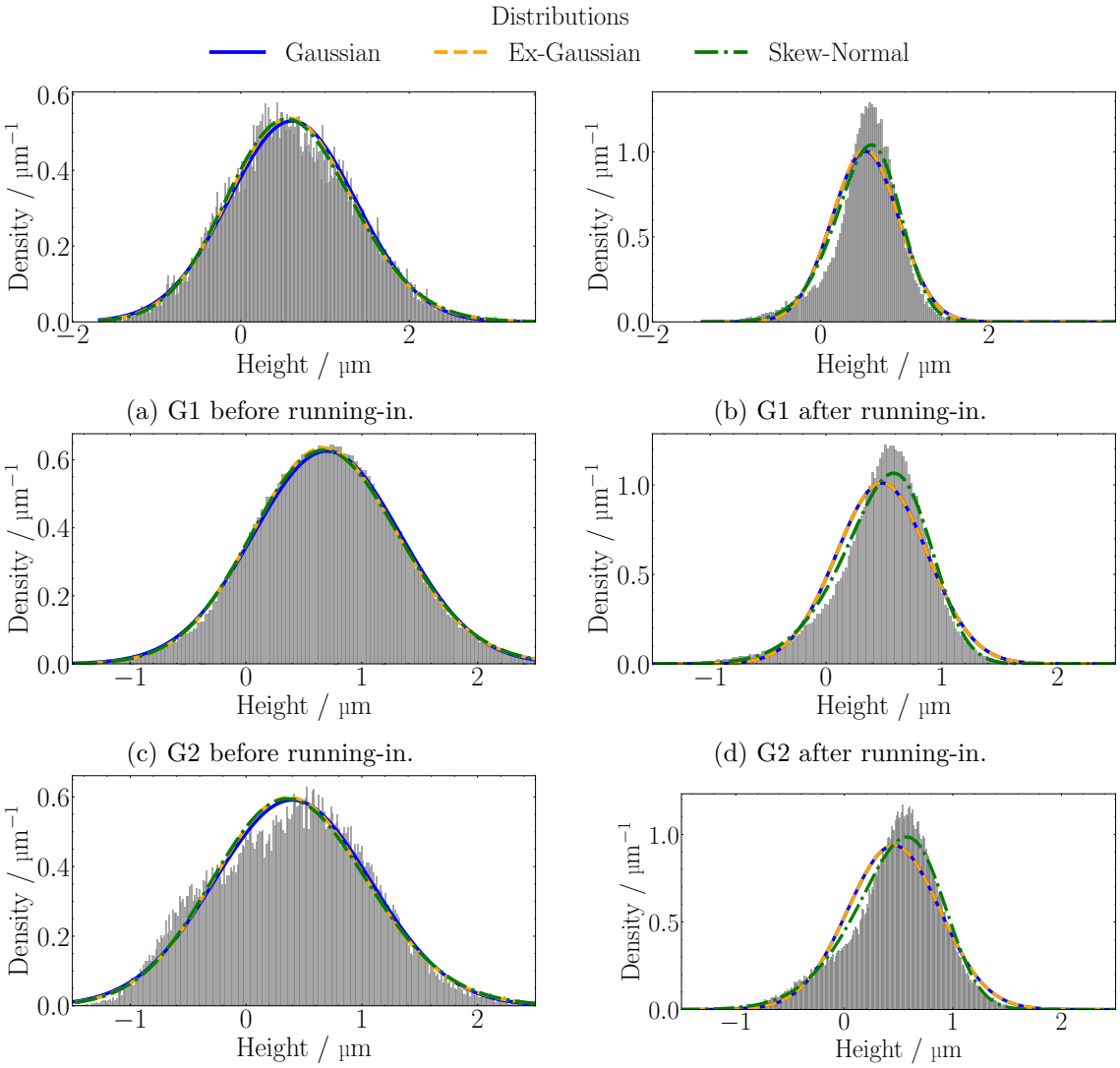
(a) Before running-in.

(b) After running-in.

Figure 5.30: Summit heights of the G3's pinion before and after running-in

In Figure 5.31 their fit are compared with all the considered pinion surfaces. As previously explained, both the Skew-Normal and Ex-Gaussian distributions are extensions of the Gaussian distribution, and under certain conditions, they become Gaussian distributions. If summit heights are symmetrical, the Skew-Normal becomes a Gaussian distribution, and, in the Ex-Gaussian distribution, if there is no exponential component, it also becomes a Gaussian distribution. This is what happens in the samples before running-in, where the distributions are almost equal, still, after the running-in process, the height becomes asymmetrical, which increases the importance of the Skew-Normal distribution. Even though the Ex-Gaussian distribution is not different from the Gaussian one after running-in, it is important to also use it because the surface could present an exponential behavior that is not present in the studied surfaces and it slightly increased the accuracy in the samples before running-in. To obtain the distribution parameter for those two distributions, the procedure in Section 5.2 was used, obtaining the Table 5.22 and 5.23.

It is important to note that the wheel parameters are estimated from the difference between the ratio of the profiles of the respective pinions and wheels, and that could result in some strange results like the ones of the α parameter, but this is the best approach available.



(a) G1 before running-in.

(b) G1 after running-in.

(c) G2 before running-in.

(d) G2 after running-in.

(e) G3 before running-in.

(f) G3 after running-in.

Figure 5.31: Summit heights of the pinions before and after running-in.

Table 5.22: Distribution parameters of the pinion surface in the gear sets.

Distribution	**Parameter**	**G1**		**G2**		**G3**	
		Before	**After**	**Before**	**After**	**Before**	**After**
Ex-Gaussian	μ_E / 10^6	0.304	0.449	0.452	0.439	0.141	0.456
	σ_E / 10^6	0.688	0.386	0.586	0.392	0.622	0.426
	τ_E / 10^6	0.306	0.081	0.247	0.044	0.260	0.0003
	α	1.080	-1.621	0.826	-2.039	0.947	-2.117
Skew-Normal	λ_{SN} / 10^6	0.066	0.890	0.323	0.880	-0.042	0.895
	δ_{SN} / 10^6	0.929	0.537	0.740	0.560	0.807	0.612

Table 5.23: Distribution parameters of the wheel surface in the gear sets.

Distribution	Parameter	G1		G2		G3	
		Before	**After**	**Before**	**After**	**Before**	**After**
Ex-Gaussian	μ_E / 10^6	0.2240	0.356	0.2492	0.3615	0.0513	0.2990
	σ_E / 10^6	0.3717	0.271	0.4462	0.2719	0.4424	0.2788
	τ_E / 10^6	0.3888	0.092	0.5327	0.0255	0.4677	0.0002
Skew-Normal	α	41.54	-0.532	-1.6942	-6.235	227.74	31.40
	λ_{SN} / 10^6	0.0393	0.503	0.0437	0.7500	0.0004	0.8602
	δ_{SN} / 10^6	0.6021	0.366	0.6022	0.3692	0.6766	0.4152

Figures 5.32 to 5.34 show the friction along the path of contact of each gear set for the 3 relevant distributions before and after running-in, and no relevant differences were encountered.

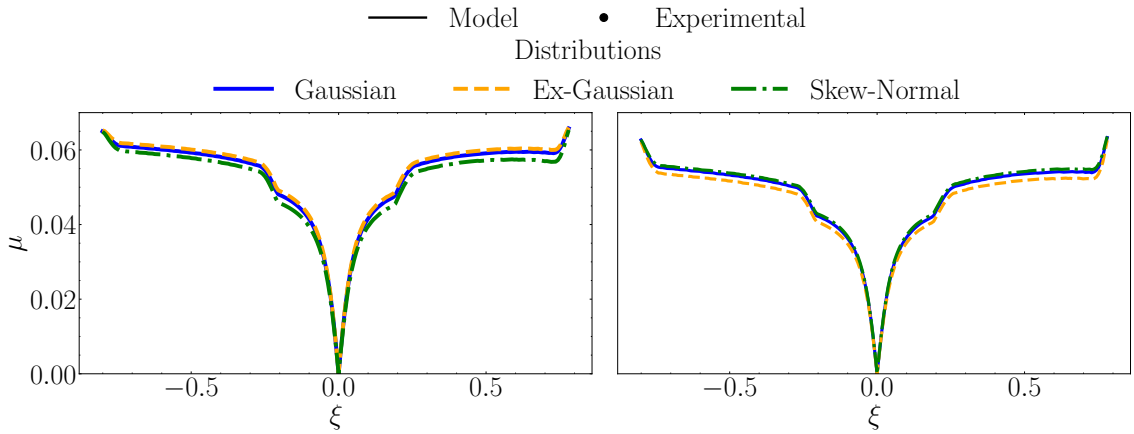


Figure 5.32: Gear set G1's coefficient of friction before and after running-in.

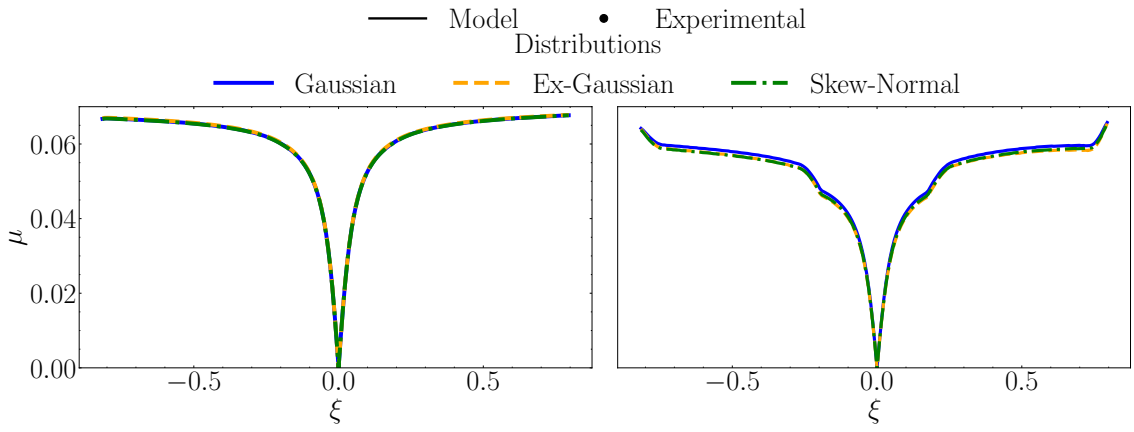


Figure 5.33: Gear set G2's coefficient of friction before and after running-in.

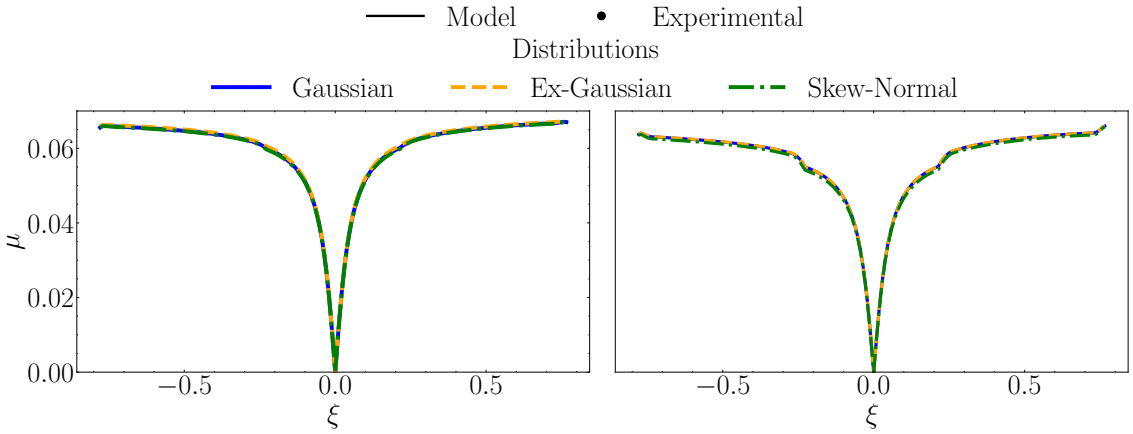


Figure 5.34: Gear set G3's coefficient of friction before and after running-in.

Chapter 6

Conclusions and Future works

6.1 Conclusions

This dissertation focused on describing a contact model to predict the coefficient of friction in different types of contacts using a numerical implementation of the load sharing concept and Greenwood and Williamson's asperity contact model, which was expanded to consider the thermal effects in the contact. The procedure to obtain the roughness parameters and to statistically model the surface was discussed, including a newly proposed method for select the summits. Finally, the model is compared with experimental data from ball-on-disk tests and FZG tests.

The model's results presented in Chapter 5 shown good performance in the ball-on-disk tests and in the torque loss FZG tests under higher loads when the proposed method of selecting the summits based in a matrix window, that is slightly bigger than twice the asperity radius in each direction, is used. Besides that, it is also shown that the roughness parameters highly influenced the results from the model, which indicates that a more in-depth study must be done and a better understanding of the procedure to obtain the summits roughness parameters.

Yet, even though a better study of the roughness is necessary, the model clearly represented the expected tendencies in the running-in process, that is, the friction coefficient is reduced after the running-in process. The same can be said of the results obtained in the torque loss test, where the experimental tendencies are visible in the model.

An important point of this dissertation was the use of non-Gaussian distributions to model the summit heights, mainly in surfaces after running-in, and no relevant differences were encountered for the analyzed surface. Still, great potential is shown in the Ex-Gaussian and Skew-Normal distributions that are extensions of the Gaussian distribution. The relevance of those distributions lies in the fact that if a surface shows a Gaussian behavior, it becomes a Gaussian distribution.

While good results were obtained, the model presented limitations that in the future

should be solved, besides the obvious problem associated with the calculation of the roughness parameters, the statistical approach used could lead to a bad representation of the summit heights if the selected distribution does not model the summit heights accurately. Besides that, the model considered the asperities to have a spherical tip while, due to the manufacturing process associated with gears, the surface of gears are not isotropic, so in reality the asperities should be model as ellipsoids or cylinders. To overcome that limitation, the equations of the asperity contact used should be adapted to new form the tip of the summit.

Another limitation is the method to estimate the limit shear stress, for which insufficient data were available to obtain a relation between the limit shear stress, temperature, and mean contact pressure.

6.2 Future works

In the future, several new features must be implemented in the model and certain concepts must be better understood. Regarding model improvements, a better method to calculate the roughness parameters must be developed, the Greenwood and Williamson's asperity contact model should be adapt to non-spherical asperities by changing the initial assumption of a spherical tip, and improved to consider the plastic deformation of the asperities. It should be developed a deterministic model not only to increase the accuracy, but also to serve as another proof to validate the statistical one.

Furthermore, while the process to consider the local roughness of tooth is described, the extraction of the involute profile is still manual, and estimation of the roughness parameters and its implementation in to the friction model is not developed, so, in the future it is important to implement that.

More in-deep studies are need to better understand of the rheological behavior of the lubricant, to understand the influence of parameters like contact force and speed in the roughness after the running-in, and to understand the wear during the running-in phase.

Regarding the wear, a preliminary study of a wear model using the roughness parameters provided by the work of Fernandes et al. [1] was done, assuming an exponential decay of the roughness parameters following the equation (6.1) [71], where R_{ai} is the initial average roughness, t_r is the running-in time of the surface, and A_r and k_r are fitting parameters.

$$R_a = R_{ai} - A_r \left(1 - e^{-k_r t_r}\right) \tag{6.1}$$

Bibliography

[1] C. M. C. G. Fernandes, J. C. Pais, R. C. Martins, and J. H. O. Seabra, "Influence of running-in operating conditions on the steady-state torque loss of ground spur gears," *Forschung im Ingenieurwesen*, vol. 85, pp. 567–582, 6 2021. doi:10.1007/s10010-021-00447-0.

[2] C. M. C. G. Fernandes, R. C. Martins, and J. H. O. Seabra, "Coefficient of friction equation for gears based on a modified hersey parameter," *Tribology International*, vol. 101, pp. 204–217, 9 2016. doi:10.1016/J.TRIBOINT.2016.03.028.

[3] K. L. Johnson, J. A. Greenwood, and S. Y. Poon, "A simple theory of asperity contact in elastohydro-dynamic lubrication," *Wear*, vol. 19, pp. 91–108, 1 1972. doi:10.1016/0043-1648(72)90445-0.

[4] J. A. Greenwood and J. B. P. Williamson, "Contact of nominally flat surfaces," *Proceedings of the Royal Society of London. Series A. Mathematical and Physical Sciences*, vol. 295, pp. 300–319, 12 1966. doi:10.1098/rspa.1966.0242.

[5] "The 17 goals | sustainable development." https://sdgs.un.org/goals. Accessed: 27-June-2025.

[6] L. Mummery, *Surface Texture Analysis: The Handbook*. Hommelwerke GmbH, 1992.

[7] H. K. Tönshoff and B. Denkena, *Surface and Subsurface Properties*, pp. 349–370. Berlin, Heidelberg: Springer Berlin Heidelberg, 2013. doi:10.1007/978-3-642-33257-9_16.

[8] J. C. Poletto, *Identification of wear failure modes of metal contacts by surface topography*. PhD thesis, Ghent University, 2024.

[9] D.-H. Lee and N.-G. Cho, "Assessment of surface profile data acquired by a stylus profilometer," *Measurement Science and Technology*, vol. 23, p. 105601, 10 2012. doi:10.1088/0957-0233/23/10/105601.

[10] R. Posusta, "Correlating advanced 3d optical profiling surface measurements to traceable standards | bruker." https://www.bruker.com/en/products-and-solutions/test-and-measurement/3d-optical-profilers/resource-library/an-558-

correlating-advanced-3d-optical-profiling-surface-measurements-to-traceable-standards.html, 2016.

[11] D. Lange, H. Jennings, and S. P. Shah, "Analysis of surface roughness using confocal microscopy," *Journal of Materials Science*, vol. 28, pp. 3879–3884, 09 1993. doi:10.1007/BF00353195.

[12] H. Liu, D. Li, M. Xi, T. Li, K. Liu, X. Liu, and Y. Wang, "Chromatic confocal precision measurement accuracy analysis with surface roughness based on a scalar diffraction and raytracing hybrid model," *Optics and Lasers in Engineering*, vol. 178, p. 108256, 7 2024. doi:10.1016/j.optlaseng.2024.108256.

[13] S. Fu, W. S. Kor, F. Cheng, and L. K. Seah, "In-situ measurement of surface roughness using chromatic confocal sensor," *Procedia CIRP*, vol. 94, pp. 780–784, 1 2020. 11th CIRP Conference on Photonic Technologies [LANE 2020] doi:10.1016/J.PROCIR.2020.09.133.

[14] Y. Li, J. Lin, H. Song, Y. Xiang, Z. Shi, and U. Olofsson, "Local surface roughness of cylindrical gears: Concept, method, and application," *Tribology International*, vol. 207, p. 110637, 7 2025. doi:10.1016/j.triboint.2025.110637.

[15] J. A. Brandão, J. H. Seabra, and M. J. Castro, "Surface fitting of an involute spur gear tooth flank roughness measurement to its nominal shape," *Measurement*, vol. 91, pp. 479–487, 2016. doi:10.1016/j.measurement.2016.05.076.

[16] T. L. Krantz, "On the correlation of specific film thickness and gear pitting life," Conference Paper GRC–E–DAA–TN16935, NASA Glenn Research Center, Cleveland, OH, United States, Oct. 2014. NASA NTRS Document ID 20150000701; U.S. government work, public domain.

[17] "Gears — cylindrical involute gears and gear pairs — concepts and geometry," ISO 21771:2007, International Organization for Standardization, Geneva, Switzerland, 2007.

[18] C. Fernandes, "Engrenagens — Órgãos de máquinas — licenciatura em engenharia mecânica," tech. rep., University of Porto, Porto, Portugal, 2022. [Online; accessed 15-Jun-2025].

[19] I. C. Faraon, *Mixed Lubricated Line Contacts*. Phd thesis - research ut, graduation ut, University of Twente, Netherlands, 11 2005.

[20] "Peak density along x,y - michigan metrology." https://michmet.com/glossary-term/peak-density-along-xy/. Accessed: 19-May-2025.

[21] E. Tomanik, H. Chacon, and G. Teixeira, "A simple numerical procedure to calculate the input data of greenwood-williamson model of asperity contact for actual engineering surfaces," in *Tribological Research and Design for Engineering Systems* (D. Dowson, M. Priest, G. Dalmaz, and A. A. Lubrecht, eds.), vol. 41 of *Tribology Series*, pp. 205–215, Elsevier, 2003. doi:10.1016/S0167-8922(03)80133-5.

[22] N. Yu and A. Polycarpou, "Extracting summit roughness parameters from random gaussian surfaces accounting for asymmetry of the summit heights," *Journal of Tribology-transactions of The Asme - J TRIBOL-TRANS ASME*, vol. 126, 10 2004. doi:10.1115/1.1792698.

[23] S. Akbarzadeh and M. M. Khonsari, "On the prediction of running-in behavior in mixed-lubrication line contact," *Journal of Tribology*, vol. 132, pp. 1–11, 7 2010. doi:10.1115/1.4001622.

[24] J. Brooks-Barlett, "Probability concepts explained: Maximum likelihood estimation | by jonny brooks-bartlett | tds archive | medium." https://medium.com/data-science/probability-concepts-explained-maximum-likelihood-estimation-c7b4342fdbb1, 1 2018. Accessed: 20-May-2025.

[25] H. Abubakar, M. Misiran, and A. I. A. Sayed, "Estimation of shifted weibull distribution parameters using optimization algorithms for optimal investment decisions making," *Franklin Open*, vol. 8, p. 100152, 9 2024. doi:10.1016/j.fraope.2024.100152.

[26] S. Kotz, T. Kozubowski, and K. Podgorski, *The Laplace Distribution and Generalizations*. 01 2001. doi:10.1007/978-1-4612-0173-1_5.

[27] Y. Dodonova and Y. Dodonov, "On choosing a model for estimating individual differences in latent growth trajectories," *Psikhologicheskie Issledovaniya*, vol. 6, 02 2013.

[28] F. Figueiredo and M. I. Gomes, "The skew-normal distribution in spc," *Revstat - Statistical Journal*, vol. 11, pp. 83–104, 03 2013. doi:10.57805/revstat.v11i1.128.

[29] M. Sosa, *Running-in of Gears – Surface and Efficiency Transformation*. Ph.d. dissertation, KTH Royal Institute of Technology, Stockholm, Sweden, 2017.

[30] A. Clarke, I. J. J. Weeks, R. W. Snidle, and H. P. Evans, "Running-in and micropitting behaviour of steel surfaces under mixed lubrication conditions," *Tribology International*, vol. 101, pp. 59–68, 9 2016. doi:10.1016/j.triboint.2016.03.007.

[31] M. J. Neale, "C26 - running-in procedures," in *Tribology Handbook (Second Edition)* (M. NEALE, ed.), pp. C26.1–C26.5, Oxford: Butterworth-Heinemann, second edition ed., 1995. doi:978-0-7506-1198-5.

[32] M. Khonsari, S. Ghatrehsamani, and S. Akbarzadeh, "On the running-in nature of metallic tribo-components: A review," *Wear*, vol. 474-475, p. 203871, 2021. doi:10.1016/j.wear.2021.203871.

[33] S. Akbarzadeh and M. M. Khonsari, "Experimental and theoretical investigation of running-in," *Tribology International*, vol. 44, pp. 92–100, 2 2011. doi:10.1016/j.triboint.2010.09.006.

[34] P. J. Blau, "Running-in: Art or engineering?," *Journal of Materials Engineering*, vol. 13, pp. 47–53, 3 1991. doi:10.1007/BF02834123.

[35] M. Varenberg, "Towards a unified classification of wear," *Friction*, vol. 1, pp. 333–340, 12 2013. doi:10.1007/s40544-013-0027-x.

[36] A. Beheshti and M. M. Khonsari, "An engineering approach for the prediction of wear in mixed lubricated contacts," *Wear*, vol. 308, pp. 121–131, 11 2013. doi:10.1016/j.wear.2013.10.004.

[37] A. Beheshti and M. M. Khonsari, "A thermodynamic approach for prediction of wear coefficient under unlubricated sliding condition," *Tribology Letters*, vol. 38, pp. 347–354, 6 2010. doi:10.1007/s11249-010-9614-4.

[38] B. Podgornik, "Adhesive wear failures," *Journal of Failure Analysis and Prevention*, vol. 22, pp. 113–138, 2 2022. doi:10.1007/s11668-021-01322-4.

[39] J. Seabra, A. Campos, and A. Sottomayor, *Lubrificação Elastohidrodinâmica*. SMAP; DEMEGI; FEUP, 9 2002.

[40] C. Fernandes, "Tribologia — Órgãos de máquinas — licenciatura em engenharia mecânica," tech. rep., University of Porto, Porto, Portugal, 2024. [Online; accessed 15-Jun-2025].

[41] E. R. M. Gelinck and D. J. Schipper, "Calculation of stribeck curves for line contacts," *Tribology International*, vol. 33, no. 3, pp. 175–181, 2000. doi:10.1016/S0301-679X(00)00024-4.

[42] C. M. C. G. Fernandes, "Experimental procedure to determine the load sharing under ehl conditions," 7 2024.

[43] A. Arana, J. Larrañaga, and I. Ulacia, "Partial ehl friction coefficient model to predict power losses in cylindrical gears," *Proceedings of the Institution of Mechanical Engineers, Part J: Journal of Engineering Tribology*, vol. 233, no. 2, pp. 303–316, 2019. doi:10.1177/1350650118778655.

[44] R. I. Taylor and I. Sherrington, "A simplified approach to the prediction of mixed and boundary friction," *Tribology International*, vol. 175, p. 107836, 2022. doi:10.1016/j.triboint.2022.107836.

[45] J. A. Greenwood and J. H. Tripp, "The contact of two nominally flat rough surfaces," *Proceedings of the Institution of Mechanical Engineers*, vol. 185, pp. 625–633, 6 1970. doi:10.1243/PIME_PROC_1970_185_069_02.

[46] A. W. Bush, R. D. Gibson, and T. R. Thomas, "The elastic contact of a rough surface," *Wear*, vol. 35, no. 1, pp. 87–111, 1975. doi:10.1016/0043-1648(75)90145-3.

[47] R. Coy, "Practical applications of lubrication models in engines1paper presented at the world tribology congress, london, september 1997.1," *Tribology International*, vol. 31, no. 10, pp. 563–571, 1998. doi:10.1016/S0301-679X(98)00077-2.

[48] A. Doleschel, *Wirkungsgradberechnung von Zahnradgetrieben in Abhängigkeit vom Schmierstoff*. Dissertation, Technical University of Munich, 2003. [Efficiency calculation of gear drives depending on the lubricant].

[49] S. Matsumoto and K. Morikawa, "The new estimation formula of coefficient of friction in rolling-sliding contact surface under mixed lubrication condition for the power loss reduction of power transmission gears," in *International Gear Conference 2014: 26th–28th August 2014, Lyon* (P. Velex, ed.), pp. 1078–1088, Oxford: Chandos Publishing, 2014. doi:10.1533/9781782421955.1078.

[50] Y. Diab, F. Ville, and P. Velex, "Prediction of power losses due to tooth friction in gears," *Tribology Transactions*, vol. 49, no. 2, pp. 260–270, 2006. doi:10.1080/05698190600614874.

[51] A. V. Olver and H. A. Spikes, "Prediction of traction in elastohydrodynamic lubrication," *Proceedings of the Institution of Mechanical Engineers, Part J: Journal of Engineering Tribology*, vol. 212, no. 5, pp. 321–332, 1998. doi:10.1243/1350650981542137.

[52] "EHD - PCS instruments." https://pcs-instruments.com/product/ehd/. Accessed: 12-fev-2025.

[53] J. Moder, F. Grün, M. Stoschka, and I. Gódor, "A novel two-disc machine for high precision friction assessment," *Advances in Tribology*, vol. 2017, pp. 1–16, 06 2017. doi:10.1155/2017/8901907.

[54] Y. Diab, F. Ville, and P. Velex, "Prediction of power losses due to tooth friction in gears," *Tribology Transactions*, vol. 49, pp. 260–270, 2006. doi:10.1080/05698190600614874.

[55] M. Sosa, S. Björklund, U. Sellgren, and U. Olofsson, "In situ surface characterization of running-in of involute gears," *Wear*, vol. 340-341, pp. 41–46, 2015. Papers from the NORDTRIB 2014 conference co-edited by Prof. Ion Marius Sivebæk and Lars Pleth Nielsen doi:10.1016/j.wear.2015.03.008.

[56] J. A. Brandão, M. Meheux, F. Ville, J. H. Seabra, and J. Castro, "Comparative overview of five gear oils in mixed and boundary film lubrication," *Tribology International*, vol. 47, pp. 50–61, 2012. doi:10.1016/j.triboint.2011.10.007.

[57] I. Hutchings and P. Shipway, "2 - surface topography and surfaces in contact," in *Tribology (Second Edition)* (I. Hutchings and P. Shipway, eds.), pp. 7–35, Butterworth-Heinemann, second edition ed., 2017. doi:10.1016/B978-0-08-100910-9.00002-7.

[58] L. Paouris, R. Rahmani, S. Theodossiades, H. Rahnejat, G. Hunt, and W. Barton, "An analytical approach for prediction of elastohydrodynamic friction with inlet shear heating and starvation," *Tribology Letters*, vol. 64, p. 10, 10 2016. doi:10.1007/s11249-016-0740-5.

[59] S. Bair and W. Habchi, "Quantitative ehl - seventeen years in," *Journal of Tribology*, vol. 146, pp. 1–32, 04 2024. doi:10.1115/1.4065299.

[60] H. Moes, *Lubrication and Beyond*. Netherlands: University of Twente, 2000.

[61] D. J. Schipper, *Transitions in lubrication of concentrated contacts*. Ph.d. dissertation, University of Twente, 1955.

[62] K. L. Johnson and J. L. Tevaarwerk, "Shear behaviour of elastohydrodynamic oil films," *Proceedings of the Royal Society of London. A. Mathematical and Physical Sciences*, vol. 356, pp. 215–236, 1977. doi:10.1098/rspa.1977.0129.

[63] R. I. Popovici and D. J. Schipper, "Stribeck and traction curves for elliptical contacts: Isothermal friction model," *International Journal of Sustainable Construction & Design*, vol. 4, Feb. 2014. doi:10.21825/scad.v4i2.1042.

[64] D. J. Whitehouse and J. F. Archard, "The properties of random surfaces of significance in their contact," *Proceedings of the Royal Society of London. A. Mathematical and Physical Sciences*, vol. 316, pp. 97–121, 3 1970. doi:10.1098/rspa.1970.0068.

[65] A. V. Olver, "Testing transmission lubricants: The importance of thermal response," *Proceedings of the Institution of Mechanical Engineers, Part G: Journal of Aerospace Engineering*, vol. 205, pp. 35–44, 1991. .

[66] J. Brandão, M. Meheux, J. Seabra, F. Ville, and J. Castro, "Traction curves and rheological parameters of fully formulated gear oils," *Proceedings of the Institution of Mechanical Engineers, Part J: Journal of Engineering Tribology*, vol. 225, pp. 577–593, 07 2011. doi:10.1177/1350650111405111.

[67] C. M. Fernandes, "10 - temperature prediction in polymer gears: semianalytical modeling," in *Polymer Gears* (S. Thomas, M. Huskić, H. J. Maria, and J. Tavćar, eds.), pp. 219–247, Elsevier, 2025. doi:10.1016/B978-0-443-21457-8.00012-1.

[68] C. M. Fernandes, P. M. Marques, R. C. Martins, and J. H. O. Seabra, "Film thickness and traction curves of wind turbine gear oils," *Tribology International*, vol. 86, pp. 1–9, 6 2015. doi:10.1016/j.triboint.2015.01.014.

[69] Z. Ma, Y. Zhao, Y. Han, W. Lou, S. Li, X. Wang, F. Guo, and H. Liu, "Approach to determine the limiting shear stress of lubricants at high pressures based on traction mapping," *Lubricants*, vol. 12, no. 4, 2024. doi:10.3390/lubricants12040128.

[70] J. C. Pais, "Influência do processo de rodagem na eficiência de engrenagens," master's thesis, Instituto Superior de Engenharia do Porto, Porto, Portugal, 2019.

[71] M. Hanief and M. Wani, "Modeling and prediction of surface roughness for running-in wear using gauss-newton algorithm and ann," *Applied Surface Science*, vol. 357, pp. 1573–1577, 2015. doi:10.1016/j.apsusc.2015.10.052.

Appendix A

Elliptical Contact

Along this appendix it will be exposed the equation for the implementation of the elliptical contact in the model. Firstly the Hertzian properties are discussed, then how the film thickness is calculated. Lastly the thermal model is explained.

A.1 Hertzian Contact

Within a contact problem, it is essential do define the Hertzian contact properties, namely the reduced radius (R), reduced elasticity modulus (E'), Hertzian pressure (p_h), the minor and major semi-axis of the contact elliptical area (a and b), and the nominal contact area (A_c), being calculated with the next equations [19]:

$$R_x = \left(\frac{1}{R_{x1}} + \frac{1}{R_{x2}}\right)^{-1} \tag{A.1}$$

$$R_y = \left(\frac{1}{R_{y1}} + \frac{1}{R_{y2}}\right)^{-1} \tag{A.2}$$

$$R = \left(\frac{1}{R_x} + \frac{1}{R_y}\right)^{-1} \tag{A.3}$$

$$E' = \left[\frac{1}{2}\left(\frac{1-\nu_1^2}{E_1} + \frac{1-\nu_2^2}{E_2}\right)\right]^{-1} \tag{A.4}$$

$$a = C_\alpha \left(\frac{2F_n R}{E'}\right)^{\frac{1}{3}} \tag{A.5}$$

$$b = C_\beta \left(\frac{2F_n R}{E'}\right)^{\frac{1}{3}} \tag{A.6}$$

$$A_c = \pi ab \tag{A.7}$$

$$p_h = \frac{3}{2}\frac{F_n}{\pi ab} \tag{A.8}$$

Where:

$$C_\alpha = \kappa^{\frac{1}{3}} \left[\frac{2}{\pi} E(m)\right]^{\frac{1}{3}} \tag{A.9}$$

$$C_\alpha = \kappa^{\frac{-2}{3}} \left[\frac{2}{\pi} E(m)\right]^{\frac{1}{3}} \tag{A.10}$$

$$E(m) = \frac{\pi}{2}(1-m)\left[1 + \frac{2m}{\pi(1-m)} - \frac{1}{8}\ln(1-m)\right] \tag{A.11}$$

$$\kappa = \left[1 + \sqrt{\frac{\ln(16/\lambda)}{2\lambda}} - \sqrt{\ln(4)} + 0.16\ln(\lambda)\right]^{-1} \tag{A.12}$$

$$m = 1 - \kappa^2 \tag{A.13}$$

$$\lambda = \frac{R_x}{R_y} \tag{A.14}$$

Where R_{xi} is the contact radius in the direction x,R_{yi} is the contact radius in the direction y , ν_i is the Poisson ratio, E_i is the Young's modulus, all referent to the body i and b is the gear width.

A.2 Elastohydrodynamic lubrication

Utilizing the same approach than the linear contact, the film thickness are calculated using dimensionless numbers proposed by Downson and Higginson (equations (A.15) to (A.18)) and Moes (equations (A.19) to (A.21)) [63].

$$G = \alpha E' \tag{A.15}$$

$$\overline{h} = h_c / R_x \tag{A.16}$$

$$U_\Sigma = \frac{\eta_0 (U_1 + U_2)}{E' R_x} \tag{A.17}$$

$$W = \frac{F_n}{E' R_x^2} \tag{A.18}$$

$$H = \overline{h} U_\Sigma^{-\frac{1}{2}} \tag{A.19}$$

$$M = W U_\Sigma^{-\frac{3}{4}} \tag{A.20}$$

$$L = G U_\Sigma^{-\frac{1}{4}} \tag{A.21}$$

The Moes' dimensionless central film thickness is defined by:

$$H_c = \left\{ \left[H_{RI}^{\frac{2}{3}} + \left(H_{EI}^{-4} + H_{00}^{-4} \right)^{-\frac{3}{8}} \right]^{\frac{2s}{3}} + \left(H_{RP}^{-8} + H_{EP}^{-8} \right)^{-\frac{s}{8}} \right\}^{1/s} \tag{A.22}$$

Where H_{00} is a constant that is dependent in the ellipticity of a contact (equation (A.23)) and the remaining are given by equations (A.24) to (A.28).

$$H_{00} = 1.8\vartheta^{-1} \tag{A.23}$$

$$s = 1.5\left[1+\exp\left(-1.2\frac{H_{EI}}{H_{RI}}\right)\right] \tag{A.24}$$

$$H_{RI} = 145\left(1+0.796\vartheta^{\frac{14}{15}}\right)^{-\frac{15}{7}}\vartheta^{-1}M^{-2} \tag{A.25}$$

$$H_{EI} = 3.18\left(1+0.006\ln\vartheta+0.63\vartheta^{\frac{4}{7}}\right)^{-\frac{14}{25}}\vartheta^{-\frac{1}{15}}M^{-\frac{2}{15}} \tag{A.26}$$

$$H_{RP} = 1.29\left(1+0.691\vartheta\right)^{-\frac{2}{3}}L^{\frac{2}{3}} \tag{A.27}$$

$$H_{EP} = 1.48\left(1+0.006\ln\vartheta+0.63\vartheta^{\frac{4}{7}}\right)^{-\frac{7}{20}}\vartheta^{-\frac{1}{24}}M^{-\frac{1}{12}}L^{\frac{3}{4}} \tag{A.28}$$

$$\vartheta = R_x/R_y \tag{A.29}$$

Where ϑ is the ratio of the reduced radius of curvature in the direction and in perpendicular direction of the rolling/sliding direction.

A.3 Mixed lubrication model

Using the Load sharing concept already described in Chapter 3, H_c is adapted to the equation (A.30) [63].

$$H_c = \gamma_1^{\frac{1}{2}}\left\{\left[\gamma_1^{\frac{9}{4}}H_{RI}^{\frac{2}{3}}+\left(\gamma_1^{-\frac{2}{5}}H_{EI}^{-4}+H_{00}^{-4}\right)^{-\frac{3}{8}}\right]^{\frac{2s}{3}}+\left[\gamma_1^{4}\left(H_{RP}^{-8}+H_{EP}^{-8}\right)\right]^{-\frac{s}{8}}\right\}^{1/s} \tag{A.30}$$

Since the same equations from the Greenwood and Williamson's asperities contact model and properties of the oil can be used they will not be discussed in this appendix.

A.4 Thermal model

With the film thickness defined, it numerical process is similar to the linear contact, except the thermal. While the influence of the heat is accounted with ϕ_T, the equations for the temperature are slightly changed (equations (A.31) to (A.37)), but the numerical cycle is the same [58].

$$\dot{Q} = \mu F_n v_g \tag{A.31}$$

$$R_{cf} = \frac{h_c}{2kA_H} \tag{A.32}$$

$$R_{fi} = \frac{1.06}{A_H k_s}\sqrt{\frac{\chi_i a}{U_i}} \tag{A.33}$$

$$\epsilon = \frac{R_{f2} + R_{cf}}{R_{f1} + R_{f2} + 2R_{cf}} \tag{A.34}$$

$$\Delta\overline{T}_{Fl} = R_{f1}\epsilon\dot{q} \tag{A.35}$$

$$\Delta\overline{T}_{oil} = \frac{v_g\overline{\tau}h_c}{8k} \tag{A.36}$$

$$\Delta\overline{T}_f = T_0 + \Delta\overline{T}_{Fl} + \Delta\overline{T}_{oil} \tag{A.37}$$